

# First-order quantum phase transitions: test ground for emergent chaoticity, regularity and persisting symmetries

M. Macek<sup>a,\*</sup>, A. Leviatan<sup>a,\*\*</sup>

<sup>a</sup>*Racah Institute of Physics, The Hebrew University, Jerusalem 91904, Israel*

---

## Abstract

We present a comprehensive analysis of the emerging order and chaos and enduring symmetries, accompanying a generic (high-barrier) first-order quantum phase transition (QPT). The interacting boson model Hamiltonian employed, describes a QPT between spherical and deformed shapes, associated with its  $U(5)$  and  $SU(3)$  dynamical symmetry limits. A classical analysis of the intrinsic dynamics reveals a rich but simply-divided phase space structure with a Hénon-Heiles type of chaotic dynamics ascribed to the spherical minimum and a robustly regular dynamics ascribed to the deformed minimum. The simple pattern of mixed but well-separated dynamics persists in the coexistence region and traces the crossing of the two minima in the Landau potential. A quantum analysis discloses a number of regular low-energy  $U(5)$ -like multiplets in the spherical region, and regular  $SU(3)$ -like rotational bands extending to high energies and angular momenta, in the deformed region. These two kinds of regular subsets of states retain their identity amidst a complicated environment of other states and both occur in the coexistence region. A symmetry analysis of their wave functions shows that they are associated with partial  $U(5)$  dynamical symmetry (PDS) and  $SU(3)$  quasi-dynamical symmetry (QDS), respectively. The pattern of mixed but well-separated dynamics and the PDS or QDS characterization of the remaining regularity, appear to be robust throughout the QPT. Effects of kinetic collective rotational terms, which may disrupt this simple pattern, are considered.

### *Keywords:*

Quantum shape-phase transitions; Regularity and chaos; Partial and quasi-dynamical symmetries; Interacting boson model (IBM).

*PACS:* 21.60.Fw; 05.45.Mt; 05.30.Rt; 21.10.Re

---

---

\*Current address: Center for Theoretical Physics, Sloane Physics Laboratory, Yale University, New Haven, CT 06520-8120, USA

\*\*Corresponding author.

*Email addresses:* mmacek@Racah.phys.huji.ac.il (M. Macek), ami@phys.huji.ac.il (A. Leviatan)

## 1. Introduction

Quantum phase transitions (QPTs) are qualitative changes in the properties of a physical system induced by a variation of parameters  $\lambda$  in the quantum Hamiltonian  $\hat{H}(\lambda)$  [1, 2, 3]. Such ground-state transformations have received considerable attention in recent years and have found a variety of applications in many areas of physics and chemistry [4]. These structural modifications occur at zero-temperature in diverse dynamical systems including spin lattices [5], ensembles of ultracold atoms [6, 7] and atomic nuclei [8].

The particular type of QPT is reflected in the topology of the underlying mean-field (Landau) potential  $V(\lambda)$ . Most studies have focused on second-order (continuous) QPTs, where  $V(\lambda)$  has a single minimum which evolves continuously into another minimum. The situation is more complex for discontinuous (first-order) QPTs, where  $V(\lambda)$  develops multiple minima that coexist in a range of  $\lambda$  values and cross at the critical point,  $\lambda = \lambda_c$ . The competing interactions in the Hamiltonian that drive these ground-state phase transitions can affect dramatically the nature of the dynamics and, in some cases, lead to the emergence of quantum chaos [9, 10, 11]. This effect has been observed in quantum optics models of  $N$  two-level atoms interacting with a single-mode radiation field [12, 13], where the onset of chaos is triggered by continuous QPTs. In the present article, we examine similar effects for the less-studied discontinuous QPTs, and explore the nature of the underlying classical and quantum dynamics in such circumstances.

The interest in first-order quantum phase transitions stems from their key role in phase-coexistence phenomena at zero temperature. In condensed matter physics, it has been recently recognized that, for clean samples, the nature of the QPT becomes discontinuous as the critical-point is approached. Examples are offered by the metal-insulator Mott transition [14], itinerant magnets [15], heavy-fermion superconductors [16], quantum Hall bilayers [17], Bose-Einstein condensates [18] and Bose-Fermi mixture [19]. First-order QPTs are relevant to shape-coexistence in mesoscopic systems, such as atomic nuclei [8], and to optimization problems in quantum computing [20].

Hamiltonians describing first-order QPTs are often non-integrable, hence their dynamics is mixed. They form a subclass among the family of generic Hamiltonians with a mixed phase space, in which regular and chaotic motion coexist. Mixed phase spaces are often encountered in billiard systems [9, 10, 11], which are generated by the free motion of a point particle inside a closed domain whose geometry governs the amount of chaoticity. Here, in contrast, we consider many-body interacting systems undergoing a first-order QPT, where the onset of chaos is governed by a change of coupling constants in the Hamiltonian. The amount of order and disorder in the system is affected by the relative strengths of different terms in the Hamiltonian which have incompatible symmetries. Order, chaos and symmetries are thus intertwined, and their study can shed light on the structure evolution. In conjunction with first-order QPTs, this raises a number of key questions. (i) How does the interplay of order and chaos reflect the first-order QPT, in particular, the changing topology of the Landau potential in the coexistence region. (ii) What is the symmetry character (if any) of the remaining regularity in the system, amidst a complicated environment. (iii) What is the effect of kinetic terms, which do not affect the potential, on the onset of chaos across

the QPT.

To address these questions in a transparent manner, we employ an interacting boson model (IBM) [21], which describes quantum phase transitions between spherical and deformed nuclei. The model is amenable to both classical and quantum treatments, has a rich algebraic structure and inherent geometry. The phases are associated with different nuclear shapes and correspond to solvable dynamical symmetry limits of the model. The Hamiltonian accommodates QPTs of first- and second order between these shapes, by breaking and mixing the relevant limiting symmetries. These attributes make the IBM an ideal framework for studying the intricate interplay of order and chaos and the role of symmetries in such quantum shape-phase transitions. It is a representative of a wide class of algebraic models used for describing many-body systems, *e.g.*, nuclei [21], molecules [22] and hadrons [23].

QPTs have been studied extensively in the IBM framework [8, 24, 25] and are manifested empirically in nuclei [26, 27]. The situation is summarized in the indicated review papers where a complete list of references is given. Particular attention has been paid to symmetry aspects (critical point symmetries [28, 29], quasi-dynamical [30, 31, 32] and partial dynamical symmetries [33]), finite-size effects [34, 35, 36, 37, 38] and scaling behavior [39, 40, 41]. Further extensions of the QPT concept to excited states [42] and to Bose-Fermi systems [43], have also been considered.

Chaotic properties of the IBM have been thoroughly investigated both classically and quantum mechanically [44, 45, 46, 47, 48, 49, 50, 51]. All such treatments involved a simplified Hamiltonian giving rise to integrable second order QPTs and to non-integrable first order QPTs with an extremely low barrier and narrow coexistence region. A new element in the present treatment, compared to previous works, is the employment of IBM Hamiltonians without such restrictions [37] and their resolution into intrinsic and collective parts [52, 53]. This enables a comprehensive analysis of the vibrational and rotational dynamics across a generic (high-barrier) first-order QPT, both inside and outside the coexistence region. Brief accounts of some aspects of this analysis were reported in [54, 55].

Section 2 reviews the algebraic, geometric and symmetry content of the IBM. An intrinsic Hamiltonian for a first-order QPT between spherical and deformed shapes, with an adjustable barrier height, is introduced in Section 3, and its symmetry properties are discussed. The classical limit of the QPT Hamiltonian is derived in Section 4. The topology of the classical potential is studied in great detail, identifying the control and order parameters in various structural regions of the QPT. A comprehensive classical analysis is performed in Section 5, focusing on regular and chaotic features of the intrinsic vibrational dynamics across the QPT. Special attention is paid to the dynamics in the vicinity of minima in the Landau potential and to resonance effects. An elaborate quantum analysis is conducted in Section 6 with emphasis on quantum manifestations of classical chaos and remaining regular features in the spectrum. A symmetry analysis is performed in Section 7, examining the symmetry content of eigenstates and the evolution of purity and coherence throughout the QPT. The impact of different collective rotational terms on the classical and quantum dynamics is considered in Section 8. The implications of modifying the barrier height, are examined in Section 9. The final Section is devoted to a summary and conclusions. Specific details on the IBM potential surface and on linear correlation coefficients are collected in

Appendix A and B, respectively.

## 2. The interacting boson model: algebras, geometry, and symmetries

The interacting boson model (IBM) [21] describes low-lying quadrupole collective states in nuclei in terms of  $N$  interacting monopole ( $s$ ) and quadrupole ( $d$ ) bosons representing valence nucleon pairs. The bilinear combinations  $\mathcal{G}_{ij} \equiv b_i^\dagger b_j = \{s^\dagger s, s^\dagger d_m, d_m^\dagger s, d_m^\dagger d_{m'}\}$  span a  $U(6)$  algebra, which serves as the spectrum generating algebra. The IBM Hamiltonian is expanded in terms of these generators,  $\hat{H} = \sum_{ij} \epsilon_{ij} \mathcal{G}_{ij} + \sum_{ijkl} u_{ijkl} \mathcal{G}_{ij} \mathcal{G}_{kl} + \dots$ , and consists of Hermitian, rotational-invariant interactions which conserve the total number of  $s$ - and  $d$ - bosons,  $\hat{N} = \hat{n}_s + \hat{n}_d = s^\dagger s + \sum_m d_m^\dagger d_m$ . A dynamical symmetry (DS) occurs if the Hamiltonian can be written in terms of the Casimir operators of a chain of nested sub-algebras of  $U(6)$ . The Hamiltonian is then completely solvable in the basis associated with each chain. The three dynamical symmetries of the IBM [56, 57, 58] and corresponding bases are

$$U(6) \supset U(5) \supset O(5) \supset O(3) \quad |N, n_d, \tau, n_\Delta, L\rangle \quad \text{spherical vibrator} \quad (1a)$$

$$U(6) \supset SU(3) \supset O(3) \quad |N, (\lambda, \mu), K, L\rangle \quad \text{axially-deformed rotor} \quad (1b)$$

$$U(6) \supset O(6) \supset O(5) \supset O(3) \quad |N, \sigma, \tau, n_\Delta, L\rangle \quad \gamma\text{-unstable deformed rotor} \quad (1c)$$

The associated analytic solutions resemble known limits of the geometric model of nuclei [59], as indicated above. The basis members are classified by the irreducible representations (irreps) of the corresponding algebras. Specifically, the quantum numbers  $N, n_d, (\lambda, \mu), \sigma, \tau$  and  $L$  label the relevant irreps of  $U(6), U(5), SU(3), O(6), O(5)$  and  $O(3)$ , respectively.  $n_\Delta$  and  $K$  are multiplicity labels needed for complete classification of selected states in the reductions  $O(5) \supset O(3)$  and  $SU(3) \supset O(3)$ , respectively. Each basis is complete and can be used for a numerical diagonalization of the Hamiltonian in the general case. Relevant information on the generators, Casimir operators and eigenvalues for the above algebras is collected in Table 1. Also listed are additional algebras,  $\overline{O(6)}$  and  $\overline{SU(3)}$ , obtained by a phase-change of the  $s$ -boson.

A geometric visualization of the model is obtained by a potential surface

$$V(\beta, \gamma) = \langle \beta, \gamma; N | \hat{H} | \beta, \gamma; N \rangle, \quad (2)$$

defined by the expectation value of the Hamiltonian in the following intrinsic condensate state [60, 61]

$$|\beta, \gamma; N\rangle = (N!)^{-1/2} [\Gamma_c^\dagger(\beta, \gamma)]^N |0\rangle, \quad (3a)$$

$$\Gamma_c^\dagger(\beta, \gamma) = \left[ \beta \cos \gamma d_0^\dagger + \beta \sin \gamma (d_2^\dagger + d_{-2}^\dagger) / \sqrt{2} + \sqrt{2 - \beta^2} s^\dagger \right] / \sqrt{2}. \quad (3b)$$

Here  $(\beta, \gamma)$  are quadrupole shape parameters analogous to the variables of the collective model of nuclei [59]. Their values  $(\beta_{\text{eq}}, \gamma_{\text{eq}})$  at the global minimum of  $V(\beta, \gamma)$  define the equilibrium shape for a given Hamiltonian. For one- and two-body interactions, the shape



Table 1: Generators, linear and quadratic Casimir operators  $\hat{C}_G$  and their eigenvalues  $\langle \hat{C}_G \rangle$ , for algebras  $G$  in the IBM. Here  $\hat{n}_s = s^\dagger s$ ,  $\hat{n}_d = \sqrt{5} U^{(0)}$ ,  $\hat{N} = \hat{n}_s + \hat{n}_d$ ,  $L_m^{(1)} = \sqrt{10} U_m^{(1)}$ ,  $Q_m^{(2)} = \Pi_m^{(2)} - \frac{\sqrt{7}}{2} U_m^{(2)}$ ,  $\bar{Q}_m^{(2)} = \bar{\Pi}_m^{(2)} + \frac{\sqrt{7}}{2} U_m^{(2)}$ ,  $\Pi_m^{(2)} = d_m^\dagger s + s^\dagger \tilde{d}_m$ ,  $\bar{\Pi}_m^{(2)} = i(d_m^\dagger s - s^\dagger \tilde{d}_m)$ ,  $U_m^{(\ell)} = (d^\dagger \tilde{d})_m^{(\ell)}$ , where  $U_m^{(\ell)}$  stands for a spherical tensor operator of rank  $\ell$  projection  $m$ , and  $\tilde{d}_m = (-1)^m d_{-m}$ .

Algebra	Generators	Casimir operator $\hat{C}_G$	Eigenvalues $\langle \hat{C}_G \rangle$
O(3)	$U^{(1)}$	$L^{(1)} \cdot L^{(1)}$	$L(L+1)$
O(5)	$U^{(1)}, U^{(3)}$	$2 \sum_{L=1,3} U^{(L)} \cdot U^{(L)}$	$\tau(\tau + 3)$
O(6)	$U^{(1)}, U^{(3)}, \Pi^{(2)}$	$\hat{C}_{O(5)} + \Pi^{(2)} \cdot \Pi^{(2)}$	$\sigma(\sigma + 4)$
SU(3)	$U^{(1)}, Q^{(2)}$	$2Q^{(2)} \cdot Q^{(2)} + \frac{3}{4} \hat{C}_{O(3)}$	$\lambda^2 + (\lambda + \mu)(\mu + 3)$
U(5)	$U^{(\ell)} \ell = 0, \dots, 4$	$\hat{n}_d, \hat{n}_d(\hat{n}_d + 4)$	$n_d, n_d(n_d + 4)$
U(6)	$\hat{n}_s, \Pi^{(2)}, \bar{\Pi}^{(2)}, U^{(\ell)} \ell = 0, \dots, 4$	$\hat{N}, \hat{N}(\hat{N} + 5)$	$N, N(N + 5)$
$\overline{O(6)}$	$U^{(1)}, U^{(3)}, \bar{\Pi}^{(2)}$	$\hat{C}_{O(5)} + \bar{\Pi}^{(2)} \cdot \bar{\Pi}^{(2)}$	$\bar{\sigma}(\bar{\sigma} + 4)$
$\overline{SU(3)}$	$U^{(1)}, \bar{Q}^{(2)}$	$2\bar{Q}^{(2)} \cdot \bar{Q}^{(2)} + \frac{3}{4} \hat{C}_{O(3)}$	$\bar{\lambda}^2 + (\bar{\lambda} + \bar{\mu})(\bar{\mu} + 3)$

can be spherical ( $\beta_{\text{eq}} = 0$ ) or deformed ( $\beta_{\text{eq}} > 0$ ) with  $\gamma_{\text{eq}} = 0$  (prolate),  $\gamma_{\text{eq}} = \pi/3$  (oblate) or  $\gamma$ -independent. The parameterization adapted in Eq. (3) is particularly suitable for a classical analysis of the model. An alternative parameterization for the shape parameters and further properties of the potential surface are discussed in Appendix A.

The dynamical symmetries of Eq. (1) correspond to solvable limits of the model. The often required symmetry breaking is achieved by including in the Hamiltonian terms associated with different sub-algebra chains of U(6). In general, under such circumstances, solvability is lost, there are no remaining non-trivial conserved quantum numbers and all eigenstates are expected to be mixed. However, for particular symmetry breaking, some intermediate symmetry structure can survive. The latter include partial dynamical symmetry (PDS) [62] and quasi-dynamical symmetry (QDS) [30]. In a PDS, the conditions of an exact dynamical symmetry (solvability of the complete spectrum and existence of exact quantum numbers for all eigenstates) are relaxed and apply to only part of the eigenstates and/or of the quantum numbers. In a QDS, particular states continue to exhibit selected characteristic properties (*e.g.*, energy and B(E2) ratios) of the closest dynamical symmetry, in the face of strong-symmetry breaking interactions. This ‘‘apparent’’ symmetry is due to the coherent nature of the mixing. Interestingly, both PDS [33] and QDS [30, 31, 32] have been shown to occur in quantum phase transitions.

In discussing the dynamics of the IBM Hamiltonian, it is convenient to resolve it into intrinsic and collective parts [52, 53],

$$\hat{H} = \hat{H}_{\text{int}} + \hat{H}_{\text{col}}. \quad (4)$$

The intrinsic part ( $\hat{H}_{\text{int}}$ ) determines the potential surface  $V(\beta, \gamma)$ , Eq. (2), and is defined to

yield zero when acting on the equilibrium condensate

$$\hat{H}_{\text{int}}|\beta = \beta_{\text{eq}}, \gamma = \gamma_{\text{eq}}; N\rangle = 0. \quad (5)$$

For  $\beta_{\text{eq}} = 0$ , the condensate is spherical, and consists of a single state with angular momentum  $L = 0$  built from  $N$  s-bosons. For  $(\beta_{\text{eq}} > 0, \gamma_{\text{eq}} = 0)$  the condensate is deformed, and has angular projection  $K = 0$  along the symmetry  $z$ -axis. States of good  $L$  projected from it span the  $K = 0$  ground band, and other eigenstates of  $\hat{H}_{\text{int}}$  are arranged in excited  $K$ -bands. The collective part ( $\hat{H}_{\text{col}}$ ) has a flat potential surface and involves collective rotations linked with the groups in the chain  $O(6) \supset O(5) \supset O(3)$ . These orthogonal groups correspond to “generalized” rotations associated with the  $\beta$ -,  $\gamma$ - and Euler angles degrees of freedom, respectively. Apart from constant terms of no significance to the excitation spectrum, the collective Hamiltonian is composed of the two-body parts of the respective Casimir operators

$$\hat{H}_{\text{col}} = \bar{c}_3 \left[ \hat{C}_{O(3)} - 6\hat{n}_d \right] + \bar{c}_5 \left[ \hat{C}_{O(5)} - 4\hat{n}_d \right] + \bar{c}_6 \left[ \hat{C}_{O(6)} - 5\hat{N} \right]. \quad (6)$$

Here  $\hat{C}_G$  are defined in Table 1 and a per-boson scaling is invoked  $\bar{c}_i = c_i/N(N-1)$  to ensure that the bounds of the energy spectrum do not change for large  $N$ . In general, the intrinsic and collective Hamiltonians do not commute and  $\hat{H}_{\text{col}}$  splits and mixes the bands generated by  $\hat{H}_{\text{int}}$ .

### 3. First order quantum phase transitions in the IBM

The dynamical symmetries of the IBM, Eq. (1), correspond to phases of the system, and provide analytic benchmarks for the dynamics of stable nuclear shapes. Quantum phase transitions (QPTs) between different shapes are studied [61] by considering Hamiltonians  $\hat{H}(\lambda)$  that mix interaction terms from different DS chains, *e.g.*,  $\hat{H}(\lambda) = \lambda\hat{H}_1 + (1-\lambda)\hat{H}_2$ . The coupling coefficient ( $\lambda$ ) responsible for the mixing, serves as the control parameter which upon variation induces qualitative changes in the properties of the system. The kind of QPT is dictated by the potential surface  $V(\lambda) \equiv V(\lambda; \beta, \gamma)$ , Eq. (2), which serves as a mean-field Landau potential with the equilibrium deformations  $(\beta_{\text{eq}}, \gamma_{\text{eq}})$  as order parameters. The order of the phase transition and the critical point,  $\lambda = \lambda_c$ , are determined by the order of the derivative with respect to  $\lambda$  of  $V(\lambda; \beta_{\text{eq}}, \gamma_{\text{eq}})$ , where discontinuities first occur.

The IBM phase diagram [63] consists of spherical and deformed phases separated by a line of first-order transition ending in a point of second-order transitions in-between the spherical [U(5)] and deformed  $\gamma$ -unstable [O(6)] phases. The spherical [U(5)] to axially-deformed [SU(3)] transition is of first order and the O(6)-SU(3) transition exhibits a cross-over. In what follows, we examine the nature of the classical and quantum dynamics across a generic first-order QPT, with a high-barrier separating the two phases.

#### 3.1. Intrinsic Hamiltonian in a first order QPT

Focusing on first-order QPTs between stable spherical ( $\beta_{\text{eq}} = 0$ ) and prolate-deformed ( $\beta_{\text{eq}} > 0, \gamma_{\text{eq}} = 0$ ) shapes, the intrinsic Hamiltonian reads

$$\hat{H}_1(\rho)/\hbar_2 = 2(1-\rho^2\beta_0^2)\hat{n}_d(\hat{n}_d-1) + \beta_0^2 R_2^\dagger(\rho) \cdot \tilde{R}_2(\rho), \quad (7a)$$

$$\hat{H}_2(\xi)/\hbar_2 = \xi P_0^\dagger(\beta_0)P_0(\beta_0) + P_2^\dagger(\beta_0) \cdot \tilde{P}_2(\beta_0), \quad (7b)$$

where  $\hat{n}_d$  is the  $d$ -boson number operator and the boson pair operators are defined as

$$R_{2\mu}^\dagger(\rho) = \sqrt{2}s^\dagger d_\mu^\dagger + \rho\sqrt{7}(d^\dagger d^\dagger)_\mu^{(2)} , \quad (8a)$$

$$P_0^\dagger(\beta_0) = d^\dagger \cdot d^\dagger - \beta_0^2 (s^\dagger)^2 , \quad (8b)$$

$$P_{2\mu}^\dagger(\beta_0) = \sqrt{2}\beta_0 s^\dagger d_\mu^\dagger + \sqrt{7}(d^\dagger d^\dagger)_\mu^{(2)} . \quad (8c)$$

In Eq. (7),  $\tilde{R}_{2\mu} = (-1)^\mu R_{2,-\mu}$ ,  $\tilde{P}_{2\mu} = (-1)^\mu P_{2,-\mu}$ , standard notation of angular momentum coupling is used and the dot implies a scalar product. As in Eq. (6), scaling by  $\bar{h}_2 \equiv h_2/N(N-1)$  is used throughout ( $h_2 > 0$ ), to facilitate the comparison with the classical limit. The control parameters that drive the QPT are  $\rho$  and  $\xi$ , with  $0 \leq \rho \leq \beta_0^{-1}$  and  $\xi \geq 0$ , while  $\beta_0$  is a constant.

The intrinsic Hamiltonian in the spherical phase,  $\hat{H}_1(\rho)$ , describes the dynamics of a spherical shape and satisfies Eq. (5), with  $\beta_{\text{eq}} = 0$ . For large  $N$ , its normal modes involve five-dimensional quadrupole vibrations about the spherical global minimum of its potential surface, with frequency

$$\epsilon = 2\bar{h}_2 N \beta_0^2 . \quad (9)$$

The intrinsic Hamiltonian in the deformed phase,  $\hat{H}_2(\xi)$ , describes the dynamics of an axially-deformed shape and satisfies Eq. (5), with ( $\beta_{\text{eq}} = \sqrt{2}\beta_0(1 + \beta_0^2)^{-1/2}$ ,  $\gamma_{\text{eq}} = 0$ ). For large  $N$ , its normal modes involve one-dimensional  $\beta$  vibration and two-dimensional  $\gamma$  vibrations about the prolate-deformed global minimum of its potential surface, with frequencies

$$\epsilon_\beta = 2\bar{h}_2 N \beta_0^2 (2\xi + 1) , \quad (10a)$$

$$\epsilon_\gamma = 18\bar{h}_2 N \beta_0^2 (1 + \beta_0^2)^{-1} . \quad (10b)$$

The two intrinsic Hamiltonians coincide at the critical point,  $\rho_c = \beta_0^{-1}$  and  $\xi_c = 0$ ,

$$\hat{H}_{\text{cri}}^{\text{int}} \equiv \hat{H}_1(\rho_c) = \hat{H}_2(\xi_c) , \quad (11)$$

where  $\hat{H}_{\text{cri}}^{\text{int}}$  is the critical-point intrinsic Hamiltonian considered in [37].

The collective Hamiltonian, Eq. (6), does not affect the shape of the potential surface but can contribute a shift to the normal-mode frequencies, Eqs. (9)-(10), by the amount

$$\epsilon^c = 2N\bar{c}_6 , \quad (12a)$$

$$\epsilon_\beta^c = 2N\bar{c}_6 , \quad (12b)$$

$$\epsilon_\gamma^c = 2N [\bar{c}_6 + \bar{c}_5 \beta_0^2 (1 + \beta_0^2)^{-1}] . \quad (12c)$$

In general, given an Hamiltonian  $\hat{H}$ , the intrinsic and collective parts, Eq. (4), are fixed by the condition of Eq. (5) and by requiring  $\hat{H}_{\text{int}}$  and  $\hat{H}$  to have the same shape for the potential surface. For example, an Hamiltonian [64] frequently used in the study of QPTs is

$$\hat{H} = \epsilon \hat{n}_d - \kappa Q(\chi) \cdot Q(\chi) , \quad (13)$$

where  $Q(\chi) = d^\dagger s + s^\dagger \tilde{d} + \chi (d^\dagger \tilde{d})^{(2)}$  is the quadrupole operator and  $\epsilon \geq 0$ ,  $\kappa \geq 0$ ,  $-\frac{\sqrt{7}}{2} \leq \chi < 0$ . The critical-point Hamiltonian is obtained for a specific relation among  $\epsilon$ ,  $\kappa$  and  $\chi$ ,

$$\hat{H}_{\text{cri}} : \quad \epsilon = \kappa \left[ \left( \frac{2}{7} \chi^2 + 4 \right) N + \frac{5}{7} \chi^2 - 8 \right] . \quad (14)$$

The parameters of the intrinsic and collective Hamiltonians are then found to be

$$\hat{H}_{\text{cri}}^{\text{int}} : \quad \bar{h}_2 = 2\kappa \quad , \quad \rho_c = \beta_0^{-1} \quad , \quad \xi_c = 0 \quad , \quad \beta_0 = -\frac{1}{\sqrt{14}} \chi . \quad (15a)$$

$$\hat{H}_{\text{cri}}^{\text{col}} : \quad \bar{c}_3 = \kappa(2 - \beta_0^2) \quad , \quad \bar{c}_5 = \kappa(4\beta_0^2 - 5) \quad , \quad \bar{c}_6 = \kappa . \quad (15b)$$

In the present study, we adapt a different strategy. We fix the value of the parameter  $\beta_0$  in the intrinsic Hamiltonian, Eq. (7), so as to ensure a high barrier at the critical point. We then vary, *independently*, the control parameters  $(\rho, \xi)$  in the intrinsic Hamiltonian and the parameters  $\bar{c}_3, \bar{c}_5, \bar{c}_6$ , of the collective Hamiltonian, Eq. (6). This will allow us to examine, separately, the influence on the dynamics of those terms affecting the Landau potential and of individual rotational kinetic terms, in a generic (high-barrier) first order QPT.

### 3.2. Symmetry properties and integrability

The symmetry properties of the intrinsic Hamiltonian (7) depend on the choice of control parameters  $(\rho, \xi)$  and of  $\beta_0$ . In general, the dynamical symmetries are completely broken in the Hamiltonian and hence the underlying dynamics is non-integrable. However, for particular values of these parameters, exact dynamical symmetries (DS) or partial dynamical symmetries (PDS) can occur and their presence affects the integrability of the system.

The appropriate intrinsic Hamiltonian in the spherical phase is  $\hat{H}_1(\rho)$ , Eq. (7a), with  $0 \leq \rho \leq \beta_0^{-1}$ . For  $\rho = 0$ ,  $\hat{H}_1(\rho = 0)$  reduces to

$$\hat{H}_1(\rho = 0)/\bar{h}_2 = 2\hat{n}_d(\hat{n}_d - 1) + 2\beta_0^2(\hat{N} - \hat{n}_d)\hat{n}_d , \quad (16)$$

and hence has U(5) DS. The spectrum is completely solvable

$$|N, n_d, \tau, n_\Delta, L\rangle \quad E_{\text{DS}} = [2n_d(n_d - 1) + 2\beta_0^2(N - n_d)n_d] \bar{h}_2 . \quad (17)$$

The eigenstates are those of the U(5) chain, Eq. (1a), with  $n_d = 0, 1, 2, \dots, N$  and  $\tau = n_d, n_d - 2, \dots, 1$  or 0. The values of  $L$  are obtained by partitioning  $\tau = 3n_\Delta + p$ , with  $n_\Delta, p \geq 0$  integers, and  $L = 2p, 2p - 2, 2p - 3, \dots, p$ . The spectrum resembles that of an anharmonic spherical vibrator, describing quadrupole excitations of a spherical shape. The lowest U(5) multiplets involve states with quantum numbers [56]

$$\begin{aligned} n_d = 3 : & \quad L = 6, 4, 3, 0 \quad (\tau = 3) \quad L = 2 \quad (\tau = 1) \\ n_d = 2 : & \quad L = 4, 2 \quad (\tau = 2) \quad L = 0 \quad (\tau = 0) \\ n_d = 1 : & \quad L = 2 \quad (\tau = 1) \\ n_d = 0 : & \quad L = 0 \quad (\tau = 0) \end{aligned} \quad (18)$$

The situation changes drastically when  $\rho > 0$ , for which the Hamiltonian becomes

$$\begin{aligned} \hat{H}_1(\rho)/\bar{h}_2 = & \quad 2\hat{n}_d(\hat{n}_d - 1) + 2\beta_0^2(\hat{N} - \hat{n}_d)\hat{n}_d + \rho^2\beta_0^2(2\hat{C}_{O(5)} - \hat{C}_{O(3)} - 2\hat{n}_d) \\ & + \rho\beta_0^2\sqrt{14}[(d^\dagger d^\dagger)^{(2)} \cdot \tilde{d}s + H.c.] , \end{aligned} \quad (19)$$

where *H.c.* means Hermitian conjugate. In this case, the last term in Eq. (19) breaks the U(5) DS, and induces U(5) and O(5) mixing subject to  $\Delta n_d = \pm 1$  and  $\Delta \tau = \pm 1, \pm 3$ . The explicit breaking of O(5) symmetry leads to non-integrability and, as will be shown in subsequent discussions, is the main cause for the onset of chaos in the spherical region. Although  $\hat{H}_1(\rho)$ , Eq. (19), is not diagonal in the U(5) chain, it retains the following selected solvable U(5) basis states [62]

$$|[N], n_d = \tau = L = 0\rangle \quad E_{\text{PDS}} = 0, \quad (20a)$$

$$|[N], n_d = \tau = L = 3\rangle \quad E_{\text{PDS}} = 6 [2 + \beta_0^2(N - 3) + 3\rho^2\beta_0^2] \bar{h}_2, \quad (20b)$$

while other eigenstates are mixed. As such, it exhibits U(5) partial dynamical symmetry [U(5)-PDS].

In the deformed phase, the appropriate intrinsic Hamiltonian is  $\hat{H}_2(\xi)$ , Eq. (7b), with  $\xi \geq 0$ . The latter has a zero-energy ground band composed of states with  $L = 0, 2, 4, \dots, 2N$ , projected from the intrinsic state, Eq. (3), with  $(\beta_{\text{eq}} = \sqrt{2}\beta_0(1 + \beta_0^2)^{-1/2}, \gamma_{\text{eq}} = 0)$ . For  $\beta_0 = \sqrt{2}$  and  $\xi = 1$ , the Hamiltonian reduces to

$$\hat{H}_2(\xi = 1; \beta_0 = \sqrt{2})/\bar{h}_2 = -\hat{C}_{SU(3)} + 2\hat{N}(2\hat{N} + 3), \quad (21)$$

and hence has SU(3) DS. The spectrum is completely solvable

$$|N, (\lambda, \mu), K, L\rangle \quad E_{\text{DS}}/\bar{h}_2 = [-c(\lambda, \mu) + 2N(2N + 3)] \bar{h}_2, \quad (22)$$

where  $c(\lambda, \mu)$  are the eigenvalues of the SU(3) Casimir operator listed in Table 1. The eigenstates are those of the SU(3) chain, Eq. (1b), with  $(\lambda, \mu) = (2N - 4k - 6m, 2k)$ , with  $k, m$  non-negative integers, such that,  $\lambda, \mu \geq 0$ . The values of  $L$  contained in these SU(3) irreps are  $L = K, K + 1, K + 2, \dots, K + \max\{\lambda, \mu\}$ , where  $K = 0, 2, \dots, \min\{\lambda, \mu\}$ ; with the exception of  $K = 0$  for which  $L = 0, 2, \dots, \max\{\lambda, \mu\}$ . The spectrum resembles that of an axially-deformed rotor with degenerate K-bands arranged in SU(3) multiplets,  $K$  being the angular momentum projection on the symmetry axis. The lowest SU(3) irreps are  $(2N, 0)$  which describes the ground band  $g(K = 0)$ ,  $(2N - 4, 2)$  which contains the  $\beta(K = 0)$  and  $\gamma(K = 2)$  bands, and  $(2N - 8, 4)$ ,  $(2N - 6, 0)$ , which contain the  $\beta^2(K = 0)$ ,  $\beta\gamma(K = 2)$ ,  $\gamma^2(K = 0, 4)$  bands. The corresponding band-members are [57]

$$\begin{aligned} (\lambda, \mu) = (2N - 6, 0) : & \quad L = 0, 2, 4, \dots \quad (K = 0) & \quad \gamma^2, \beta^2 \\ (\lambda, \mu) = (2N - 8, 4) : & \quad L = 4, 5, 6, \dots \quad (K = 4) & \quad \gamma^2 \\ & \quad L = 2, 3, 4, \dots \quad (K = 2) & \quad \beta\gamma \\ & \quad L = 0, 2, 4, \dots \quad (K = 0) & \quad \beta^2, \gamma^2 \\ (\lambda, \mu) = (2N - 4, 2) : & \quad L = 2, 3, 4, \dots \quad (K = 2) & \quad \gamma \\ & \quad L = 0, 2, 4, \dots \quad (K = 0) & \quad \beta \\ (\lambda, \mu) = (2N, 0) : & \quad L = 0, 2, 4, \dots \quad (K = 0) & \quad g \end{aligned} \quad (23)$$

For  $\beta_0 = \sqrt{2}$  and  $\xi \neq 1$ , the Hamiltonian becomes

$$\hat{H}_2(\xi; \beta_0 = \sqrt{2})/\bar{h}_2 = -\hat{C}_{SU(3)} + 2\hat{N}(2\hat{N} + 3) + (\xi - 1)P_0^\dagger P_0, \quad (24)$$

where  $P_0^\dagger \equiv P_0^\dagger(\beta_0 = \sqrt{2})$  of Eq. (8b). The added term breaks the SU(3) DS of the Hamiltonian and most eigenstates are mixed with respect to SU(3). However, the following states [62]

$$|N, (2N, 0)K = 0, L\rangle \quad L = 0, 2, 4, \dots, 2N$$

$$E_{\text{PDS}} = 0 \tag{25a}$$

$$|N, (2N - 4k, 2k)K = 2k, L\rangle \quad L = K, K + 1, \dots, (2N - 2k) \quad k > 0 ,$$

$$E_{\text{PDS}} = 6k(2N - 2k + 1)\bar{\hbar}_2 \tag{25b}$$

remain solvable with good SU(3) symmetry. As such,  $\hat{H}_2(\xi; \beta_0 = \sqrt{2})$  exhibits SU(3) partial dynamical symmetry [SU(3)-PDS]. The selected states of Eq. (25) span the ground band  $g(K = 0)$  and  $\gamma^k(K = 2k)$  bands. Such Hamiltonians with SU(3)-PDS have been used for the spectroscopy of deformed rotational nuclei [65, 66]. In general, the analytic properties of the solvable states in a PDS, provide unique signatures for their identification in the quantum spectrum.

The collective Hamiltonian of Eq. (6) preserves the O(5) symmetry for any choice of couplings  $\bar{c}_i$ , hence its dynamics is integrable with  $\tau$  and  $L$  as good quantum numbers. The  $\hat{C}_{\text{O}(3)}$  and  $\hat{C}_{\text{O}(5)}$  terms lead to an  $L(L + 1)$  and  $\tau(\tau + 3)$  type of splitting. In general, integrability is lost when the collective Hamiltonian is added to the intrinsic Hamiltonian (7), since the latter breaks the O(5) symmetry, and only  $L$  remains a good quantum number for the full Hamiltonian. A notable exception is when  $\rho = 0$ , since now all terms in  $\hat{H}_1(\rho = 0) + \hat{H}_{\text{col}}$ , respect the O(5) symmetry.

#### 4. Classical limit

The classical limit of the IBM is obtained through the use of Glauber coherent states [67]. This amounts to replacing  $(s^\dagger, d_\mu^\dagger)$  by six c-numbers  $(\alpha_s^*, \alpha_\mu^*)$  rescaled by  $\sqrt{N}$  and taking  $N \rightarrow \infty$ , with  $1/N$  playing the role of  $\hbar$ . Number conservation ensures that phase space is 10-dimensional and can be phrased in terms of two shape (deformation) variables, three orientation (Euler) angles and their conjugate momenta. The shape variables can be identified with the  $\beta, \gamma$  variables introduced through Eq. (3). Setting all momenta to zero, yields the classical potential which is identical to  $V(\beta, \gamma)$  of Eq. (2). In the classical analysis presented below we consider, for simplicity, the dynamics of  $L = 0$  vibrations, for which only two degrees of freedom are active. The rotational dynamics with  $L > 0$  is examined in the subsequent quantum analysis.

#### 4.1. Classical limit of the QPT Hamiltonian

For the intrinsic Hamiltonian of Eq. (7), constrained to  $L = 0$ , the above procedure yields the following classical Hamiltonian

$$\begin{aligned} \mathcal{H}_1(\rho)/h_2 &= \mathcal{H}_{d,0}^2 + \beta_0^2(1 - \mathcal{H}_{d,0})\mathcal{H}_{d,0} + \rho^2\beta_0^2p_\gamma^2 \\ &\quad + \rho\beta_0^2\sqrt{\frac{1-\mathcal{H}_{d,0}}{2}} \left[ (p_\gamma^2/\beta - \beta p_\beta^2 - \beta^3) \cos 3\gamma + 2p_\beta p_\gamma \sin 3\gamma \right] , \end{aligned} \quad (26a)$$

$$\begin{aligned} \mathcal{H}_2(\xi)/h_2 &= \mathcal{H}_{d,0}^2 + \beta_0^2(1-\mathcal{H}_{d,0})\mathcal{H}_{d,0} + p_\gamma^2 \\ &\quad + \beta_0\sqrt{\frac{1-\mathcal{H}_{d,0}}{2}} \left[ (p_\gamma^2/\beta - \beta p_\beta^2 - \beta^3) \cos 3\gamma + 2p_\beta p_\gamma \sin 3\gamma \right] \\ &\quad + \xi \left[ \beta^2 p_\beta^2 + \frac{1}{4}(\beta^2 - T)^2 - \beta_0^2(1 - \mathcal{H}_{d,0})(\beta^2 - T) + \beta_0^4(1-\mathcal{H}_{d,0})^2 \right] . \end{aligned} \quad (26b)$$

Here the coordinates  $\beta \in [0, \sqrt{2}]$ ,  $\gamma \in [0, 2\pi)$  and their canonically conjugate momenta  $p_\beta \in [0, \sqrt{2}]$  and  $p_\gamma \in [0, 1]$  span a compact classical phase space. The term

$$\mathcal{H}_{d,0} \equiv (T + \beta^2)/2 \quad , \quad T = p_\beta^2 + p_\gamma^2/\beta^2 \quad , \quad (27)$$

denotes the classical limit of  $\hat{n}_d$  (restricted to  $L = 0$ ) and forms an isotropic harmonic oscillator Hamiltonian in the  $\beta$  and  $\gamma$  variables. Notice that the classical Hamiltonian of Eq. (26) contains complicated momentum-dependent terms originating from the two-body interactions in the Hamiltonian (7), not just the usual quadratic kinetic energy  $T$ . Setting  $p_\beta = p_\gamma = 0$  in Eq. (26) leads to the following classical potential

$$V_1(\rho)/h_2 = \beta_0^2\beta^2 - \rho\beta_0^2\sqrt{2-\beta^2}\beta^3 \cos 3\gamma + \frac{1}{2}(1-\beta_0^2)\beta^4 \quad , \quad (28a)$$

$$\begin{aligned} V_2(\xi)/h_2 &= \beta_0^2[1 - \xi(1+\beta_0^2)]\beta^2 - \beta_0\sqrt{2-\beta^2}\beta^3 \cos 3\gamma \\ &\quad + \frac{1}{4} [2(1-\beta_0^2) + \xi(1+\beta_0^2)^2] \beta^4 + \xi\beta_0^4 . \end{aligned} \quad (28b)$$

The same expressions can be obtained from Eq. (2) using the static intrinsic coherent state (3). Notice that the potential of Eq. (28) is independent of  $N$  due to the per-boson scaling used in Eq. (7).

The variables  $\beta$  and  $\gamma$  can be interpreted as polar coordinates in an abstract plane parameterized by Cartesian coordinates  $(x, y)$ . The transformation between these two sets of coordinates and conjugate momenta is

$$x = \beta \cos \gamma \quad , \quad y = \beta \sin \gamma \quad , \quad (29a)$$

$$p_x = p_\beta \cos \gamma - (p_\gamma/\beta) \sin \gamma \quad , \quad p_y = (p_\gamma/\beta) \cos \gamma + p_\beta \sin \gamma . \quad (29b)$$

Using the relations

$$p_\gamma = xp_y - yp_x \quad , \quad \beta p_\beta = xp_x + yp_y \quad , \quad \beta^2 = x^2 + y^2 \quad , \quad \beta^3 \cos 3\gamma = x^3 - 3xy^2 \quad , \quad (30a)$$

$$(p_\gamma^2/\beta - \beta p_\beta^2) \cos 3\gamma + 2p_\beta p_\gamma \sin 3\gamma = x(p_y^2 - p_x^2) + 2yp_x p_y \quad , \quad (30b)$$

$$\mathcal{H}_{d,0} \equiv (T + x^2 + y^2)/2 \quad , \quad T = p_x^2 + p_y^2 \quad , \quad (30c)$$

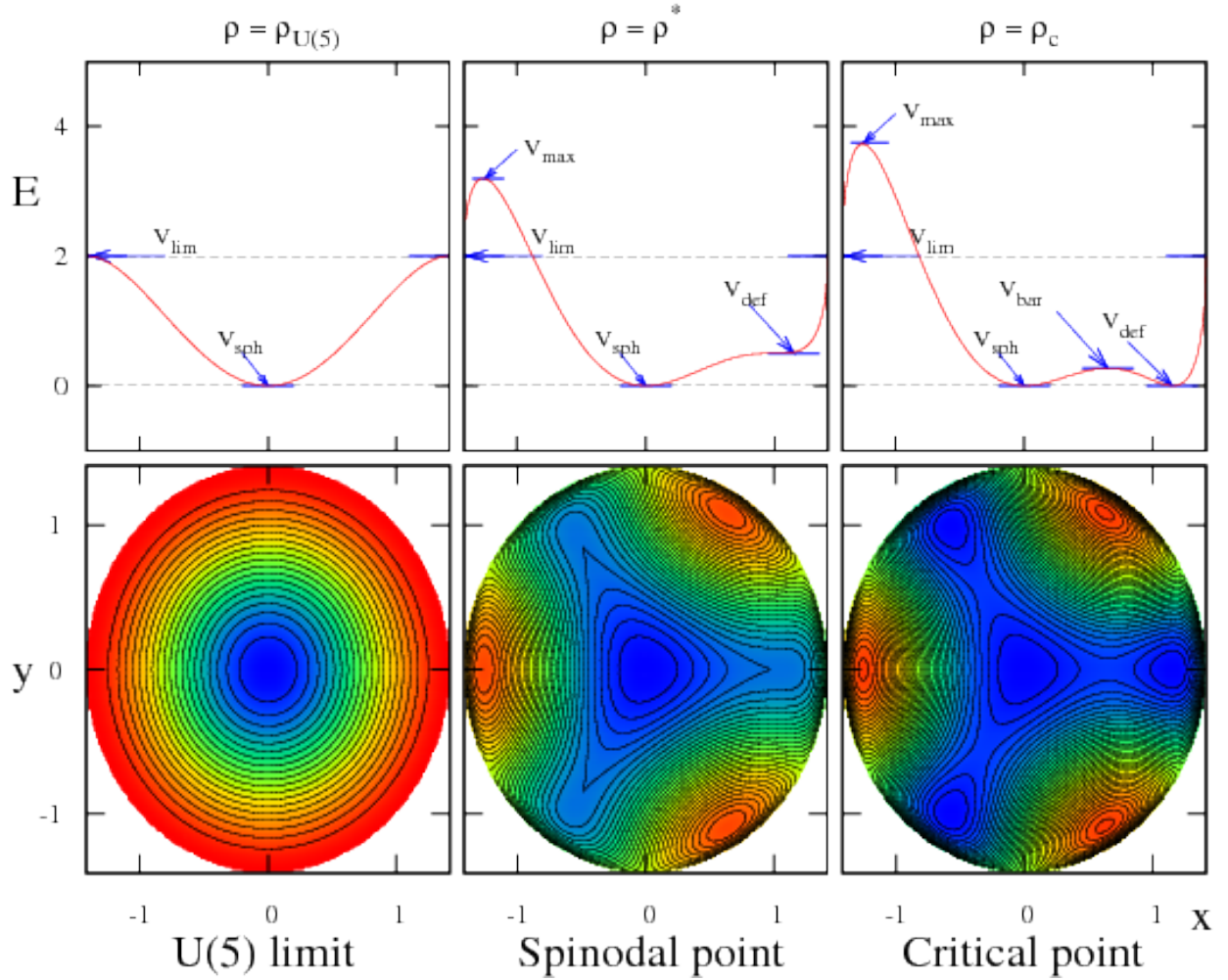


Figure 1: Contour plots of the potential  $V_1(\rho; x, y)$ , Eq. (31a), [lower portion], and the section  $V_1(\rho; x, y = 0)$  [upper portion], for  $\beta_0 = \sqrt{2}$ ,  $h_2 = 1$ , relevant to the spherical side of the QPT ( $0 \leq \rho \leq \rho_c$ ). Here  $\rho_{U(5)} = 0$  corresponds to the U(5) limit,  $\rho^*$  the spinodal point, Eq. (34), and  $\rho_c$  the critical point, Eq. (33). The stationary values ( $V_{\text{sph}}, V_{\text{def}}, V_{\text{bar}}, V_{\text{sad}}, V_{\text{max}}$ ) and boundary values ( $V_{\text{lim}}$ ) of  $V_1(\rho; x, y)$  are marked by arrows. The energy scale of the color coding in the contour plots can be inferred from the respective panels above them.

one can express the classical Hamiltonians of Eq. (26) in terms of  $(x, y, p_x, p_y)$ . Setting  $p_x = p_y = 0$  in the resulting expressions, we obtain the classical potential of Eq. (28) in Cartesian form

$$V_1(\rho)/h_2 = \beta_0^2(x^2 + y^2) - \rho\beta_0^2\sqrt{2 - (x^2 + y^2)} [x^3 - 3xy^2] + \frac{1}{2}(1 - \beta_0^2)(x^2 + y^2)^2, \quad (31a)$$

$$V_2(\xi)/h_2 = \beta_0^2 [1 - \xi(1 + \beta_0^2)] (x^2 + y^2) - \beta_0\sqrt{2 - (x^2 + y^2)} [x^3 - 3xy^2] + \frac{1}{4} [2(1 - \beta_0^2) + \xi(1 + \beta_0^2)^2] (x^2 + y^2)^2 + \xi\beta_0^4. \quad (31b)$$



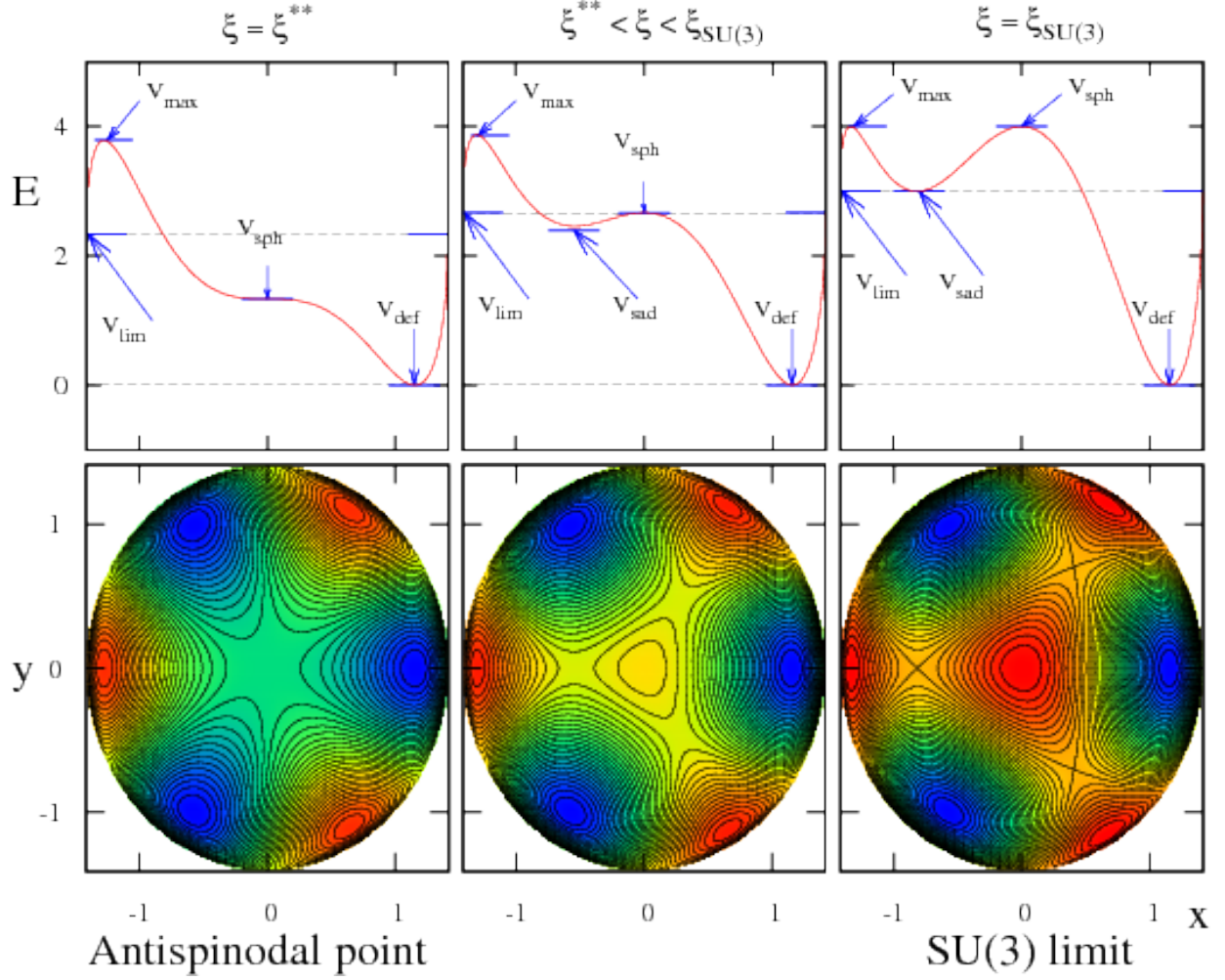


Figure 2: Same as in Fig. 1, but for the potential  $V_2(\xi; x, y)$ , Eq. (31b), [lower portion], and the section  $V_2(\xi; x, y = 0)$  [upper portion], relevant to the deformed side of the QPT ( $\xi^{**} \leq \xi \leq 1$ ). Here  $\xi^{**}$  denotes the anti-spinodal point, Eq. (35), and  $\xi_{\text{SU}(3)} = 1$  corresponds to the SU(3) limit.

Note that the potentials  $V(\beta, \gamma) = V(x, y)$  depend on the combinations  $\beta^2 = x^2 + y^2$ ,  $\beta^4 = (x^2 + y^2)^2$  and  $\beta^3 \cos 3\gamma = x^3 - 3xy^2$ .

The classical limit of the collective Hamiltonian, Eq. (6), constrained to  $L = 0$ , is obtained in a similar manner and is given by

$$\begin{aligned} \mathcal{H}_{\text{col}} &= c_5 p_\gamma^2 + c_6 (-T^2 + 2T - \beta^2 p_\beta^2) \\ &= c_5 (xp_y - yp_x)^2 + c_6 [-T^2 + 2T - (xp_x + yp_y)^2] , \end{aligned} \quad (32)$$

where  $T = p_\beta^2 + p_\gamma^2 / \beta^2 = p_x^2 + p_y^2$ . The O(3)-rotational  $c_3$ -term is absent from Eq. (32), since the classical Hamiltonian is constrained to angular momentum zero. The purely kinetic character of the collective terms is evident from the fact that  $\mathcal{H}_{\text{col}}$  vanishes for  $p_\beta = p_\gamma = 0$ , thus not contributing to the potential  $V(\beta, \gamma)$ .

#### 4.2. Topology of the classical potentials

The values of the control parameters  $\rho$  and  $\xi$  determine the landscape and extremal points of the potentials  $V_1(\rho; \beta, \gamma)$  and  $V_2(\xi; \beta, \gamma)$ , Eq. (28). Important values of these parameters at which a pronounced change in structure is observed, are the spinodal point where a second (deformed) minimum occurs, an anti-spinodal point where the first (spherical) minimum disappears and a critical point in-between, where the two minima are degenerate. For the potentials under discussion, the critical point  $(\rho_c, \xi_c)$  given by

$$\rho_c = \beta_0^{-1} \quad \text{and} \quad \xi_c = 0, \quad (33)$$

separates the spherical and deformed phases. The spinodal point  $(\rho^*)$

$$\rho^* = \frac{1}{\sqrt{6}} \left[ -(r^2 - 4r + 1) + (r + 1)\sqrt{(r + 1)(r - 1/3)} \right]^{1/2}, \quad r \equiv \beta_0^{-2}, \quad (34)$$

and the anti-spinodal point  $(\xi^{**})$

$$\xi^{**} = (1 + \beta_0^2)^{-1}, \quad (35)$$

embrace the critical point and mark the boundary of the phase coexistence region. The derivation of these expressions is explained in Appendix A.

In general, the only  $\gamma$ -dependence in the potentials (28) is due to the  $\sqrt{2 - \beta^2}\beta^3 \cos 3\gamma$  term. This induces a three-fold symmetry about the origin  $\beta = 0$ , as is evident in the contour plots of the potentials shown in Figs 1-2. As a consequence, the deformed extremal points are obtained for  $\gamma = 0, \frac{2\pi}{3}, \frac{4\pi}{3}$  (prolate shapes), or  $\gamma = \frac{\pi}{3}, \pi, \frac{5\pi}{3}$  (oblate shapes). It is therefore possible to restrict the analysis to  $\gamma = 0$  and allow for both positive and negative values of  $\beta$ , corresponding to prolate and oblate deformations, respectively. Henceforth, we occasionally use the shorthand notation,  $V_1(\rho; \beta) \equiv V_1(\rho; \beta, \gamma = 0)$  and  $V_2(\xi; \beta) \equiv V_2(\xi; \beta, \gamma = 0)$ . These  $\gamma = 0$  sections are shown in the upper portion of Figs. 1-2.

*The spherical phase* ( $0 \leq \rho \leq \rho_c = \beta_0^{-1}$ ).

The relevant potential in the spherical phase is  $V_1(\rho; \beta, \gamma)$ , Eq. (28a), with  $0 \leq \rho \leq \rho_c$ . In this case,  $\beta = 0$  is a global minimum of the potential at an energy  $V_{\text{sph}}$ , representing the equilibrium spherical shape,

$$\beta_{\text{eq}} = 0 : \quad V_{\text{sph}} = V_1(\rho; \beta_{\text{eq}} = 0, \gamma) = 0. \quad (36)$$

The limiting value at the domain boundary is

$$V_{\text{lim}} = V_1(\rho; \beta = \sqrt{2}, \gamma) = 2h_2. \quad (37)$$

For  $\rho = 0$ , the potential is independent of  $\gamma$ ,

$$V_1(\rho = 0)/h_2 = \beta_0^2 \beta^2 + \frac{1}{2}(1 - \beta_0^2)\beta^4, \quad (38)$$

and has  $\beta_{\text{eq}} = 0$  as a single minimum.

For  $\rho > 0$ , the deformed extremal points ( $\beta \neq 0$ ) are given by

$$\beta = \sqrt{2}\tilde{\beta}(1 + \tilde{\beta}^2)^{-1/2}, \quad (39)$$

where  $\tilde{\beta}$  are real solutions of the cubic equation

$$\rho\tilde{\beta}^3 + 3\eta\tilde{\beta}^2 - 3\rho\tilde{\beta} + 1 = 0, \quad \eta = (2 - \beta_0^2)/3\beta_0^2. \quad (40)$$

For  $\rho < \rho^*$ , Eq. (40) has one real root,  $\tilde{\beta}_1 < 0$ . The corresponding deformation,  $\beta_1 < 0$ , obtained from Eq. (39), produces a maximum in  $V_1(\rho; \beta)$  at an energy  $V_{\max} = F_1(\rho, \tilde{\beta}_1)$ , where

$$F_1(\rho; \tilde{\beta})/h_2 = \beta_0^2(1 + \tilde{\beta}^2)^{-1}\tilde{\beta}^2(1 - \rho\tilde{\beta}). \quad (41)$$

At the spinodal point,  $\rho = \rho^*$ , Eq. (40) has one negative root ( $\tilde{\beta}_1 < 0$ ) and a doubly-degenerate positive root ( $\tilde{\beta}_2 > 0$ ), given by

$$\tilde{\beta}_1 = -2\sqrt{1 + (\eta/\rho^*)^2} - \eta/\rho^*, \quad (42a)$$

$$\tilde{\beta}_2 = \sqrt{1 + (\eta/\rho^*)^2} - \eta/\rho^*. \quad (42b)$$

The corresponding deformations  $\beta_1 < 0$  and  $\beta_2 > 0$ , obtained from Eq. (39), correspond to a maximum of the potential at an energy  $V_{\max} = F_1(\rho^*; \tilde{\beta}_1)$ , and to an inflection point at an energy  $V_{\text{def}} = F_1(\rho^*; \tilde{\beta}_2)$ , respectively.

For  $\rho > \rho^*$ , Eq. (40) has three distinct real roots,  $\tilde{\beta}_1 < \tilde{\beta}_2 < \tilde{\beta}_3$ , satisfying  $\tilde{\beta}_1 + \tilde{\beta}_2 + \tilde{\beta}_3 = -3\eta/\rho$ ,  $\tilde{\beta}_1\tilde{\beta}_2 + \tilde{\beta}_2\tilde{\beta}_3 + \tilde{\beta}_3\tilde{\beta}_1 = -3$  and  $\tilde{\beta}_1\tilde{\beta}_2\tilde{\beta}_3 = \rho^{-1}$ . The extremal points ( $\beta_1 < 0$ ,  $\beta_2 > 0$  and  $\beta_3 > 0$ ) obtained from Eq. (39), correspond to a maximum, a saddle and a minimum point of  $V_1(\rho, \beta)$ , at energies  $V_{\max} = F_1(\rho; \tilde{\beta}_1)$ ,  $V_{\text{bar}} = F_1(\rho; \tilde{\beta}_2)$ , and  $V_{\text{def}} = F_1(\rho; \tilde{\beta}_3)$ , respectively. The saddle point ( $\beta_2$ ) forms a barrier between the newly-developed local deformed minimum ( $\beta_3$ ) and the global minimum at  $\beta_{\text{eq}} = 0$ . As seen in the contour plot of Fig. 1, the potential near the saddle point decreases towards the spherical and prolate-deformed minima, and increases towards the two-out-of-three equivalent oblate-deformed maxima. Thus a barrier in the  $\beta$ -direction at the saddle point, separates the spherical and deformed phases.

*The deformed phase* ( $\xi \geq \xi_c = 0$ ).

The relevant potential in the deformed phase is  $V_2(\xi; \beta, \gamma)$ , Eq. (28b), with  $\xi \geq \xi_c$ . In this case,  $[\beta_{\text{eq}} > 0, \gamma_{\text{eq}} = 0]$  is a global minimum of the potential at an energy  $V_{\text{def}}$ , representing the equilibrium deformed shape

$$[\beta_{\text{eq}} = \sqrt{2}\beta_0(1 + \beta_0^2)^{-1/2}, \gamma_{\text{eq}} = 0]: \quad V_{\text{def}} = V_2(\xi; \beta_{\text{eq}} > 0, \gamma_{\text{eq}} = 0) = 0. \quad (43)$$

The limiting value of the domain boundary is

$$V_{\text{lim}} = V_2(\xi; \beta = \sqrt{2}, \gamma) = (2 + \xi)h_2. \quad (44)$$

$\beta = 0$  is an extremal point and occurs at an energy  $V_{\text{sph}}$

$$\beta = 0: \quad V_{\text{sph}} = V_2(\xi; \beta = 0, \gamma) = h_2\xi\beta_0^4. \quad (45)$$

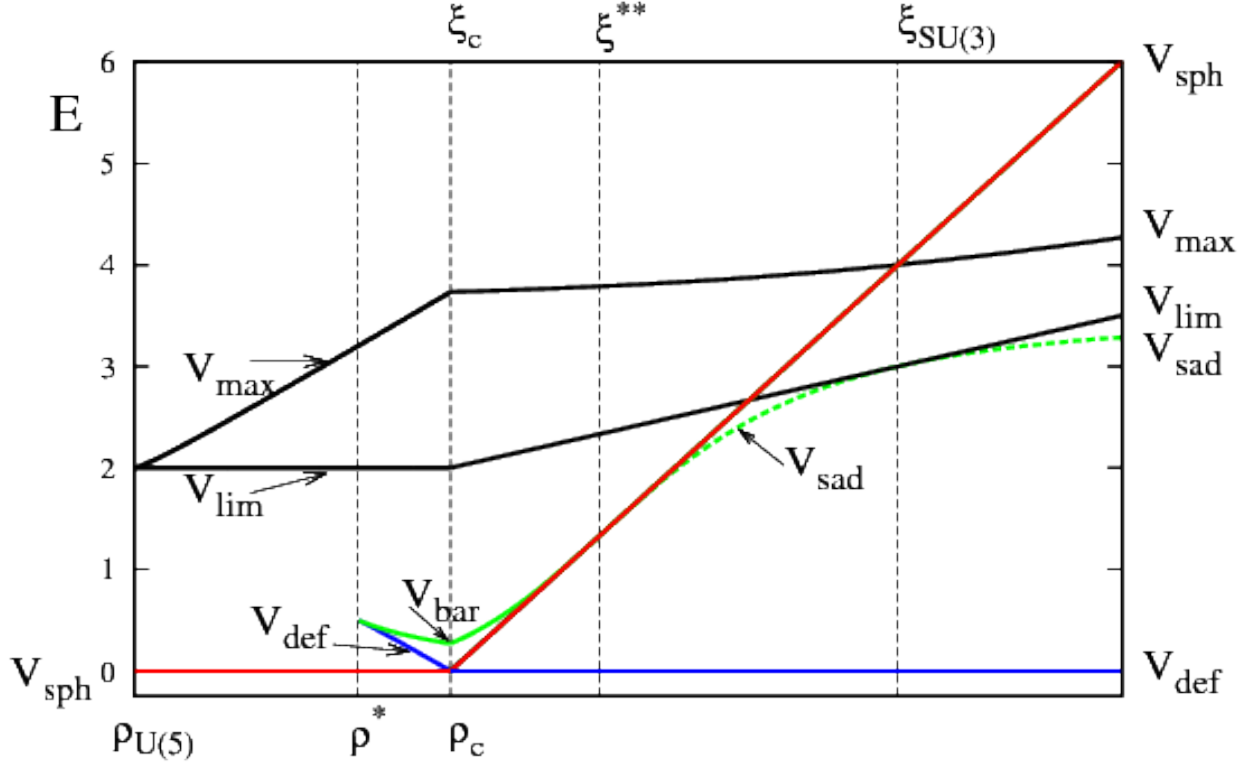


Figure 3: Evolution of the stationary and boundary values of the potential surfaces  $V_1(\rho)$  and  $V_2(\xi)$ , Eq. (28), with  $\beta_0 = \sqrt{2}$ ,  $h_2 = 1$ .  $\rho_{U(5)} = 0$  and  $\xi_{SU(3)} = 1$  correspond to the U(5) and SU(3) limits, respectively.  $V_{\text{lim}} = V(\beta = \sqrt{2}, \gamma)$  are the domain boundaries.  $V_{\text{sph}}$  is the energy of the spherical configuration which is a global minimum for  $0 \leq \rho < \rho_c$  and a local minimum for  $\xi_c \leq \xi < \xi^{**}$ . For  $\rho > 0$ , a deformed maximum occurs at an energy  $V_{\text{max}}$ . Beyond the spinodal point,  $\rho > \rho^*$ , a local deformed minimum at an energy  $V_{\text{def}}$  develops, along with a saddle point which creates a barrier of height  $V_{\text{bar}}$  separating the two minima. The latter cross and become degenerate ( $V_{\text{sph}} = V_{\text{def}}$ ) at the critical point  $(\rho_c, \xi_c)$ . At the anti-spinodal point,  $\xi^{**}$ , the spherical configuration changes from a minimum to a maximum, the deformed configuration remains a single minimum (energy  $V_{\text{def}}$ ) and the saddle point (energy  $V_{\text{sad}}$ ), now separates pairs of equivalent deformed minima (see Fig. 2). Note that  $V_{\text{bar}} = V_{\text{def}}$  at  $\rho^*$  and  $V_{\text{bar}} = V_{\text{sph}}$  at  $\xi^{**}$ . The relations  $V_{\text{sph}} = V_{\text{max}}$  and  $V_{\text{sad}} = V_{\text{lim}}$  at  $\xi_{SU(3)} = 1$  are a specific property of the SU(3) surface.

It is a local minimum for  $\xi < \xi^{**}$  and a maximum for  $\xi > \xi^{**}$ . The deformed extremal points ( $\beta \neq 0$ ) are given by  $\beta = \sqrt{2}\tilde{\beta}(1 + \tilde{\beta}^2)^{-1/2}$ , where  $\tilde{\beta}$  satisfies the following cubic equation,

$$\beta_0 \tilde{\beta}^3 + [2 - \beta_0^2 + \xi(1 + \beta_0^2)]\tilde{\beta}^2 - 3\beta_0 \tilde{\beta} + \beta_0^2[1 - \xi(1 + \beta_0^2)] = 0. \quad (46)$$

One solution of Eq. (46) is  $\tilde{\beta} = \beta_0$ , which yields the global deformed minimum,  $\beta_{\text{eq}} = \sqrt{2}\beta_0(1 + \beta_0^2)^{-1/2}$ , Eq. (43). The remaining solutions ( $\tilde{\beta} = \tilde{\beta}_{\pm}$ ) satisfy the quadratic equation,

$$\beta_0 \tilde{\beta}^2 + [2 + \xi(1 + \beta_0^2)]\tilde{\beta} + \beta_0[\xi(1 + \beta_0^2) - 1] = 0, \quad (47)$$

and determine two additional deformed extremal points,  $\beta_{\pm} = \sqrt{2}\tilde{\beta}_{\pm}(1 + \tilde{\beta}_{\pm}^2)^{-1/2}$ .

At the critical point ( $\xi_c = 0$ ,  $\rho_c = \beta_0^{-1}$ ), the potentials in the spherical and deformed phases coincide  $V_2(\xi_c; \beta, \gamma) = V_1(\rho_c; \beta, \gamma) \equiv V_{\text{cri}}(\beta, \gamma)$ , and read

$$V_{\text{cri}}(\beta, \gamma)/h_2 = \beta_0^2 \beta^2 - \beta_0 \sqrt{2 - \beta^2} \beta^3 \cos 3\gamma + \frac{1}{2}(1 - \beta_0^2) \beta^4 . \quad (48)$$

The topology of  $V_{\text{cri}}(\beta, \gamma)$  is shown on the right panel in Fig. 1. In this case, the global deformed minimum ( $\beta_{\text{eq}} > 0$ ) of Eq. (43), is degenerate with the spherical minimum ( $\beta = 0$ ), and both occur at zero energy,

$$V_{\text{cri}}(\beta = 0, \gamma) = V_{\text{cri}}(\beta_{\text{eq}} > 0, \gamma_{\text{eq}} = 0) = 0 . \quad (49)$$

The two solutions of Eq. (47), for  $\xi_c = 0$ , are  $\tilde{\beta}_{\pm} = [-1 \pm \sqrt{1 + \beta_0^2}]/\beta_0$  and the resulting additional deformed extremal points,  $\beta_{\pm} = \sqrt{2} \tilde{\beta}_{\pm} (1 + \tilde{\beta}_{\pm}^2)^{-1/2}$ , are found to be

$$\beta_{\pm} = \pm [1 \mp (1 + \beta_0^2)^{-1/2}]^{1/2} . \quad (50)$$

Here  $\beta_- < 0$  corresponds to a maximum of  $V_{\text{cri}}(\beta, \gamma = 0)$  and occurs at an energy  $V_{\text{max}}$

$$V_{\text{max}} = V_{\text{cri}}(\beta_-, \gamma = 0) = \frac{1}{2} h_2 \left( 1 + \sqrt{1 + \beta_0^2} \right)^2 . \quad (51)$$

$\beta_+ > 0$  corresponds to a saddle point, which creates a barrier of height  $V_{\text{bar}}$ ,

$$V_{\text{bar}} = V_{\text{cri}}(\beta_+, \gamma = 0) = \frac{1}{2} h_2 \left( 1 - \sqrt{1 + \beta_0^2} \right)^2 , \quad (52)$$

separating the spherical and deformed minima. The height and width of the barrier are governed by  $\beta_0$ .

For  $\xi > \xi_c$ , the spherical  $\beta = 0$  minimum turns local with an energy  $V_{\text{sph}} > 0$ , Eq. (45), above that of the deformed minimum [ $\beta_{\text{eq}} > 0$ ,  $\gamma_{\text{eq}} = 0$ ], Eq. (43). The additional deformed extremal points,  $\beta_{\pm} = \sqrt{2} \tilde{\beta}_{\pm} (1 + \tilde{\beta}_{\pm}^2)^{-1/2}$ , are determined by the solutions of Eq. (47)

$$\tilde{\beta}_{\pm} = \frac{-[2 + \xi(1 + \beta_0^2)] \pm \sqrt{\Delta}}{2\beta_0} , \quad (53a)$$

$$\Delta = (1 + \beta_0^2) [4 + 4\xi(1 - \beta_0^2) + \xi^2(1 + \beta_0^2)] . \quad (53b)$$

The two solutions  $\tilde{\beta}_{\pm}$  satisfy,  $\tilde{\beta}_- + \tilde{\beta}_+ = -[2 + \xi(1 - \beta_0^2)]/\beta_0$  and  $\tilde{\beta}_- \tilde{\beta}_+ = \xi(1 + \beta_0^2) - 1$ . The extremal point  $\beta_-$  corresponds to a maximum of the potential at an energy  $V_{\text{max}}$ , and  $\beta_+$  is a saddle point at an energy  $V_{\text{sad}}$ , given by

$$\beta_- = \sqrt{2} \tilde{\beta}_- (1 + \tilde{\beta}_-^2)^{-1/2} : \quad V_{\text{max}} = V_2(\beta_-, \gamma = 0) = F_2(\tilde{\beta}_-) , \quad (54a)$$

$$\beta_+ = \sqrt{2} \tilde{\beta}_+ (1 + \tilde{\beta}_+^2)^{-1/2} : \quad V_{\text{sad}} = V_2(\beta_+, \gamma = 0) = F_2(\tilde{\beta}_+) , \quad (54b)$$

where

$$F_2(\tilde{\beta})/h_2 = \frac{1}{2} \beta_0^2 \tilde{\beta}^2 + \frac{1}{2} \xi \beta_0 (1 + \beta_0^2) (1 + \tilde{\beta}^2)^{-1} \tilde{\beta}^2 (\tilde{\beta}_{\pm} - \beta_0) + \xi \beta_0^4 . \quad (55)$$

Table 2: Significant values of the control parameters  $(\rho, \xi)$  and order parameters,  $(\beta_{\text{eq}}, \gamma_{\text{eq}})$  for a first order QPT between a spherical [U(5)] phase and an axially-deformed [SU(3)] phase. The relevant intrinsic Hamiltonians are  $\hat{H}_1(\rho)$ , Eq. (7a) and  $\hat{H}_2(\xi)$ , Eq. (7b) with  $\beta_0 = \sqrt{2}$ . At the critical point, the barrier height is  $V_{\text{bar}} = 0.268h_2$ , and the domain boundary is  $V_{\text{lim}} = 2h_2$ .

Special points	Control parameters	Order parameters
Spherical phase	$0 \leq \rho \leq \frac{1}{\sqrt{2}}$	$\beta_{\text{eq}} = 0$
Deformed phase	$0 \leq \xi \leq 1$	$[\beta_{\text{eq}} = \frac{2}{\sqrt{3}}, \gamma_{\text{eq}} = 0]$
U(5) DS	$\rho_{\text{U(5)}} = 0$	
Spinodal point	$\rho^* = \frac{1}{2}$	
Critical point	$\rho_c = \frac{1}{\sqrt{2}}, \xi_c = 0$	
Anti-spinodal point	$\xi^{**} = \frac{1}{3}$	
SU(3) DS	$\xi_{\text{SU(3)}} = 1$	

For  $0 \leq \xi < \xi^{**}$ , the local spherical minimum, Eq. (45), coexists with the deformed global minimum, Eq. (43), and  $\beta_- \beta_+ < 0$ . At the anti-spinodal point,  $\xi = \xi^{**}$ , the spherical minimum disappears and  $\beta = 0$  becomes an inflection point. For  $\xi > \xi^{**}$ ,  $\beta = 0$  becomes a maximum,  $[\beta_{\text{eq}} > 0, \gamma_{\text{eq}} = 0]$  remains a single minimum of the potential, and  $\beta_- \beta_+ > 0$ . In this case, as seen in the contour plot in Fig. 2, the potential near the saddle point ( $\beta_+$ ) increases both towards the spherical maximum ( $\beta = 0$ ) and the oblate-deformed maximum ( $\beta_-$ ), and decreases towards the two-out-of-three equivalent prolate-deformed global minima ( $\beta_{\text{eq}} > 0$ ). The saddle point has now a different character from that encountered in the coexistence region, accommodating a barrier in the  $\gamma$ -direction between pairs of equivalent prolate-deformed minima.

The evolution of the various stationary and asymptotic values of the Landau potentials ( $V_{\text{sph}}, V_{\text{max}}, V_{\text{def}}, V_{\text{bar}}, V_{\text{sad}}, V_{\text{lim}}$ ) as a function of the control parameters  $\rho$  and  $\xi$ , is depicted in Fig. 3. Most of these quantities, depend also on the parameter  $\beta_0$  of the Hamiltonian (7). In particular,  $\beta_0$  determines the equilibrium deformation in the deformed phase  $\beta_{\text{eq}} > 0$ , Eq. (43), the height of the barrier at the critical point  $V_{\text{bar}}$ , Eq. (52), and the width of the coexistence region through the values of the spinodal point  $\rho^*$ , Eq. (34), and anti-spinodal point  $\xi^{**}$ , Eq. (35). In the present work, we choose  $\beta_0 = \sqrt{2}$ , for which the intrinsic Hamiltonian interpolates between the U(5) and SU(3) dynamical symmetries and various expressions simplify, since  $\eta = 0$  in Eq. (40). For convenience, Table 2 lists the values of the relevant control and order parameters when  $\beta_0 = \sqrt{2}$ .

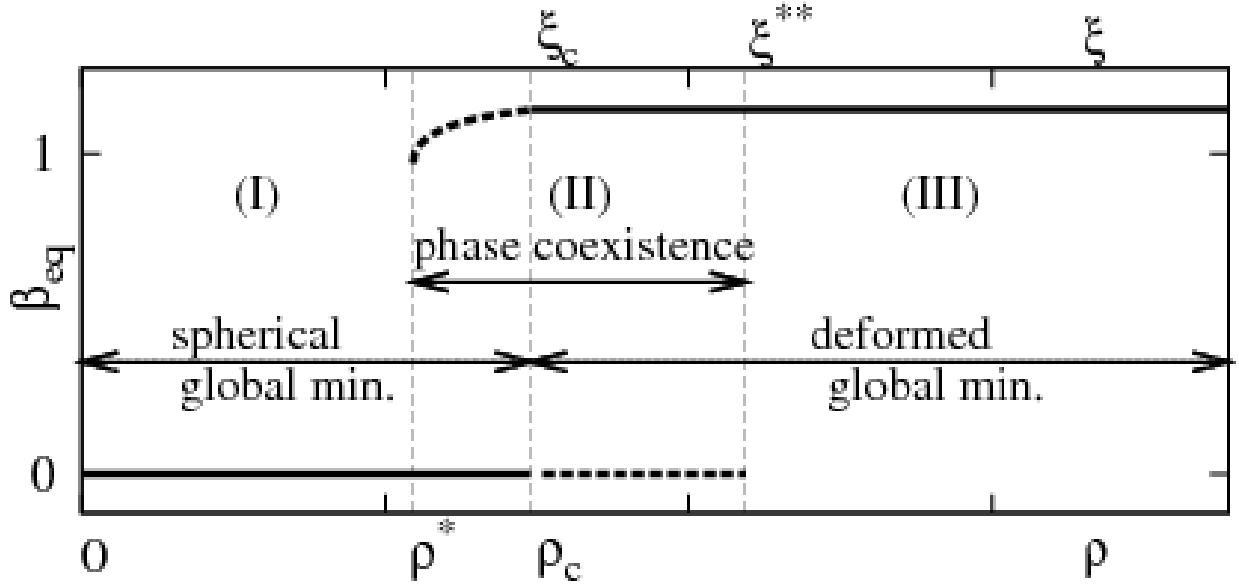


Figure 4: Behavior of the order parameter,  $\beta_{\text{eq}}$ , as a function of the control parameters  $(\rho, \xi)$  of the intrinsic Hamiltonian (7), with  $\beta_0 = \sqrt{2}$ . Here  $\rho^*$ ,  $(\rho_c, \xi_c)$ ,  $\xi^{**}$ , are the spinodal, critical and anti-spinodal points, respectively, with values given in Table 2. The deformation at the global (local) minimum of the Landau potential (28) is marked by solid (dashed) lines.  $\beta_{\text{eq}}=0$  ( $\beta_{\text{eq}} = \frac{2}{\sqrt{3}}$ ) on the spherical (deformed) side of the QPT. Region I (III) involves a single spherical (deformed) shape, while region II involves shape-coexistence.

#### 4.3. Structural regions of the QPT and order parameters

The preceding classical analysis of the potential surfaces has identified three regions with distinct structure.

- I. The region of a stable spherical phase,  $\rho \in [0, \rho^*]$ , where the potential has a single spherical minimum.
- II. The region of phase coexistence,  $\rho \in (\rho^*, \rho_c]$  and  $\xi \in [\xi_c, \xi^{**})$ , where the potential has both spherical and deformed minima which cross and become degenerate at the critical point.
- III. The region of a stable deformed phase,  $\xi \geq \xi^{**}$ , where the potential has a single deformed minimum.

The potential surface in each region serves as the Landau potential of the QPT, with the equilibrium deformations as order parameters. The latter evolve as a function of the control parameters  $(\rho, \xi)$  and exhibit a discontinuity typical of a first order transition. As depicted in Fig 4, the order parameter  $\beta_{\text{eq}}$  is a double-valued function in the coexistence region (in-between  $\rho^*$  and  $\xi^{**}$ ) and a step-function outside it. In what follows we examine the nature of the classical dynamics in each region.

## 5. Regularity and chaos: classical analysis

Hamiltonians with dynamical symmetry are always completely integrable [68]. The Casimir invariants of the algebras in the chain provide a complete set of constants of the motion in involution. The classical motion is purely regular. A dynamical symmetry-breaking is usually connected to non-integrability and may give rise to chaotic motion [68, 69, 70]. This is the situation encountered in a QPT, which occurs as a result of a competition between terms in the Hamiltonian with incompatible symmetries.

Regular and chaotic properties of the IBM have been studied extensively, employing various measures of classical and quantum chaos [44, 45, 46, 47, 48, 49, 50, 51]. All such treatments involved the simplified Hamiltonian of Eq. (13), giving rise to an extremely low barrier and narrow coexistence region. For that reason, the majority of studies focused on the regions I and III of stable phases, while far less effort was devoted to the dynamics inside the region II of phase-coexistence. Considerable attention has been paid to integrable paths (the U(5)-O(6) transition for  $\chi = 0$  in Eq. (13) [49, 50]) and to specific sets of parameters leading to an enhanced regularity (“arc of regularity” [46, 51]) within these regions. Similar type of analysis was performed in the framework of the geometric collective model of nuclei [71, 72, 73, 74, 75].

In the present work, we consider the evolution of order and chaos across a generic first order quantum phase transition, with particular emphasis on the role of a high barrier separating the two phases. For that purpose, we employ the intrinsic Hamiltonian of Eq. (7) with  $\beta_0 = \sqrt{2}$ . In this case, the height of the barrier at the critical point, Eq. (52), is  $V_{\text{bar}}/h_2 = 0.268$ , substantially higher than barrier heights encountered in previous works. In comparison, for the Hamiltonian of Eq. (14) with  $\chi = -\frac{\sqrt{2}}{2}$ , the corresponding quantities are  $\beta_0 = \frac{1}{2\sqrt{2}}$  and  $V_{\text{bar}}/h_2 = 0.0018$ . A high barrier will allow us to uncover a rich pattern of regularity and chaos in region II of shape-coexistence.

The classical dynamics of  $L=0$  vibrations, associated with the Hamiltonian (7), can be depicted conveniently via Poincaré surfaces of sections [9, 10, 11]. The latter are chosen in the plane  $y = 0$  which passes through all the various types of stationary points (minimum, maximum, saddle) in the Landau potential (28). The values of  $x$  and  $p_x$  are plotted each time a trajectory intersects the plane. The method of Poincaré sections provides a snapshot of the dynamics at a given energy. Regular trajectories are bound to toroidal manifolds within the phase space and their intersections with the plane of section lie on one-dimensional curves (ovals). In contrast, chaotic trajectories diverge exponentially and randomly cover kinematically accessible areas of the section. Although restricted to  $L = 0$ , the method is particularly valuable to the present study, due to its ability to identify different forms of dynamics occurring at the same energy in separate regions of phase space. Standard global classical measures of chaos, such as, the fraction of chaotic volume and the average largest Lyapunov exponent, are insensitive such local variations. We first discuss distinctive features of the dynamics in each region and relate them to the morphology of the Landau potential. This will provide the necessary background for understanding the complete evolution of the dynamics across the QPT.



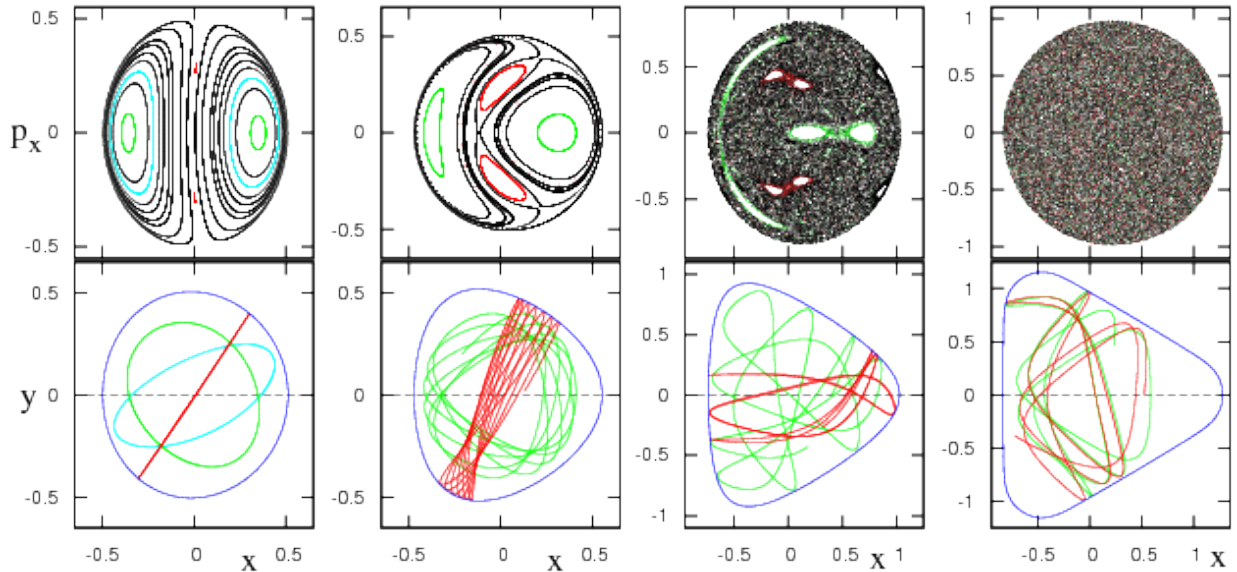


Figure 5: Classical dynamics of  $\mathcal{H}_1(\rho)$ , Eq. (26a) with  $\beta_0 = \sqrt{2}$ ,  $h_2 = 1$ , for several values of  $\rho$  and energies  $E$ , in the vicinity of a spherical minimum. Selected trajectories (bottom row) and corresponding Poincaré sections (top row), portray the motion in the presence of a single spherical minimum. (a)  $\rho = 0.03$ ,  $E = 0.5$ . (b)  $\rho = 0.2$ ,  $E = 0.5$ . (c)  $\rho = 0.2$ ,  $E = 1.114$ . (d)  $\rho = 0.2$ ,  $E = 1.5$ .

### 5.1. Characteristic features of the dynamics in the vicinity of minima

Considerable insight into the nature of the classical dynamics at low energy can be gained by examining the topology of the Landau potential in the vicinity of its minima. A sample of representative Poincaré sections for the classical Hamiltonian constrained to  $L = 0$ , Eq. (26), are depicted in Figs. 5-6, along with selected trajectories.

The spherical configuration ( $\beta = 0$ ) is a global minimum of the potential  $V_1(\rho; \beta, \gamma)$ , Eq. (28a), on the spherical side of the QPT ( $0 \leq \rho \leq \rho_c$ ). For  $\rho = 0$ , the system has  $U(5)$  DS and hence is integrable. The potential  $V_1(\rho = 0)$ , Eq. (38), is  $\gamma$ -independent and exhibits  $\beta^2$  and  $\beta^4$  dependence. As shown in Fig. 5(a), the sections, for small  $\rho$ , show the phase space portrait typical of a weakly perturbed anharmonic (quartic) oscillator with two major regular islands and quasi-periodic trajectories. The effect of increasing  $\rho$  on the dynamics in the vicinity of the spherical ( $s$ ) minimum ( $\beta \approx 0$ ), can be inferred from a small  $\beta$ -expansion of the potential,

$$V_{1,s}(\rho) \approx \beta_0^2 \beta^2 - \rho \sqrt{2} \beta_0^2 \beta^3 \cos 3\gamma. \quad (56)$$

To order  $\beta^3$ ,  $V_{1,s}(\rho)$  has the same functional form as the the well-known Hénon-Heiles (HH) potential [76], which in polar coordinates ( $r, \phi$ ) reads

$$V_{\text{HH}} = r^2 - \alpha r^3 \cos 3\phi, \quad (57)$$

with  $\alpha > 0$ . The latter potential serves as a paradigm of a system that exhibits a transition from regular to chaotic dynamics as the energy increases [9, 10, 11]. As shown for  $\rho=0.2$ , at

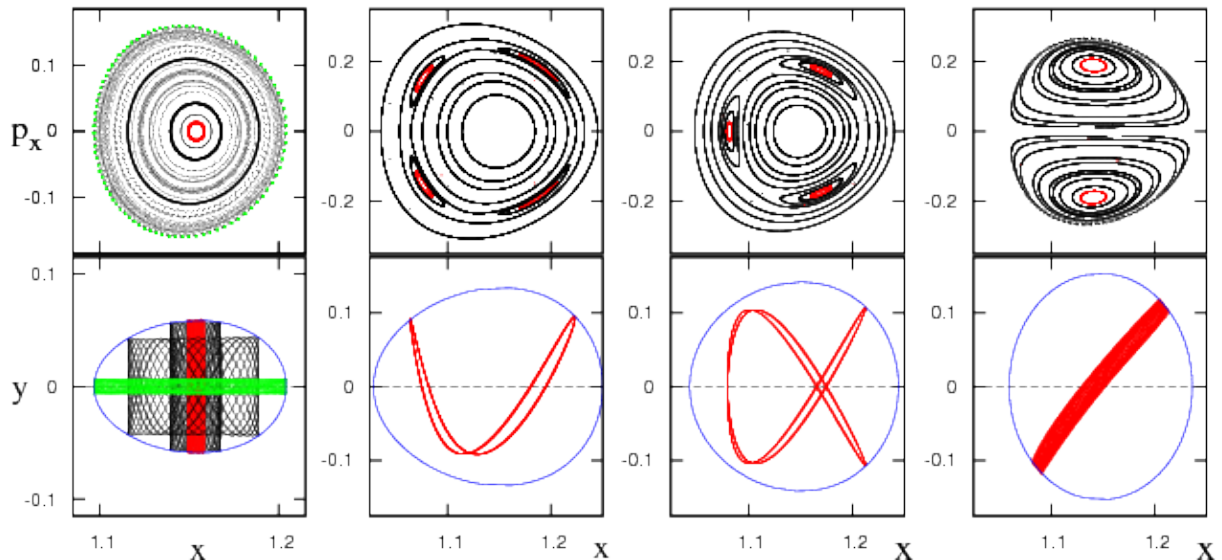


Figure 6: Classical dynamics of  $\mathcal{H}_2(\xi)$ , Eq. (26b) with  $\beta_0 = \sqrt{2}$ ,  $h_2 = 1$ , for several values of  $\xi$  and energies  $E$ , in the vicinity of a deformed minimum. Selected trajectories (bottom row) and corresponding Poincaré sections (top row), portray the motion in the presence of a single deformed minimum. (a)  $\xi = 0.11$ ,  $E = 0.02$ . (b)  $\xi = 0.258$ ,  $E = 0.11$ . (c)  $\xi = 0.505$ ,  $E = 0.12$ . (d)  $\xi = 1$ ,  $E = 0.15$ . Panel (a) shows a typical pattern encountered for most values of  $\xi \geq \xi^{**}$ . Panels (b)-(c)-(d) correspond to  $R = \epsilon_\beta/\epsilon_\gamma = 1/2, 2/3, 1$  in Eq. (59), and show the effect of local degeneracies of normal modes. Panel (d) corresponds to the SU(3) DS limit.

low energy [Fig. 5(b)], the dynamics remains regular, and two additional islands show up. The four major islands surround stable fixed points and unstable (hyperbolic) fixed points occur in-between. At higher energy [Fig. 5(c)], one observes a marked onset of chaos and an ergodic domain. This typical HH-type of behavior persists in the vicinity of the spherical minimum throughout the coexistence region, including the critical point  $(\rho_c, \xi_c)$  and beyond where the spherical minimum is only local ( $0 \leq \xi \leq \xi^{**}$ ). This can be inferred from a similar small  $\beta$ -expansion of the relevant potential  $V_2(\xi; \beta, \gamma)$ , Eq. (28b),

$$V_{2,s}(\xi) \approx \xi\beta_0^4 + \beta_0^2[1 - \xi(1 + \beta_0^2)]\beta^2 - \sqrt{2}\beta_0\beta^3 \cos 3\gamma. \quad (58)$$

It should be noted that although the expansions in Eqs. (56) and (58) are similar in form to the Hénon-Heiles potential (57), the full potentials, Eq. (28), have a finite domain and include a  $\beta^4$  term, thus ensuring that the motion is bounded at all energies.

The deformed configuration ( $\beta_{\text{eq}} > 0, \gamma_{\text{eq}} = 0$ ), Eq. (43), is a global minimum of the potential  $V_2(\xi; \beta, \gamma)$ , Eq. (28b), on the deformed side of the QPT ( $\xi \geq \xi_c$ ). The classical dynamics in its vicinity ( $x \approx 1$ ) has a very different character, being robustly regular. At low energy, the motion reflects the  $\beta$  and  $\gamma$  normal mode oscillations about the deformed minimum. As shown in Fig. 6(a), the family of regular trajectories has a particular simple structure. It forms a single set of concentric loops around a single stable (elliptic) fixed point. They portray  $\gamma$ -vibrations at the center of the surface ( $p_x \approx 0$ ) and  $\beta$ -vibrations at the perimeter (large  $|p_x|$ ). This regular pattern of the dynamics is found for most values of

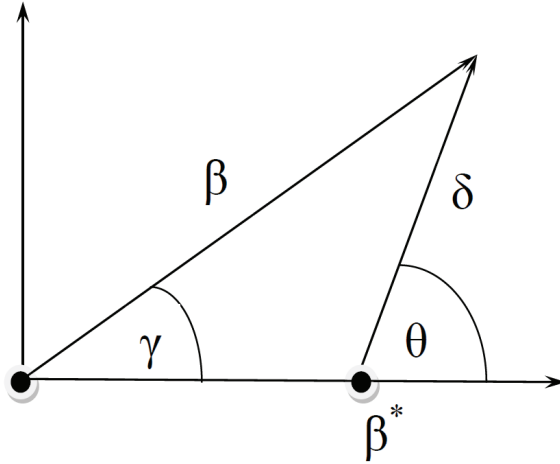


Figure 7: Local coordinates  $(\delta, \theta)$ , Eq. (60), about a deformed minimum  $(\beta^*, \gamma^* = 0)$ .

$\xi \geq 0$  both inside and outside the phase coexistence region. The dynamics remains regular but its pattern changes in the presence of resonances. The latter appear when the ratio of normal mode frequencies, Eq. (10), is a rational number

$$R \equiv \frac{\epsilon_\beta}{\epsilon_\gamma} = \frac{1}{9}(1 + \beta_0^2)(2\xi + 1) . \quad (59)$$

Panels (b)-(c)-(d) of Fig. 6 show examples of such scenario for  $\beta_0 = \sqrt{2}$  and  $\xi$ -values corresponding to  $R = 1/2, 2/3, 1$ . The corresponding surfaces exhibit four, three and two islands, respectively. The phase space portrait for  $(\xi = 1, R = 1)$ , shown in Fig. 6(d), corresponds to the integrable SU(3) DS limit. These additional chains of regular islands will be considered in more detail in Section 5.3.

Similar trends are observed in the region  $(\rho^* < \rho \leq \rho_c)$ , where the deformed minimum is only local. A regular dynamics is thus an inherent feature of a deformed minimum and, at low energy, reflects the behavior of the Landau potential in its vicinity. The structure of the latter is revealed in an expansion of the potential in local coordinates. Consider a deformed minimum (global or local) of the Landau potential characterized by the deformation  $(\beta^* > 0, \gamma^* = 0)$ . The local coordinates  $(\delta, \theta)$  about it, shown in Fig 7, are defined by the relations

$$\beta \cos \gamma = \beta^* + \delta \cos \theta , \quad (60a)$$

$$\beta \sin \gamma = \delta \sin \theta . \quad (60b)$$

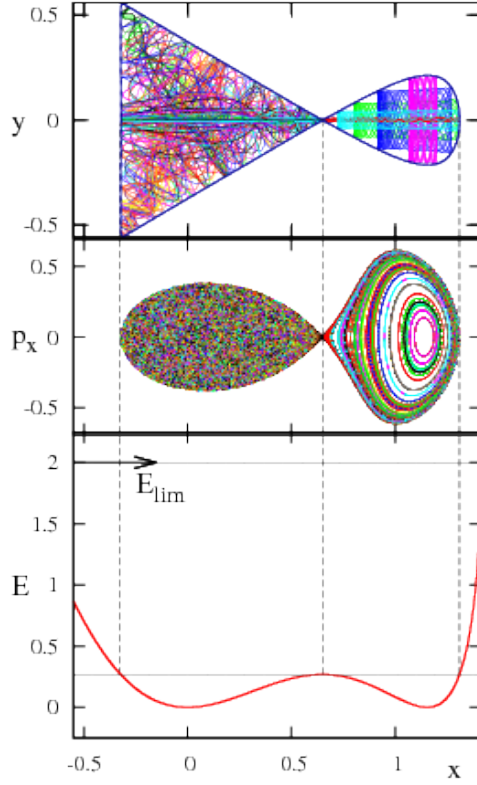


Figure 8: Classical dynamics of the critical point Hamiltonian,  $\mathcal{H}_{\text{cri}} = \mathcal{H}_1(\rho_c) = \mathcal{H}_2(\xi_c)$ , Eq. (26), at the energy of the barrier. The lower, middle, and upper portions depict  $V_{\text{cri}}(\beta, \gamma = 0)$ , Eq. (48), the Poincaré section and selected trajectories, respectively. The pattern of mixed but well-separated chaotic and regular dynamics, associated with the spherical and deformed minima, appears throughout the coexistence region.

A small  $\delta$ -expansion of the potential about this minimum (to order  $\delta^3$ ), reads

$$V(\beta, \gamma) \approx K_1 + \delta^2 (K_2 + K_3 \cos^2 \theta) + \delta^3 (K_4 \cos \theta + K_5 \cos^3 \theta) . \quad (61)$$

Here  $V(\beta, \gamma)$  stands for  $V_1(\rho; \beta, \gamma)$  in the spherical phase and  $V_2(\xi; \beta, \gamma)$  in the deformed phase. In general, the coefficients  $K_i$  depend on  $\beta^*$  and the control parameters, *e.g.*,  $K_1 = V(\beta^*, \gamma = 0)$ . In the deformed phase, where the deformed minimum is global,  $\beta^* = \beta_{\text{eq}} = \sqrt{2}\beta_0(1 + \beta_0^2)^{-1/2}$ , Eq. (43), and the  $K_i$  coefficients are given by

$$\begin{aligned} K_1 &= 0 \quad , \quad K_2 = \frac{9\beta_0^2}{1+\beta_0^2} \quad , \quad K_3 = \frac{\beta_0^2}{1+\beta_0^2} [(\beta_0^2 - 2)(\beta_0^2 + 4) + 2\xi(1 + \beta_0^2)^2] \quad , \\ K_4 &= \frac{\sqrt{2}\beta_0}{2\sqrt{1+\beta_0^2}} [(\beta_0^2 - 2)(\beta_0^2 - 5) + 2\xi(1 + \beta_0^2)^2] \quad , \\ K_5 &= \frac{\sqrt{2}\beta_0}{2\sqrt{1+\beta_0^2}} [(\beta_0^2 - 2)(\beta_0^2 + 2)^2 + \beta_0^2(\beta_0^2 + 16)] \quad . \end{aligned} \quad (62)$$

For  $\beta_0 = \sqrt{2}$ , these expressions simplify to

$$V_2(\xi) \approx 6\delta^2 [1 + 2\xi \cos^2 \theta] + 6\sqrt{3}\delta^3 [2 \cos^3 \theta + \xi \cos \theta] \quad . \quad (63)$$

The expansions in Eqs. (61) and (63) contain terms with  $\cos \theta$ ,  $\cos 2\theta$  and  $\cos 3\theta$  dependence. The presence of lower harmonics destroys, locally, the three-fold symmetry encountered near

the spherical minimum, Eqs. (56)-(58), due to the  $\cos 3\gamma$  term. This asymmetry is clearly seen in the contour plots of Figs. 1-2.

Both spherical and deformed minima of the Landau potentials  $V_1(\rho; \beta, \gamma)$  and  $V_2(\xi; \beta, \gamma)$ , are present in the coexistence region,  $\rho^* < \rho \leq \rho_c$  and  $\xi_c \leq \xi < \xi^{**}$ . In this case, each minimum preserves its own characteristic dynamics resulting in a marked separation between a Hénon-Heiles type of chaotic motion in the vicinity of the spherical minimum and a regular motion in the vicinity of the deformed minimum. Such mixed form of dynamics occurring at the same energy in different regions of phase space, is demonstrated in Fig. 8. The latter depicts the potential landscape at the critical point  $(\rho_c, \xi_c)$ , along with the Poincaré section and selected trajectories at the barrier energy. In this case, the spherical (s) and deformed (d) minima are degenerate, and for  $\beta_0 = \sqrt{2}$ , the expansions of the corresponding Landau potential in their vicinity exhibit a different morphology

$$V_{s,\text{cri}} \approx 2\beta^2 - 2\beta^3 \cos 3\gamma, \quad (64a)$$

$$V_{d,\text{cri}} \approx 6\delta^2 + 3\sqrt{3}\delta^3 [\cos 3\theta + 3 \cos \theta]. \quad (64b)$$

The critical-point potential near the spherical minimum ( $V_{s,\text{cri}}$ ) has a 3-fold symmetry and its contours are either concave or convex towards the origin (see Fig. 1). The former contours lead to divergence of trajectories, a characteristic property of chaotic motion. In contrast, the critical-point potential near the deformed minimum ( $V_{d,\text{cri}}$ ) has an egg-shape, without a local 3-fold symmetry. The potential contours are convex and tend to focus the trajectories towards the minimum, resulting in a confined regular motion.

### 5.2. Evolution of the classical dynamics across the QPT

We turn now to a comprehensive analysis of the classical dynamics, constraint to  $L = 0$ , evolving across the first order QPT. The evolution is accompanied by an intricate interplay of order and chaos, reflecting the change in structure. The shape-phase transition is induced by the intrinsic Hamiltonian of Eq. (7) with  $\beta_0 = \sqrt{2}$ . The Poincaré surfaces of sections, are shown in Figs. 9-10-11 for representative energies, below the domain boundary ( $V_{\text{lim}}$ ), and control parameters  $(\rho, \xi)$  in regions I-II-III, respectively. The surfaces record a total of 40,000 passages through the  $y = 0$  plane by 120 trajectories with randomly generated initial conditions, in order to scan the whole accessible phase space at a given energy. The bottom row in each figure displays the corresponding classical potential  $V(x, y = 0)$ , Eq. (31).

The classical dynamics of  $L = 0$  vibrations in the stable spherical phase (region I) is governed by the Hamiltonian  $\mathcal{H}_1(\rho)$ , Eq. (26a), with  $0 \leq \rho \leq \rho^*$ . The relevant potential  $V_1(\rho)$ , Eq. (31a), has a single minimum at  $(x, y) = (0, 0)$ . For  $\rho = 0$ , the quantum Hamiltonian  $\hat{H}_1(\rho = 0)$ , Eq. (16), has U(5) DS and its classical counterpart,  $\mathcal{H}_1(\rho = 0) = \mathcal{H}_{d,0}(2 - \mathcal{H}_{d,0})$ , involves the 2D harmonic oscillator Hamiltonian,  $\mathcal{H}_{d,0} = (p_x^2 + p_y^2 + x^2 + y^2)/2$ . The system is completely integrable. The orbits are periodic and, as shown in Fig. 9, appear in the surface of section as a finite collection of points. As previously noted, for small values of  $\rho$  ( $\rho = 0.03$  in Fig. 9), the sections are those of an anharmonic (quartic) oscillator, weakly perturbed by the small  $\rho(x^3 - 3x^2y)$  term. The orbits are quasi-periodic and appear as smooth one-dimensional invariant curves. For larger values of  $\rho$ , the importance of the latter perturbation increases. The derived phase-space portrait near  $x = 0$ , shown for  $\rho = 0.2$  in Fig. 9,

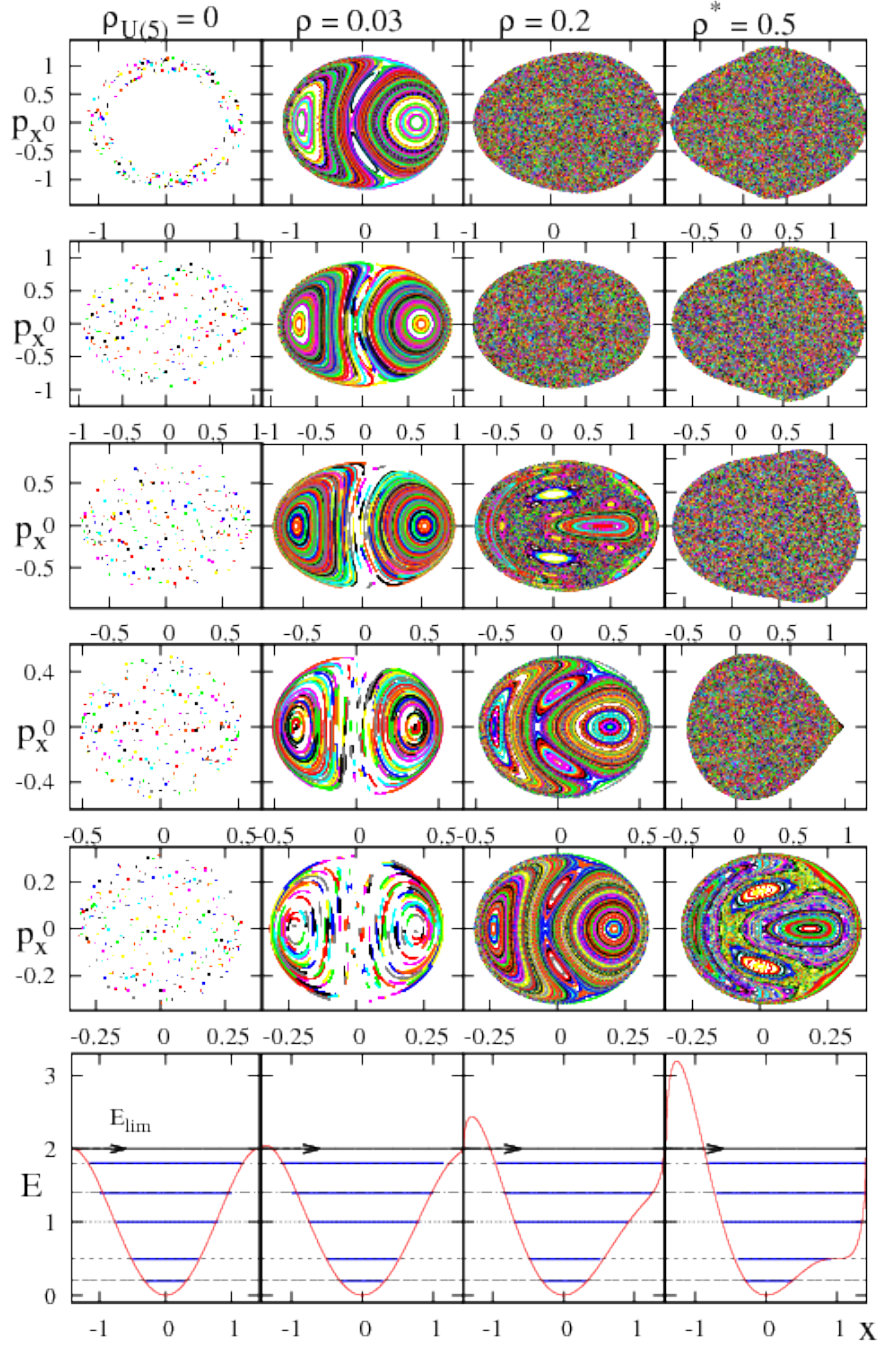


Figure 9: Poincaré sections in the stable spherical phase (region I). Upper five rows depict the classical dynamics of  $\mathcal{H}_1(\rho)$  (26a) with  $h_2 = 1$  and  $\beta_0 = \sqrt{2}$ , for several values of  $\rho \leq \rho^{**}$ . The bottom row displays the corresponding classical potentials  $V_1(\rho; x, y = 0)$  (31a). The five energies, below  $E_{lim} = 2h_2$ , at which the sections were calculated consecutively, are indicated by horizontal lines. The left column ( $\rho_{U(5)} = 0$ ) corresponds to the integrable U(5) DS limit. The right column ( $\rho^*$ ) corresponds to the spinodal point.



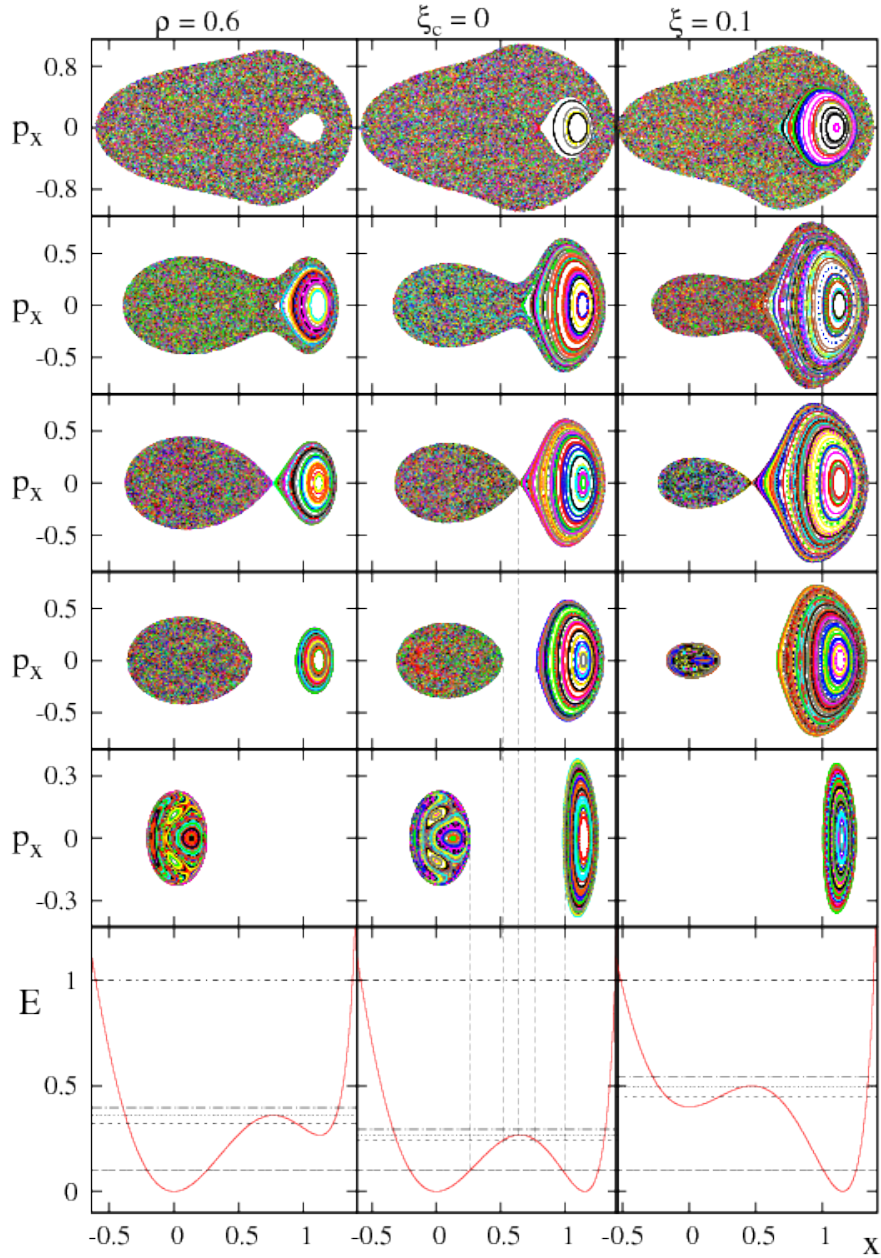


Figure 10: Poincaré sections in the region of phase-coexistence (region II). The panels are as in Fig. 9, but for  $\mathcal{H}_1(\rho)$  (26a) with  $\rho^{**} < \rho \leq \rho_c$ , and  $\mathcal{H}_2(\xi)$  (26b) with  $\xi_c \leq \xi < \xi^{**}$ . The classical potentials are  $V_1(\rho; x, y = 0)$  (31a) and  $V_2(\xi; x, y = 0)$  (31b), respectively. The middle column corresponds to the critical point  $(\rho_c, \xi_c)$ , and the vertical lines mark the turning points for energies below or equal to the barrier height.

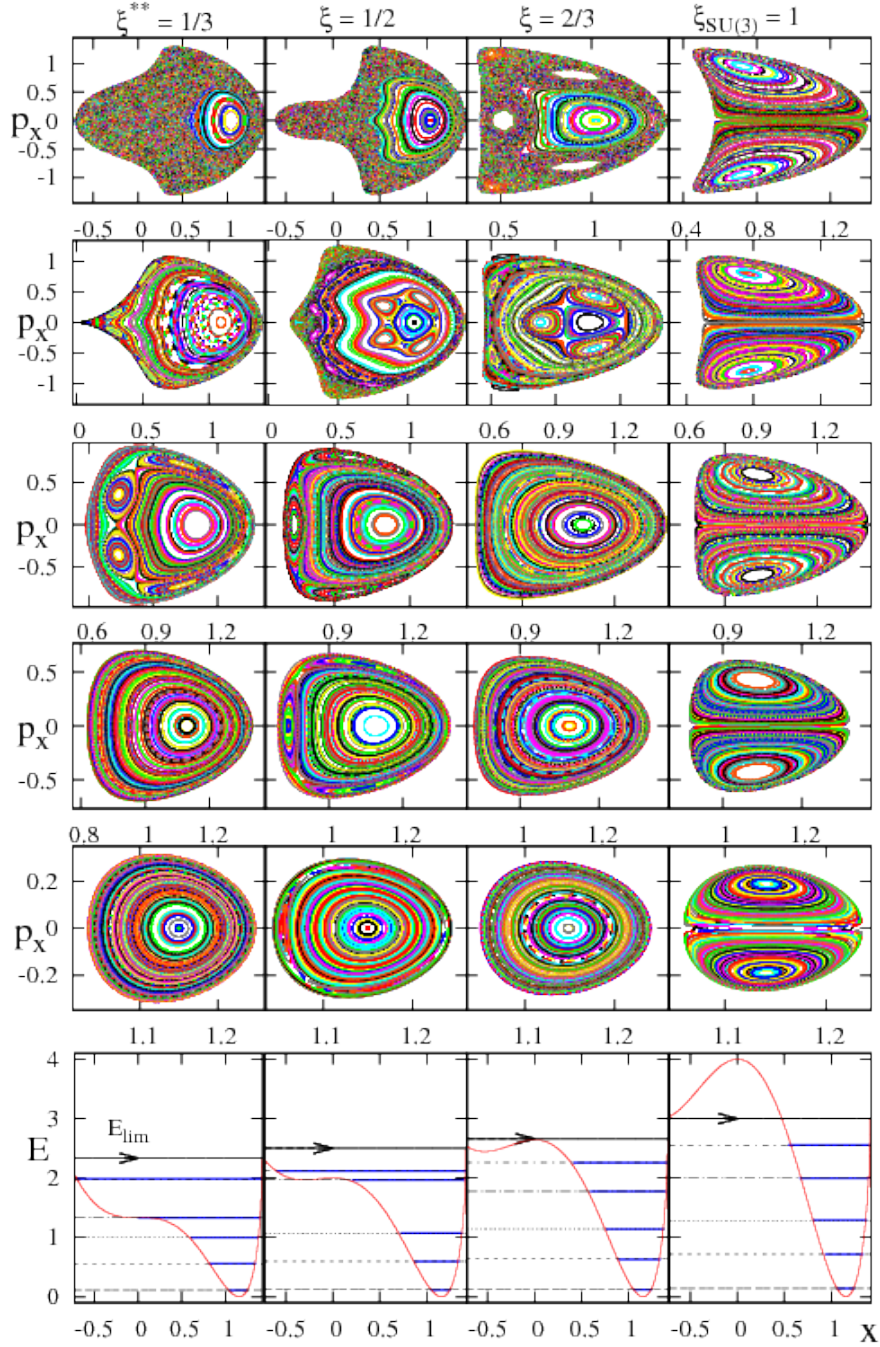


Figure 11: Poincaré sections in the stable deformed phase (region III) The panels are as in Fig. 9, but for the classical intrinsic Hamiltonian  $\mathcal{H}_2(\xi)$  (26b) and potential  $V_2(\xi; x, y = 0)$  (31b), with  $\xi \geq \xi^{**}$  and  $E_{\text{lim}} = h_2(2+\xi)$ . The left column ( $\xi^{**}$ ) corresponds to the anti-spinodal point. The right column ( $\xi_{\text{SU}(3)} = 1$ ) corresponds to the integrable SU(3) DS limit.



is similar to the Hénon-Heiles system (HH) [76] with regularity at low energy and marked onset of chaos at higher energies. The chaotic component of the dynamics increases with  $\rho$  and maximizes at the spinodal point  $\rho^* = 0.5$ . The chaotic orbits densely fill two-dimensional regions of the surface of section.

The dynamics changes profoundly in the coexistence region (region II). Here the relevant classical Hamiltonians are  $\mathcal{H}_1(\rho)$ , Eq. (26a), with  $\rho^* < \rho \leq \rho_c$  and  $\mathcal{H}_2(\xi)$ , Eq. (26b), with  $\xi_c \leq \xi < \xi^{**}$ . The corresponding potentials  $V_1(\rho)$ , Eq. (31a), and  $V_2(\xi)$ , Eq. (31b) have both spherical and deformed minima, which become degenerate and cross at the critical point ( $\rho_c = 1/\sqrt{2}, \xi_c = 0$ ). The Poincaré sections before, at and after the critical point, ( $\rho = 0.6, \xi_c = 0, \xi = 0.1$ ) are shown in Fig. 10. In general, the motion is predominantly regular at low energies and gradually turning chaotic as the energy increases. However, the classical dynamics evolves differently in the vicinity of the two wells. As the local deformed minimum develops, robustly regular dynamics attached to it appears. The trajectories form a single island and remain regular even at energies far exceeding the barrier height  $V_{\text{bar}}$ . This behavior is in marked contrast to the HH-type of dynamics in the vicinity of the spherical minimum, where a change with energy from regularity to chaos is observed, until complete chaoticity is reached near the barrier top. The clear separation between regular and chaotic dynamics, associated with the two minima, persists all the way to the barrier energy,  $E = V_{\text{bar}}$ , where the two regions just touch. At  $E > V_{\text{bar}}$ , the chaotic trajectories from the spherical region can penetrate into the deformed region and a layer of chaos develops, and gradually dominates the surviving regular island for  $E \gg V_{\text{bar}}$ . As  $\xi$  increases, the spherical minimum becomes shallower, and the HH-like dynamics diminishes.

As seen in Fig. 11, the dynamics is robustly regular in the stable deformed phase (region III), where the relevant classical Hamiltonian is  $\mathcal{H}_2(\xi)$ , Eq. (26b), with  $\xi \geq \xi^{**}$ . The spherical minimum disappears at the anti-spinodal point  $\xi^{**} = 1/3$  and the relevant potential  $V_2(\xi)$ , Eq. (31b), remains with a single deformed minimum. Regular motion prevails for  $\xi \geq \xi^{**}$  where a single stable fixed point, surrounded by a family of elliptic orbits, continues to dominate the Poincaré section. In certain regions of the control parameter  $\xi$  and energy, the section landscape changes from a single to several regular islands, reflecting the sensitivity of the dynamics to local degeneracies of normal modes. Such resonance effects will be elaborated in more detail in Section 5.3. A notable exception to such variation is the SU(3) DS limit ( $\xi = 1$ ), for which the system is integrable and the phase space portrait is the same for any energy.

### 5.3. Resonance effects

The preceding discussion has shown that even away from the integrable SU(3) limit, the classical intrinsic dynamics associated with the deformed well, remains robustly regular. In most segments of regions II and III, the Poincaré sections exhibit a single island, originating from simple  $\beta$  ( $x$ ) and  $\gamma$  ( $y$ ) orbits, imprinting the small amplitude vibrations of normal modes about the deformed minimum. As noted, occasionally, resonances in these oscillations give rise to additional chains of regular islands. In the present section we examine in more detail this sensitivity of the classical motion and attempt to demarcate the ranges of energy and control parameters where these resonance effects occur.

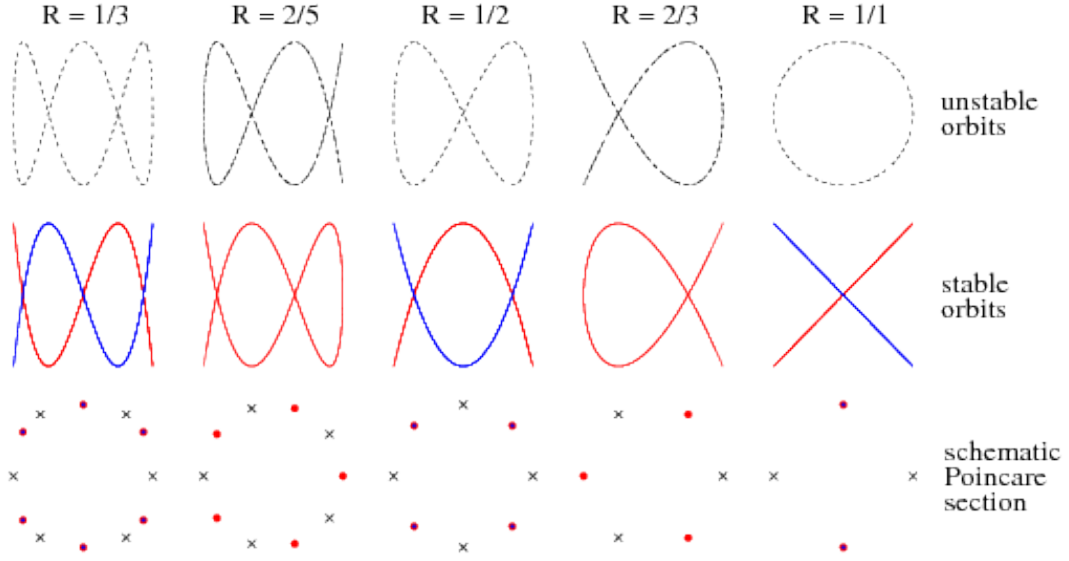


Figure 12: Lissajous figures of the simplest stable (middle row) and unstable (top row) resonant orbits of  $\mathcal{H}_2(\xi)$ , Eq. (26b), with  $\beta_0 = \sqrt{2}$ . The bottom row illustrates the Poincaré-Birkhoff scenario of the breakdown of resonant tori. Sequences of alternating stable (dots) and unstable (crosses) fixed points are seen in the Poincaré sections due to the stable and unstable orbits for each particular resonance.

The dynamical consequences of perturbing a classical integrable system, are governed by the celebrated Kolmogorov-Arnold-Moser (KAM) and Poincaré-Birkhoff (PB) theorems [9, 10, 11]. According to the KAM theorem, most tori of the integrable system which are sufficiently irrational, get slightly deformed in the perturbed system but are not destroyed. On the other hand, the resonant tori (the tori characterized by a rational ratio of winding frequencies) of the integrable system, disintegrate when the system gets perturbed and consequently, according to the PB theorem, a chain of islands is formed on the surface of section. The resonant tori decay into sets of stable and unstable orbits, giving rise to sequences of alternating elliptic and hyperbolic fixed points. The elliptic points lead to the emergence of regular islands, inside which the trajectories are phase-locked and the ratio of the corresponding frequencies remains equal to the rational number of the corresponding initial resonant torus. The hyperbolic points lie on separatrix intersections between the islands, about which chaotic layers can develop.

For the considered classical intrinsic Hamiltonian  $\mathcal{H}_2(\xi)$ , Eq. (26b), in the deformed region ( $\xi \geq \xi_c = 0$ ), the resonances are reached when the ratio  $R = \epsilon_\beta/\epsilon_\gamma = m/n$  of Eq. (59), is a rational number. The shape of the resonant orbits resembles Lissajous figures with the same ratio of frequencies. For more details on the topology of such orbits, the reader is referred to [77]. The most pronounced resonances (thicker PB islands) correspond to small co-prime  $(m, n)$  integers, and the number of islands in a given chain is  $2/R$ . These features were observed in Fig. 6, and are shown schematically in Fig. 12, for  $R = 1, 2/3, 1/2, 2/5, 1/3$ , corresponding to 2, 3, 4, 5, 6 islands, respectively.

At low energy ( $E \rightarrow 0$ ), where the harmonic approximation is valid, one expects the

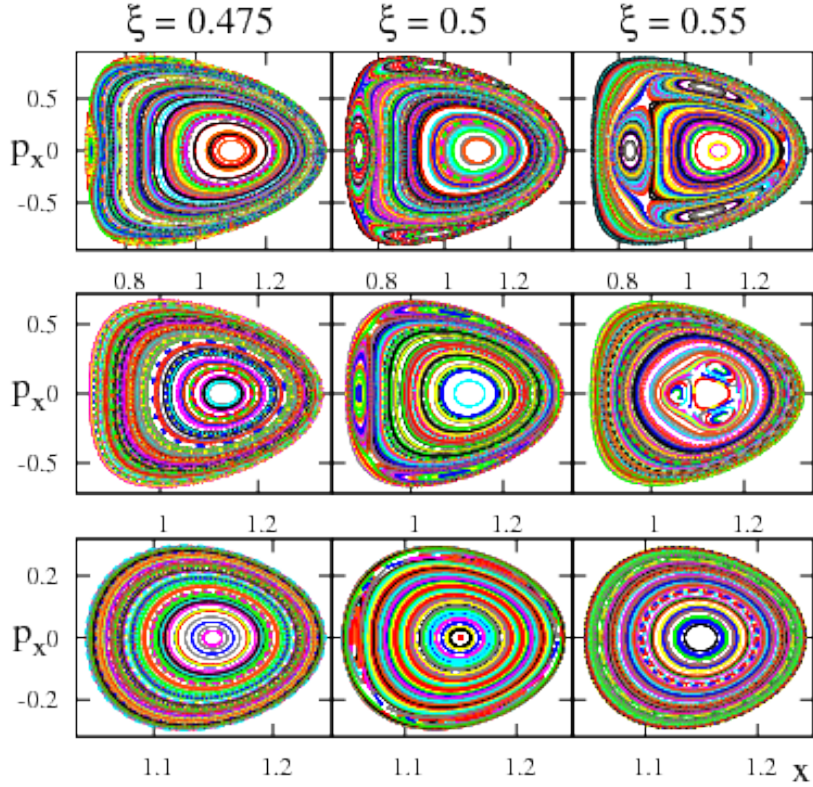


Figure 13: Poincaré sections near the  $R = 2/3$  normal-mode resonance. The three columns refer to values of  $\xi = 0.475, 0.5, 0.55$ , before, at, and after the resonance point,  $\xi_R = 0.5$ , Eq. (65). The bottom, center and top rows, correspond to energies  $E_1 = V_{\text{lim}}(\xi)/21$ ,  $E_2 = 5V_{\text{lim}}(\xi)/21$ ,  $E_3 = 9V_{\text{lim}}(\xi)/21$ , respectively, below the domain boundary  $V_{\text{lim}}(\xi) = (2 + \xi)h_2$ , Eq. (44).

resonances to occur at discrete values of the control parameter  $\xi \approx \xi_R$ , in a narrow interval around  $\xi_R$ ,

$$\xi_R = \frac{9}{2}(1 + \beta_0^2)^{-1}R - \frac{1}{2}, \quad (65)$$

where the latter is obtained by inverting Eq. (59). At a finite energy ( $E > 0$ ), anharmonic effects in  $\mathcal{H}_2(\xi)$  come into play and, consequently, a PB chain of islands associated with a given rational  $R$  ratio, can occur in wider ranges of  $\xi$  values.

The sensitivity of the classical dynamics to resonance effects is demonstrated in Fig. 13 near  $R = 2/3$ , where the PB chain consists of three regular islands. The different columns show the Poincaré sections for  $\xi = 0.475, 0.5, 0.55$ , at energies  $E_1 = V_{\text{lim}}(\xi)/21$  (bottom row),  $E_2 = 5E_1$  (center row), and  $E_3 = 9E_1$  (upper row), where  $V_{\text{lim}}(\xi) = (2 + \xi)h_2$ , Eq. (44). At the resonance point,  $\xi_R = 0.5$  (middle column), one observes at all chosen energies, the expected three regular islands near the perimeter of the Poincaré sections, indicating an instability with respect to the  $\beta$ -motion. Their relative size compared to the total area of the section, increases with energy. In contrast, the PB islands are not seen at low  $E$  neither

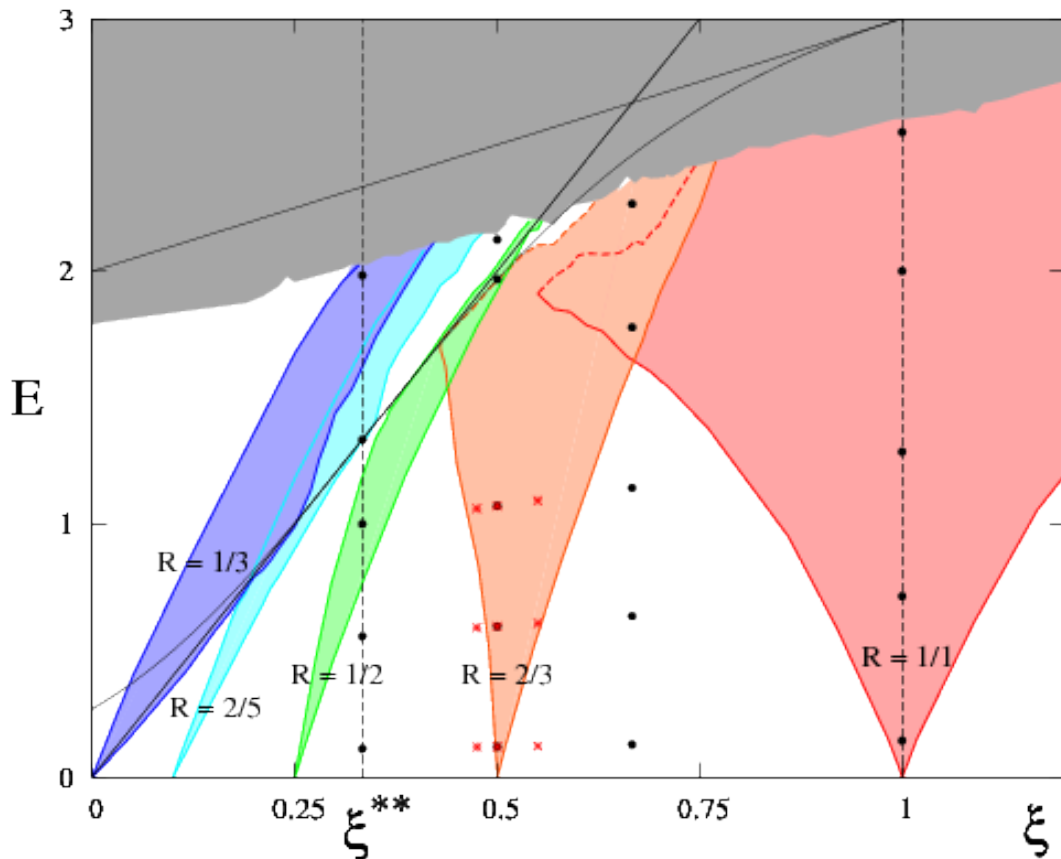


Figure 14: Resonance map for the Hamiltonian  $\mathcal{H}_2(\xi)$  with  $\beta_0 = \sqrt{2}$  and  $h_2 = 1$ , Eq. (26b), on the deformed side of the QPT,  $\xi \geq 0$ . The color-coded regions indicate the occurrence of major Poincaré-Birkhoff chains of islands in the Poincaré sections due to normal-mode resonances with frequency ratios  $R = 1/3, 2/5, 1/2, 2/3$  and  $1/1$ , giving rise to 6, 5, 4, 3, 2 islands, respectively. As  $E \rightarrow 0$ , the colored regions tip exactly towards the resonant values  $\xi_R$  of Eq. (65). White areas involve  $(\xi, E)$  domains with a single island. Black bullets (red stars) correspond to individual panels in Figs. 10-11 (Fig. 13). Stationary and boundary values of the potential surface  $V_2(\xi)$ , Eq. (28b), are marked by thin black lines (compare with Fig. 3). The gray area at high energies is inaccessible due to numerical instability.

at  $\xi = 0.475$  (see panels for  $E = E_1, E_2$ ), nor at  $\xi = 0.55$  (panel for  $E = E_1$ ), where the Poincaré sections display the usual pattern of a single island. These islands, however, do appear at higher energies,  $E = E_3$  for  $\xi = 0.475$  and  $E = E_2$  for  $\xi = 0.55$ . In the latter case, the PB island-chain occurs near the center of the Poincaré section, signaling an instability with respect to the  $\gamma$ -motion.

Fig. 14 presents a detailed map of the (colored-coded) regions in the  $(\xi, E)$  plane, where PB chains with 2, 3, 4, 5, 6 islands occur. The latter are associated with the most pronounced resonances having normal-mode frequency ratios  $R = 1, 2/3, 1/2, 2/5, 1/3$ , respectively. For  $E \rightarrow 0$ , all the resonance regions end in a sharp tip at  $\xi_R = 0, 0.1, 0.25, 0.5, 1$ , in agreement with Eq. (65). As the energy  $E > 0$  increases, the resonance regions are either tilted away from  $\xi_R$  (as for  $R = 1/3, 2/5, 1/2$ ) or fan out and embrace  $\xi_R$  (as for  $R = 2/3, 1$ ).

At higher energies, pairs of regions  $[(R = 1/3, 2/5), (R = 1/2, 2/3), (R = 2/3, 1)]$ , can overlap, indicating that for a given Hamiltonian  $\mathcal{H}_2(\xi)$ , Eq. (26b), two distinct PB island chains can occur simultaneously in the Poincaré surface. The white areas outside the color-coded resonance regions, identify the  $(\xi, E)$  domains where the Poincaré surfaces exhibit a single island, without additional PB island chains. The dominance of these areas for  $E \leq 1$  explains why this simple pattern prevails in most Poincaré sections at low energies.

Fig. 14 is very instrumental for understanding the rich regular structure arising from the classical intrinsic dynamics in regions II and III of the QPT, for  $\xi \geq 0$ . For orientation, a few black bullets are marked in some of the color-coded resonance regions, corresponding to particular Poincaré sections in Figs. 10-11. For the critical point, the line  $\xi_c = 0$  is completely inside a white area in Fig. 14 and no resonance regions are seen along it, consistent with the single island observed in the panels of the  $\xi_c = 0$  column in Fig. 10. At the anti-spinodal point ( $\xi^{**} = 1/3$ ), the lowest two bullets marked in Fig. 14, are located in white areas and the remaining bullets at higher energies reside inside the  $R = 1/2, 2/5, 1/3$  resonance regions, consecutively. This is consistent with the observed surfaces of the  $\xi^{**} = 1/3$  column in Fig. 11, where the lowest two panels display a single island and the remaining panels in consecutive order, show PB chains with 4, 5, 6 islands. The Poincaré sections of the  $\xi = 2/3$  column in Fig. 11, show a single island (lowest three panels) and a PB chain of three islands in the remaining panels at higher energies. This is again in line with the location of the bullets for  $\xi = 2/3$  in Fig. 14. For the SU(3)-DS limit ( $\xi = 1$ ), the Poincaré sections in Fig. 11 display two islands at all energies, consistent with the sole  $R = 1$  resonance region embracing the  $\xi = 1$  line in Fig. 14.

Near the boundaries of each resonance region, the PB islands are tiny in size. Upon varying  $\xi$  and/or  $E$  towards the center of a given region, the islands migrate to the interior of the main regular island in the respective Poincaré sections, and grow in relative size. Such a scenario is seen clearly in the panels of Fig. 13. The latter correspond to the red starred points near/inside the  $R = 2/3$  resonance region in Fig. 14. The dashed lines marking the high- $E$  boundaries of the  $R = 2/3$  and  $R = 1$  resonance regions, indicate the location where the respective PB chains disappear in the surrounding chaotic sea. Thus, for  $\xi = 0.5$  in Fig. 14, the fourth black bullet lies on the dashed line marking the boundary of the  $R = 2/3$  resonance region, where the three islands of the PB chain just disappear in an emerging chaotic layer. Notice, that the same black bullet lies simultaneously inside the  $R = 1/2$  resonance region and indeed, we observe four additional pronounced islands in the fourth panel from the bottom of the  $\xi = 0.5$  column in Fig. 11. In contrast, the fifth black bullet at higher energy for  $\xi = 0.5$ , lies inside a white area in Fig. 14 and in the corresponding fifth panel in Fig. 11, we observe just a single regular island, without any PB island chains, embedded in a significant chaotic environment.

## 6. Quantum analysis

The analysis of the classical dynamics, constraint to  $L = 0$ , has revealed a rich inhomogeneous phase space structure with a pattern of mixed regular and chaotic dynamics, reflecting the changing topology of the Landau potential across the QPT. It is clearly of in-

terest to examine the implications of this behavior to the quantum treatment of the system. In what follows, we consider the evolution of levels in the corresponding quantum spectrum and examine the regular and irregular features of these quantum states.

### 6.1. Level evolution

Fig. 15 shows the correlation diagrams for energies of ( $N = 80, L = 0$ ) eigenstates of the intrinsic Hamiltonian, Eq. (7), with  $\beta_0 = \sqrt{2}$ , as a function of the control parameters,  $0 \leq \rho \leq \rho_c$  (upper portion) and  $\xi_c \leq \xi \leq 1$  (lower portion). The position of the spinodal point ( $\rho^* = 1/2$ ) and the anti-spinodal point ( $\xi^{**} = 1/3$ ), is indicated by vertical lines. In-between these points, inside the coexistence region, solid lines mark the energies of the barrier ( $V_{\text{bar}}$ ) at the saddle point and of the local minima ( $V_{\text{def}}$  for  $\rho^* < \rho \leq \rho_c$  and  $V_{\text{sph}}$  for  $\xi_c \leq \xi < \xi^{**}$ ) in the relevant Landau potential (compare with Fig. 3).

On the spherical side of the QPT, outside of the coexistence region ( $0 \leq \rho \leq \rho^*$ ), the spectrum of  $\hat{H}_1(\rho)$  (7a) at low energy, resembles the normal-mode expression of Eq. (9),  $E = \epsilon n_d$  ( $n_d = 0, 2, 3, \dots$ ), with  $\epsilon = 4\bar{h}_2 N$  independent of  $\rho$  (the missing  $n_d = 1$  state has  $L = 2$ ). As seen in the upper portion of Fig. 15, this low-energy behavior is observed also inside the coexistence region ( $\rho^* < \rho \leq \rho_c$ ) at energies  $E < V_{\text{def}}$  below the local deformed minimum. Anharmonicities are suppressed by  $1/N$ , as can be verified by comparing the spectrum at  $\rho = 0$  with the U(5)-DS expression, Eq. (17). At higher energies and  $\rho > 0$ , there are noticeable level repulsion and (avoided) level crossing occurring in the classical chaotic regime. These effects become more pronounced as  $\rho$  increases and approaches the spinodal point  $\rho^*$ , and are due to the U(5) breaking  $\rho$ -term in Eq. (19).

On the deformed side of the QPT, outside of the coexistence region ( $\xi^{**} \leq \xi \leq 1$ ), the levels with  $L = 0$  serve as bandheads of rotational  $K = 0$  bands, associated with the ground band  $g(K = 0)$  and multiple  $\beta^n \gamma^{2k}$  ( $K = 0$ ) excitations of the prolate-deformed shape. The low energy spectrum of  $\hat{H}_2(\rho)$  (7b) resembles the normal-mode expression of Eq. (10),  $E = \epsilon_\beta n_\beta + \epsilon_\gamma n_\gamma$  ( $n_\beta = 0, 1, 2, \dots$  and  $n_\gamma = 0, 2, 4, 6, \dots$ ) with  $\epsilon_\beta = 4\bar{h}_2 N(2\xi + 1)$  and  $\epsilon_\gamma = 12\bar{h}_2 N$  (only bands with  $n_\gamma$  even support  $L = 0$  states). In particular, bandhead energies involving pure  $\gamma$  excitations are independent of  $\xi$ , while bandhead energies involving  $\beta$  excitations are linear in  $\xi$ , a trend seen in the lower portion of Fig. 15. Local degeneracies of normal-modes lead to bunching of energy levels and noticeable voids in the level density, in the same regions of  $(\xi, E)$  shown in the classical resonance map of Fig. 14. For  $\xi = 1$ , one has  $\epsilon_\beta = \epsilon_\gamma$  and the spectrum follows the SU(3)-DS expression, Eq. (22), with anharmonicities of order  $1/N$ . This ordered pattern of levels is observed also inside the coexistence region ( $\xi_c \leq \xi < \xi^{**}$ ) at energies  $E < V_{\text{sph}}$  below the local spherical minimum.

Dramatic structural changes in the level dynamics take place in the coexistence region ( $\rho^* < \rho \leq \rho_c$ ) and ( $\xi_c \leq \xi < \xi^{**}$ ). As shown in Fig. 15, at energies above the respective local minima, ( $E > V_{\text{sph}}$  or  $E > V_{\text{def}}$ ), the spherical type and deformed type of levels approach each other and their encounter results in marked modifications in the local level density. In particular, there is an accumulation of levels near the top of the barrier ( $V_{\text{bar}}$ ). Such singularities in the evolution of the spectrum, referred to as excited state quantum phase transition [42], have been encountered in integrable models involving QPTs [78]. In what follows, we plan to examine the regular and irregular features of these quantum states, and

explore how their properties echo the mixed regular and chaotic dynamics observed in the classical analysis of the first-order QPT.

## 6.2. Peres lattices

Quantum manifestations of classical chaos are often detected by statistical analyses of energy spectra [9, 10, 11]. In a quantum system with mixed regular and irregular states, the statistical properties of the spectrum are usually intermediate between the Poisson and the Gaussian orthogonal ensemble (GOE) statistics. Such global measures of quantum chaos are, however, insufficient to reflect the rich dynamics of an inhomogeneous phase space structure encountered in Fig. 9-11, with mixed but well-separated regular and chaotic regions. To do so, one needs to distinguish between regular and irregular subsets of eigenstates in the same energy intervals. For that purpose, we employ the spectral lattice method of Peres [79], which provides additional properties of individual energy eigenstates. The Peres lattices are constructed by plotting the expectation values  $O_i = \langle i|\hat{O}|i\rangle$  of an arbitrary operator,  $[\hat{O}, \hat{H}] \neq 0$ , versus the energy  $E_i = \langle i|\hat{H}|i\rangle$  of the Hamiltonian eigenstates  $|i\rangle$ . The lattices  $\{O_i, E_i\}$  corresponding to regular dynamics can be shown to display a regular pattern, while chaotic dynamics leads to disordered meshes of points. The method has been recently applied to the collective model of nuclei [74, 75] and to the IBM [80, 81]. The ability of the method to distinguish between regular and irregular states, does not rely on the Peres operators  $\hat{O}$  used, and their choice can be made on physical grounds.

In the present analysis, in order to highlight the classical-quantum correspondence, we choose  $\hat{O} = \hat{n}_d$  and define the Peres lattices as the set of points  $\{x_i, E_i\}$ , with

$$x_i \equiv \sqrt{\frac{2\langle i|\hat{n}_d|i\rangle}{N}}, \quad (66)$$

and  $|i\rangle$  being the eigenstates of the IBM Hamiltonian. The expectation value of  $\hat{n}_d$  in the condensate  $|\beta; N\rangle \equiv |\beta, \gamma = 0; N\rangle$  of Eq. (3)

$$x = \beta = \sqrt{\frac{2\langle \beta; N|\hat{n}_d|\beta; N\rangle}{N}}, \quad (67)$$

is related to the deformation  $\beta$  (whose equilibrium value is the order parameter of the QPT) and the coordinate  $x$  in the classical potential,  $V(x, y=0) = V(\beta, \gamma=0)$ , Eqs. (28) and (31). The spherical ground state is the  $s$ -boson condensate which has  $n_d = x_i = 0$ . Excited spherical states are obtained, to a good approximation, by replacing  $s$ -bosons in  $|\beta = 0; N\rangle$  with  $d$ -bosons, hence  $x_i \sim \sqrt{n_d/N}$  is small for  $n_d/N \ll 1$ . Rotational members of the deformed ground band are obtained by  $L$ -projection from  $|\beta; N\rangle$  and have  $x_i \approx \beta$  to leading order in  $N$ . This relation is still valid, to a good approximation, for states in excited deformed bands, whose intrinsic states are obtained by replacing condensate bosons in  $|\beta; N\rangle$  with the orthogonal bosons,  $\Gamma_\beta^\dagger = [\sqrt{2 - \beta^2}d_0^\dagger - \beta s^\dagger]/\sqrt{2}$  and  $\Gamma_{\gamma, \pm 2}^\dagger = d_{\pm 2}^\dagger$ , representing  $\beta$  and  $\gamma$  excitations [53, 82]. These attributes have the virtue that the chosen lattices  $\{x_i, E_i\}$  of Eq. (66), can identify the regular/irregular quantum states and associate them with a given region in the classical phase space.



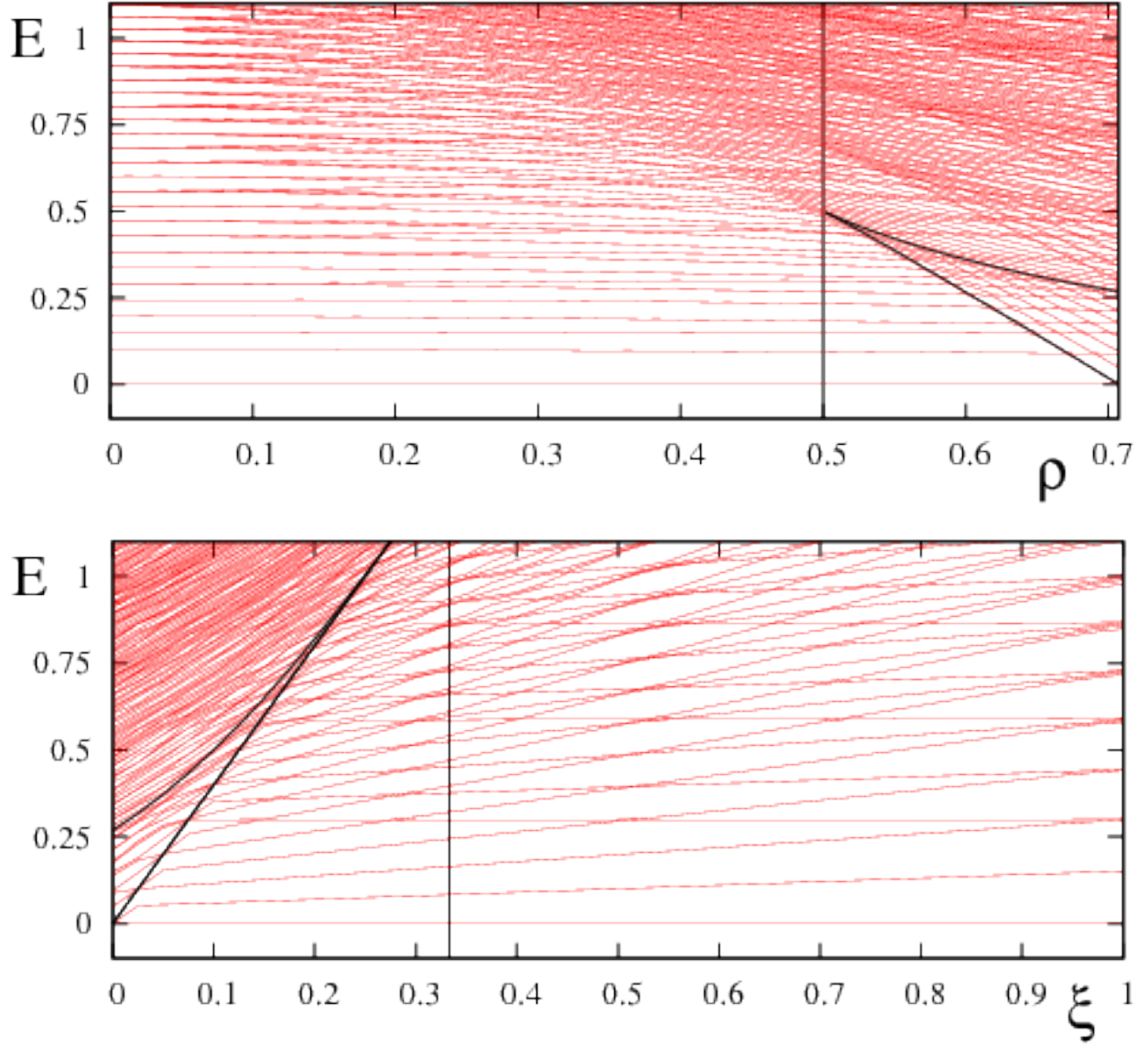


Figure 15: The evolution of  $L = 0$  energy levels for the intrinsic Hamiltonian, Eq. (7), with  $\beta_0 = \sqrt{2}$ ,  $h_2 = 1$  and  $N = 80$ . Upper portion: the  $L = 0$  spectrum of  $\hat{H}_1(\rho)$ , Eq. (7a), relevant to the spherical side of the QPT ( $0 \leq \rho \leq \rho_c$ ). Here  $\rho = 0$  corresponds to the U(5)-DS limit,  $\rho^* = 0.5$  is the spinodal point (marked by a vertical line) and  $\rho_c = 1/\sqrt{2}$  is the critical point. The energies of the barrier ( $V_{\text{bar}}$ ) at the saddle point and of the local deformed minimum ( $V_{\text{def}}$ ) are marked by solid lines inside the coexistence region ( $\rho^* < \rho \leq \rho_c$ ). Note that in this portion, the lowest  $L = 0$  level is the solvable U(5) state with  $n_d = 0$ , Eq. (20a). Lower portion: the  $L = 0$  spectrum of  $\hat{H}_2(\xi)$ , Eq. (7b), relevant to the deformed side of the QPT ( $\xi_c \leq \xi \leq 1$ ). Here  $\xi_c = 0$  is the critical point,  $\xi^{**} = 1/3$  is the anti-spinodal point (marked by a vertical line) and  $\xi = 1$  correspond to the SU(3)-DS limit. The energies of the barrier ( $V_{\text{bar}}$ ) at the saddle point and of the local spherical minimum ( $V_{\text{sph}}$ ) are marked by solid lines inside the coexistence region ( $\xi_c \leq \xi \leq \xi^{**}$ ). Note that in this portion, the lowest  $L = 0$  level is the solvable SU(3) state of Eq. (25a).



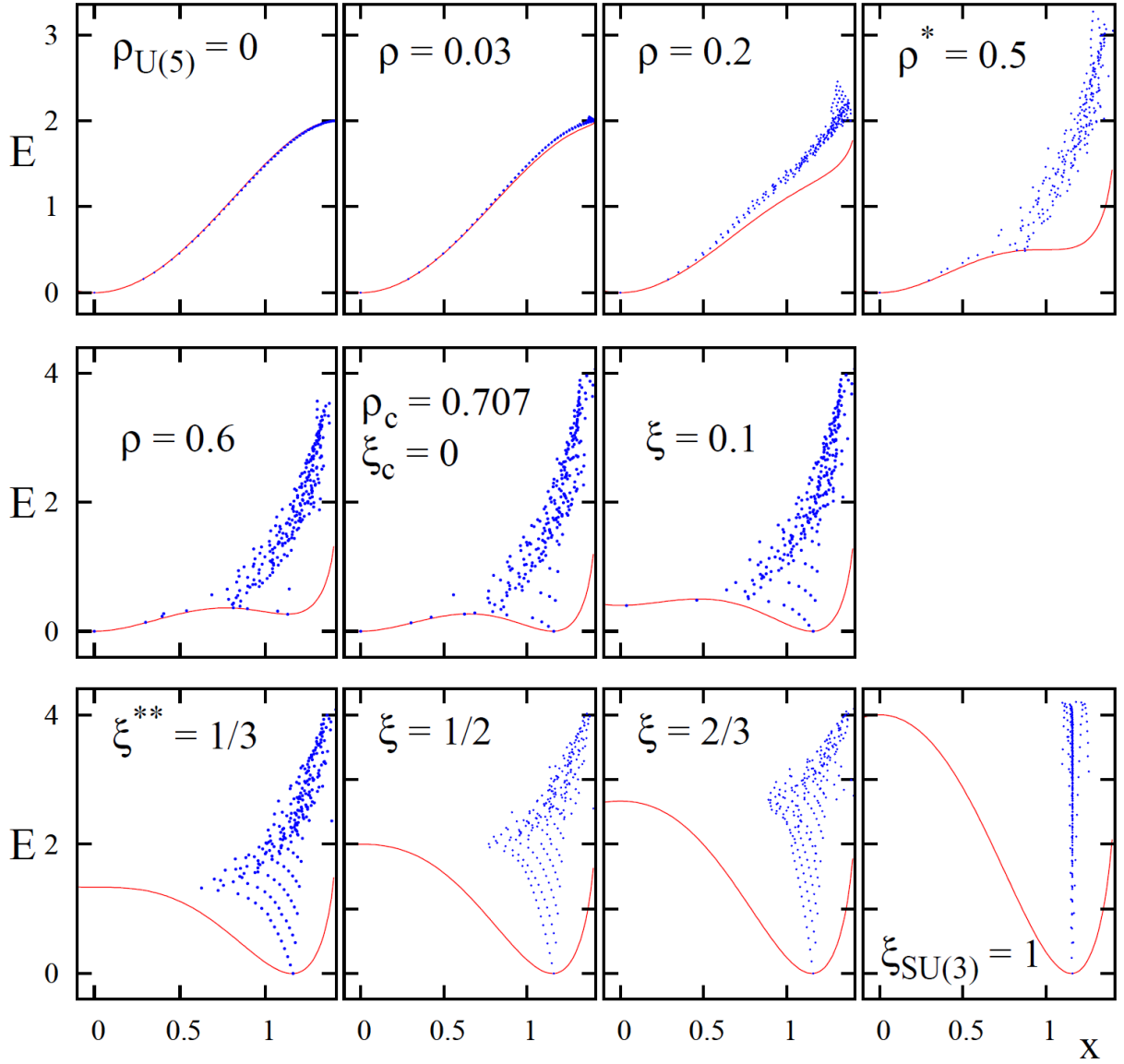


Figure 16: Peres lattices  $\{x_i, E_i\}$ , Eq. (66), of  $(N = 50, L = 0)$  eigenstates of the intrinsic Hamiltonian, Eq. (7), with  $h_2 = 1$ ,  $\beta_0 = \sqrt{2}$ , for several values of the control parameters in region I (top row), region II (center row) and region III (bottom row). The lattices are overlaid on the classical potentials  $V(x, y = 0)$ , Eq. (31).

### 6.3. Evolution of the quantum dynamics across the QPT

The Peres lattices for  $(N = 50, L = 0)$  eigenstates of the intrinsic Hamiltonian (7) with  $\beta_0 = \sqrt{2}$  and  $h_2 = 1$ , are shown in Fig. 16, portraying the quantum dynamics across the QPT in regions I-II-III. To facilitate the comparison of the quantum and classical analyses, the Peres lattices  $\{x_i, E_i\}$  of Eq. (66) are overlaid on the classical potentials  $V(x, y = 0)$  of Eq. (31). These are the same potentials shown at the bottom rows in Figs. 9-10-11, depicting the classical dynamics in these regions.

The top row of Fig. 16 displays the evolution of quantum Peres lattices in the stable spherical phase (region I) for the same values of the control parameter  $\rho \in [0, \rho^*]$  in  $\hat{H}_1(\rho)$ , Eq. (7a), as in the classical Poincaré sections of Fig. 9. For  $\rho = 0$ , the Hamiltonian (16) has  $U(5)$  DS with a solvable spectrum  $E_i = 2\hbar_2[2N - 1 - n_d]n_d$ , Eq. (17). For large  $N$ , and

replacing  $x_i$  by  $\beta$ , the Peres lattice coincides with  $V_1(\rho = 0)$ , Eq. (38), a trend seen for  $\rho = 0$  (full regularity) and  $\rho = 0.03$  (almost full regularity) in the top row of Fig. 16. For  $\rho = 0.2$ , at low energy a few lattice points still follow the potential curve  $V_1(\rho)$ , but at higher energies one observes sizeable deviations and disordered meshes of lattice points, in accord with the onset of chaos in the classical Hénon-Heiles system considered in Fig. 9. The disorder in the Peres lattice enhances at the spinodal point  $\rho^* = 0.5$ , where the chaotic component of the classical dynamics maximizes.

The center row of Fig. 16 displays the evolution of quantum Peres lattices in the region of phase-coexistence (region II) for  $\rho \in (\rho^*, \rho_c]$  in  $\hat{H}_1(\rho)$ , Eq. (7a), and  $\xi \in [\xi_c, \xi^{**})$  in  $\hat{H}_2(\xi)$ , Eq. (7b). The calculations shown are for the same values of control parameters used in the classical analysis in Fig 10. The occurrence of a second deformed minimum in the potential is signaled by the occurrence of regular sequences of states localized within and above the deformed well. They form several chains of lattice points close in energy, with the lowest chain originating at the deformed ground state. A close inspection reveals that the  $x_i$ -values of these regular states, lie in the intervals of  $x$ -values occupied by the regular tori in the Poincaré sections in Fig. 10. Similarly to the classical tori, these regular sequences persist to energies well above the barrier  $V_{\text{bar}}$ . The lowest sequence consists of  $L=0$  bandhead states of the ground  $g(K=0)$  and  $\beta^n(K=0)$  bands. Regular sequences at higher energy correspond to multi-phonon  $\beta^n\gamma^{2m}(K=0)$  bands. In contrast, the remaining states, including those residing in the spherical minimum, do not show any obvious patterns and lead to disordered (chaotic) meshes of points at high energy  $E > V_{\text{bar}}$ .

The bottom row of Fig. 16 displays the Peres lattices in the stable deformed phase (region III) for  $\xi \in [\xi_c, 1]$ , and is the quantum counterpart of Fig. 11. No lattice points are seen at small values of  $x < 0.5$ , beyond the anti-spinodal point  $\xi^{**}$ , where the spherical minimum disappears. On the other hand, more and longer regular sequences of  $K=0$  bandhead states are observed in the vicinity of the single deformed minimum ( $x \approx 1$ ) as its depth increases. These sequences tend to be more aligned above the center of the potential well, as  $\xi$  progresses from  $\xi^{**}$  towards the SU(3) limit ( $\xi = 1$ ). A close inspection reveals slight dislocations in the ordered pattern of lattice points for those values of  $(\xi, E)$ , mentioned in Section 5, corresponding to a resonance.

Unlike the Poincaré sections of the classical analysis, the Peres spectral method can be used to visualize also the dynamics of quantum states with non-zero angular momenta. Examples of such Peres lattices of states with  $L = 0, 2, 3, 4$  are shown in Fig. 17 for representative values of the control parameters in region I ( $\rho = 0.2$ ), region II ( $\xi_c = 0$ ) and region III ( $\xi = 0.8$ ). The right column in the figure combines the separate- $L$  lattices and overlays them on the relevant classical potential. For  $\rho = 0.2$ , at low energies typical of the regular Hénon Heiles (HH) regime, one can identify multiplets of states with  $L=0, L=2, L=0, 2, 4$ , similar to the lowest U(5) multiplets of Eq. (18). As will be discussed in Section 7, their wave functions show the dominance of a single  $n_d$  component ( $n_d = 0, 1, 2$ , respectively), characteristic of a spherical vibrator. No such multiplet structure can be detected at higher energy in the chaotic HH regime. Interestingly, a small number of low-energy U(5)-like multiplets persists in the coexistence region, to the left of the barrier towards the spherical minimum, as seen in the Peres lattice for the critical point,  $\xi_c = 0$ , in Fig. 17.

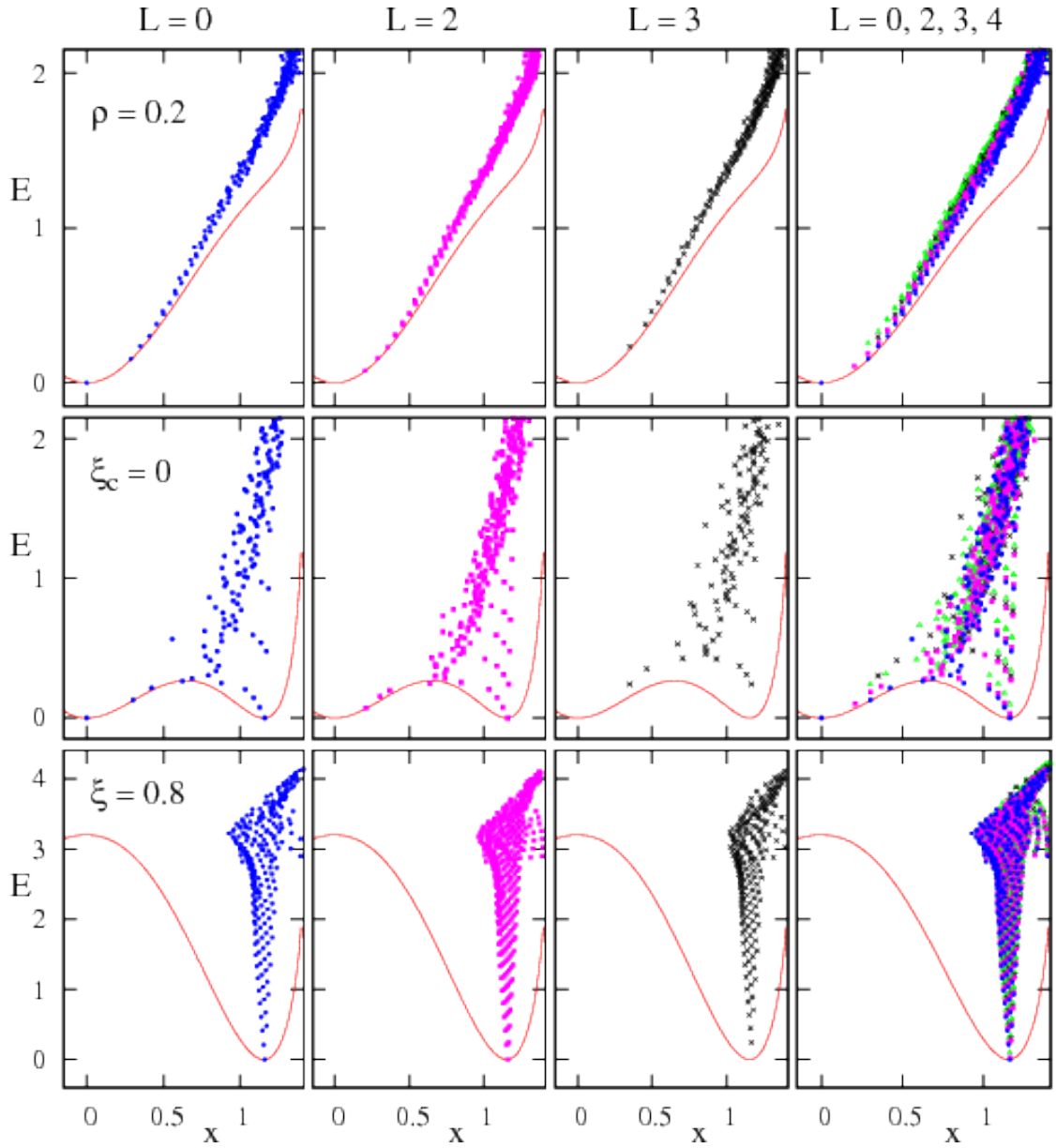


Figure 17: Peres lattices  $\{x_i, E_i\}$ , Eq. (66), for  $L = 0, 2, 3, 4$ , eigenstates of the intrinsic Hamiltonian (7) with  $h_2 = 1$ ,  $\beta_0 = \sqrt{2}$ ,  $N = 50$ . The lattices in region I ( $\rho = 0.2$ ), region II ( $\xi_c = 0$ ) and region III ( $\xi = 0.8$ ) are overlaid on the corresponding classical potential  $V(x, y = 0)$ , Eq. (31). The right column combines the separate- $L$  lattices.

In regions II and III one can detect the rotational states with  $L = 0, 2, 4, \dots$ , comprising the regular  $K=0$  bands mentioned above. Additional  $K$ -bands with  $L = K, K+1, K+2, \dots$ , corresponding to multiple  $\beta$  and  $\gamma$  vibrations about the deformed shape, can also be identified. These ordered band structures show up in the vicinity of the deformed well and are not present in the chaotic portions of the Peres lattice. The panels for  $\xi_c = 0$  in Fig. 17

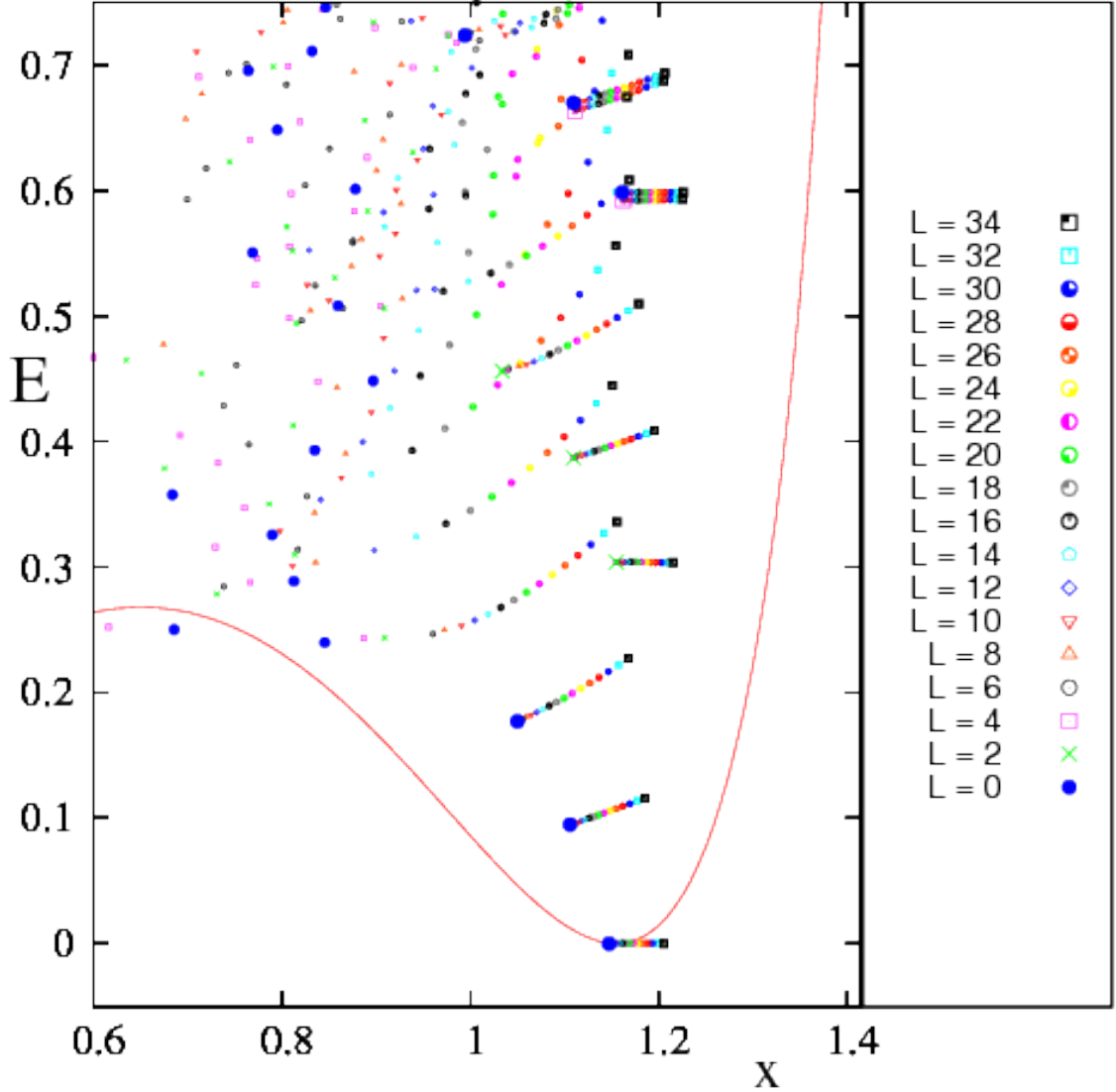


Figure 18: Combined Peres lattices  $\{x_i, E_i\}$ , Eq. (66), for  $L = 0, 2, 4, \dots, 34$ , eigenstates of the intrinsic critical-point Hamiltonian, Eq. (11), with  $h_2 = 1$ ,  $\beta_0 = \sqrt{2}$ ,  $N = 40$ .

demonstrate the occurrence of such regular  $K = 0, 2, 4$  bands inside the coexistence region (region II), alongside with other irregular states represented by the disordered meshes of points in the Peres lattice. The panels for  $\xi = 0.8$  in Fig. 17 indicate that in region III, as the single deformed minimum becomes deeper, the regular  $K$ -bands exhaust larger portions of the Peres lattice. Generally, the states in each regular band share a common intrinsic structure as indicated by their nearly equal values of  $\langle \hat{n}_d \rangle$  and a similar coherent decomposition of their wave functions in the  $SU(3)$  basis, to be discussed in Section 7. The regular bands extend to high angular momenta as demonstrated for the critical point in Fig. 18. While it is natural to find regular rotational bands in a region with a single well-developed

deformed minimum, their occurrence in the coexistence region, including the critical point, is somewhat unexpected, in view of the strong mixing and abrupt structural changes taking place. Their persistence in the spectrum to energies well above the barrier and to high values of angular momenta, amidst a complicated environment, validates the relevance of an adiabatic separation of intrinsic and collective modes [83], for a subset of states.

To conclude, the classical and quantum analyses presented so far, indicate that the variation of the control parameters  $(\rho, \xi)$  in the intrinsic Hamiltonian, induces a change in the topology of the Landau potential across the QPT which, in turn, is correlated with an intricate interplay of order and chaos. For the considered Hamiltonian, whenever a spherical minimum occurs in the potential, the system exhibits an anharmonic oscillator (AO) type of dynamics for small  $\rho$ , and a Hénon Heiles (HH) type of dynamics at larger values of  $\rho$ . While the AO dynamics is regular, the HH dynamics shows a variation with energy from regular to chaotic character, which is reflected in the Peres lattices by a change from ordered to disordered patterns. Whenever a deformed minimum occurs in the potential, the Peres lattices display regular rotational bands localized in the region of the deformed well and corresponding to the regular islands in the classical Poincaré sections. In the coexistence region, these regular bands persist to energies well above the barrier and are well separated from the remaining states, which form disordered meshes of lattice points in the classical chaotic regime. The system in the domain of phase coexistence, thus provides a clear cut demonstration of the classical-quantum correspondence of regular and chaotic behavior, illustrating Percival's conjecture concerning the distinct properties of regular and irregular quantum spectra [84].

## 7. Symmetry aspects

The intrinsic Hamiltonian, Eq. (7), with  $\beta_0 = \sqrt{2}$ , interpolates between the U(5)-DS limit ( $\rho = 0$ ) and the SU(3)-DS limit ( $\xi = 1$ ). Away from these limits, ( $\rho > 0$  and  $\xi < 1$ ), both dynamical symmetries are broken and the competition between terms in the Hamiltonian with different symmetry character, drives the system through a first-order QPT. It is of great interest to study the symmetry properties of the Hamiltonian eigenstates and explore how they echo the observed interplay of order and chaos accompanying the QPT.

The preceding quantum analysis has revealed regular SU(3)-like sequences of states which persist in the deformed region and, possibly, U(5)-like multiples which persist at low-energy in the spherical region. It is natural to seek a symmetry-based explanation for the survival of such regular subsets of states, in the presence of more complicate type of states. In what follows, we show that partial dynamical symmetry (PDS) and quasi-dynamical symmetry (QDS) can play a clarifying role. They reflect, respectively, the enhanced purity and coherence, observed in the wave functions of these selected states.

A number of works [85, 86] have shown that PDSs can cause suppression of chaos even when the fraction of states which has the symmetry vanishes in the classical limit. SU(3) QDS has been proposed [87] to underly the ‘‘arc of regularity’’ [46], a narrow zone of enhanced regularity in the parameter-space of the IBM Hamiltonian, Eq. (13). In conjunction with first-order QPTs, both U(5) and SU(3) PDSs were shown to occur at the critical point [33].

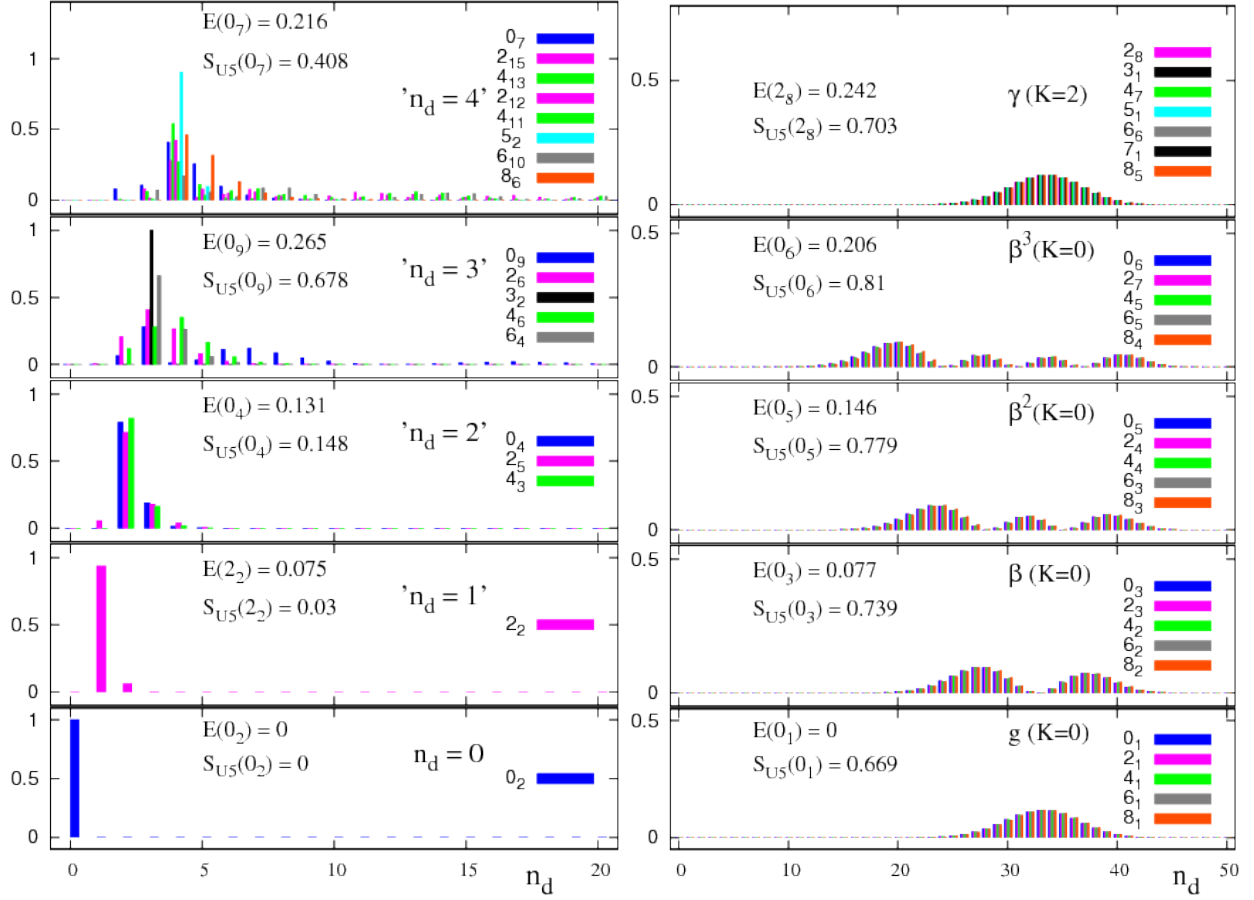


Figure 19: U(5) ( $n_d$ ) decomposition for selected eigenstates of the intrinsic critical-point Hamiltonian, Eq. (11), with  $h_2 = 1$ ,  $\beta_0 = \sqrt{2}$ ,  $N = 50$ . Left column:  $n_d$ -probability distribution  $P_{n_d}^{(L_i)}$ , Eq. (69a), for spherical-type of states arranged in U(5)-like multiplets, ' $n_d$ ', with a maximal  $n_d = 0, 1, 2, 3, 4$  component. Note the dominance of a single  $n_d$ -component for states in the multiplets with ' $n_d \leq 2$ '. Right column:  $P_{n_d}^{(L_i)}$  for deformed-type of states, members of rotational  $K$ -bands, showing a broad  $n_d$ -distribution. Each panel lists the energy and U(5) Shannon entropy  $S_{U5}(L_i)$ , Eq. (70a), of a representative state in the multiplet.

The QDS notion was originally applied to properties of selected low-lying states outside the coexistence region [32]. Later works [80, 81] have demonstrated the relevance of SU(3) QDS not only to the ground band, but also to high-lying bands in the stable deformed phase, with a single deformed minimum. In what follows, we show that the PDS and QDS notions can be used also inside the coexistence region of the QPT and serve as fingerprints for structural changes throughout this region. Their measures can uncover the survival of order in the face of a chaotic environment.

### 7.1. Decomposition of wave functions in the dynamical symmetry bases

Consider an eigenfunction of the IBM Hamiltonian,  $|L_i\rangle$ , with angular momentum  $L$  and ordinal number  $i$  (enumerating the occurrences of states with the same  $L$ , with increasing

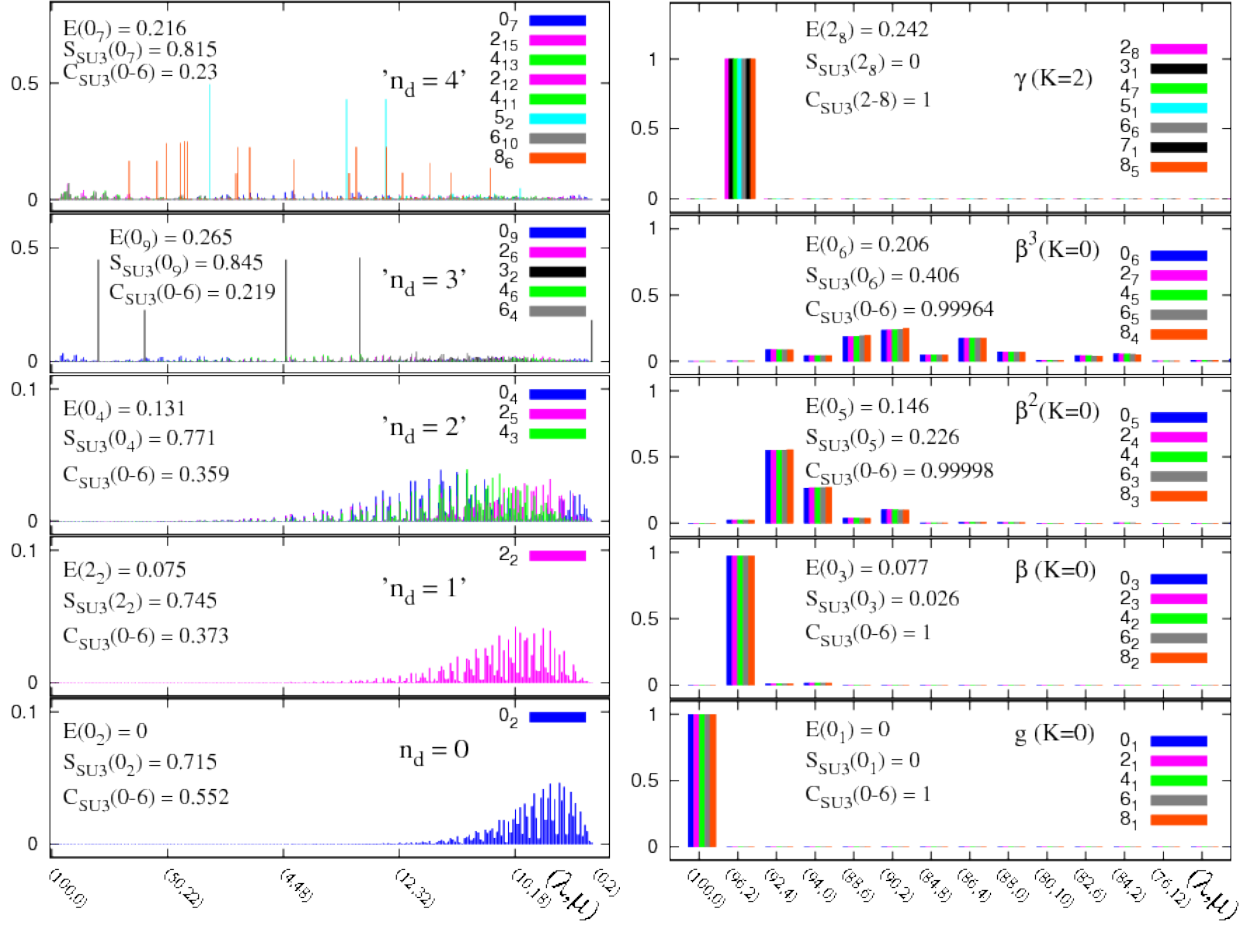


Figure 20: SU(3)  $[(\lambda, \mu)]$  decomposition for the same eigenstates of the intrinsic critical-point Hamiltonian as in Fig. 19. Left column:  $(\lambda, \mu)$ -probability distribution  $P_{(\lambda, \mu)}^{(L_i)}$ , Eq. (69b), for spherical-type of states arranged in ' $n_d$ ' multiplets. Right column:  $P_{(\lambda, \mu)}^{(L_i)}$ , for deformed-type of states arranged in rotational bands. Note the coherent ( $L$ -independent) mixing for states in the same band. Each panel lists the energy, SU(3) Shannon entropy  $S_{\text{SU3}}(L_i)$ , Eq. (70b) and SU(3) correlator  $C_{\text{SU3}(0-6)}$ , Eq. (71), for representative states in the multiplet.

energy). Its expansion in the U(5) DS basis,  $|N, n_d, \tau, n_\Delta, L\rangle$ , of Eq. (1a) and in the SU(3) DS basis,  $|N, (\lambda, \mu), K, L\rangle$ , of Eq. (1b) reads

$$\begin{aligned}
 |L_i\rangle &= \sum_{n_d, \tau, n_\Delta} C_{n_d, \tau, n_\Delta}^{(L_i)} |N, n_d, \tau, n_\Delta, L_i\rangle, \\
 &= \sum_{(\lambda, \mu), K} C_{(\lambda, \mu), K}^{(L_i)} |N, (\lambda, \mu), K, L_i\rangle,
 \end{aligned} \tag{68}$$

where, for simplicity, the dependence of  $|L_i\rangle$  and the expansion coefficients on  $N$  is suppressed. The U(5) ( $n_d$ ) probability distribution,  $P_{n_d}^{(L_i)}$ , and the SU(3)  $[(\lambda, \mu)]$  probability

distribution,  $P_{(\lambda,\mu)}^{(L_i)}$ , are calculated as

$$P_{n_d}^{(L_i)} = \sum_{\tau, n_\Delta} |C_{n_d, \tau, n_\Delta}^{(L_i)}|^2, \quad (69a)$$

$$P_{(\lambda,\mu)}^{(L_i)} = \sum_K |C_{(\lambda,\mu), K}^{(L_i)}|^2. \quad (69b)$$

The sum in Eq. (69a) runs over the  $O(5)$  labels  $(\tau, n_\Delta)$  compatible with the  $U(5) \supset O(5) \supset O(3)$  reduction and the sum in Eq. (69b) runs over the multiplicity label  $K$ , compatible with the  $SU(3) \supset O(3)$  reduction.

The quantity  $P_{n_d}^{(L_i)}$  (69a) provides considerable insight on the nature of states. This follows from the observation that ‘‘spherical’’ type of states show a narrow distribution, with a characteristic dominance of single  $n_d$  components that one would expect for a spherical vibrator. In contrast, ‘‘deformed’’ type of states show a broad  $n_d$ -distribution typical of a deformed rotor structure. This ability to distinguish different types of states, is illustrated for eigenstates of the critical-point Hamiltonian in Fig 19.

The states shown on the left column of Fig. 19, were selected on the basis of having the largest components with  $n_d = 0, 1, 2, 3, 4$ , within the given  $L$  spectra. States with different  $L$  values are arranged into panels labeled by ‘ $n_d$ ’ to conform with the structure of the  $n_d$ -multiplets of the  $U(5)$  DS limit, Eq. (18). Each panel depicts the  $n_d$ -probability,  $P_{n_d}^{(L_i)}$ , for states in the multiplet and lists the energy of a representative eigenstate. In particular, the zero-energy  $L = 0_2^+$  state is seen to be a pure  $n_d = 0$  state which is the solvable  $U(5)$ -PDS eigenstate of Eq. (20a). The state  $2_2^+$  has a pronounced  $n_d = 1$  component (96%) and the states ( $L = 0_4^+, 2_5^+, 4_3^+$ ) in the third panel, have a pronounced  $n_d = 2$  component. All the above states with ‘ $n_d \leq 2$ ’ have a dominant single  $n_d$  component, and hence qualify as ‘spherical’ type of states. These multiplets comprise the lowest left-most states shown in the combined Peres lattices for  $\xi_c = 0$  in Fig. 17. In contrast, the states in the panels ‘ $n_d = 3$ ’ and ‘ $n_d = 4$ ’ of Fig. 19, are significantly fragmented. Notable exceptions are the  $L = 3_2^+$  state, which is the solvable  $U(5)$ -PDS state of Eq. (20b) with  $n_d = 3$ , and the  $L = 5_2^+$  state with a dominant  $n_d = 4$  component. The existence in the spectrum of specific spherical-type of states with either  $P_{n_d}^{(L_i)} = 1$  or  $P_{n_d}^{(L_i)} \approx 1$ , exemplifies the presence of an exact or approximate  $U(5)$  PDS at the critical-point.

The states shown on the right column of Fig. 19, have a different character. They belong to the five lowest regular sequences seen in the combined Peres lattices for  $\xi_c = 0$  in Fig. 17. The association of a set of  $L_i$ -states to a given sequence, is based on a close proximity of their lattice points  $\{x_i, E_i\}$ , and on having a similar decomposition in the  $SU(3)$  DS basis, to be discussed below. The states shown, exhibit a broad  $n_d$ -distribution, hence are qualified as ‘deformed’-type of states, forming rotational bands:  $g(K=0)$ ,  $\beta(K=0)$ ,  $\beta^2(K=0)$ ,  $\beta^3(K=0)$  and  $\gamma(K=2)$ . The bandhead energy of each  $K$ -band is listed in each panel. Note that the zero-energy deformed ground state,  $L = 0_1$ , is degenerate with the ( $n_d = 0, L = 0_2$ ) spherical state. The  $P_{n_d}^{(L_i)}$  probabilities for the  $K = 0$  bands in Fig. 19, display an oscillatory behavior, reflecting the expected nodal structure of these ground and multi  $\beta$ -phonon bands.



Fig. 20 shows the SU(3)  $(\lambda, \mu)$ -distribution,  $P_{(\lambda, \mu)}^{(L_i)}$  (69b), for the same eigenstates of the critical-point Hamiltonian as in Fig. 19. The spherical-type of states, shown on the left column, involve considerable mixing with respect to SU(3), without any obvious common pattern among states in the same ‘ $n_d$ ’ multiplet, and in marked contrast to their  $n_d$ -distribution shown in Fig. 19. The states in the ‘ $n_d \leq 2$ ’ multiplets involve higher SU(3) irreps, while those in the fragmented ‘ $n_d \geq 3$ ’ multiplets are more uniformly spread among all  $(\lambda, \mu)$ -components. The ‘rotational’-type of states, shown on the right column of Fig. 20, show again a very different behavior. First, the ground  $g(K=0)$  and the  $\gamma(K=2)$  bands are pure with  $(\lambda, \mu) = (2N, 0)$  and  $(2N-4, 2)$  SU(3) character, respectively. These are the solvable bands of Eq. (25) with SU(3) PDS. Second, the non-solvable  $K$ -bands are mixed with respect to SU(3), but the mixing is similar for the different  $L$ -states in the same band. Such strong but coherent ( $L$ -independent) mixing is the hallmark of SU(3) QDS. It results from the existence of a single intrinsic state for each such band and imprints an adiabatic motion and increased regularity [83].

By comparing the right hand side panels in Fig. 20, with the left hand side panels in Fig. 19, we find that the SU(3) QDS property of the ‘deformed’ states persists, while the U(5) PDS property of the spherical states dissolves at higher energy. This observation is in accord with the classical and quantum analyses. As portrayed in the Poincaré sections (Fig. 10) and Peres lattices (Figs. 17-18) at the critical point ( $\xi_c = 0$ ), the dynamics ascribed to the deformed well is regular and persists to energies higher than the barrier. In contrast, the dynamics ascribed to the spherical well, shows a Hénon-Heiles (HH) type of transition from regular to chaotic motion as the energy increases. A narrow chaotic layer in the classical phase space starts to occur at  $E \approx 0.1$ , while fully chaotic dynamics develops at  $E \approx 0.24$ , below the top of the barrier at  $V_{\text{bar}}/h_2 = 0.268$ . For the boson number  $N = 50$  considered, the ‘ $n_d = 0, 1$ ’ states in Fig. 19, lie in the energy domain of the regular HH dynamics, the ‘ $n_d = 2$ ’ triplet resides in the relatively-regular domain just above the appearance of the chaotic layer, while the ‘ $n_d = 3, 4$ ’ multiplets lie already near the barrier top, in the highly chaotic domain. Thus, the observed breakdown of the U(5)-character of the multiplets, can be attributed to the onset of chaos at higher energy in the region of the spherical well.

## 7.2. Measures of purity (PDS) and coherence (QDS)

The preceding discussion highlights the importance of U(5)-PDS and SU(3)-QDS in identifying and characterizing the persisting regular states. These symmetry notions rely on the purity and coherence of the states with respect to a DS basis. It is therefore of interest to have at hand quantitative measures for these properties.

The Shannon state entropy is a convenient tool to evaluate the purity of eigenstates with respect to a DS basis. Given a state  $|L_i\rangle$ , with U(5) and SU(3) decomposition as in Eq. (68), its U(5) and SU(3) entropies are defined as

$$S_{\text{U5}}(L_i) = -\frac{1}{\ln D_5} \sum_{n_d} P_{n_d}^{(L_i)} \ln P_{n_d}^{(L_i)}, \quad (70a)$$

$$S_{\text{SU3}}(L_i) = -\frac{1}{\ln D_3} \sum_{(\lambda, \mu)} P_{(\lambda, \mu)}^{(L_i)} \ln P_{(\lambda, \mu)}^{(L_i)}. \quad (70b)$$

Here  $P_{n_d}^{(L_i)}$  and  $P_{(\lambda, \mu)}^{(L_i)}$  are the U(5) and SU(3) probability distributions of Eq. (69). The normalization  $D_5$  ( $D_3$ ) counts the number of possible  $n_d$  [ $(\lambda, \mu)$ ] values for a given  $L$  and, for simplicity, their dependence on  $L_i$  and  $N$  is suppressed. A Shannon entropy vanishes when the considered state is pure with good  $G$ -symmetry [ $S_G(L_i) = 0$ ] and is positive for a mixed state. The maximal value [ $S_G(L_i) = 1$ ] is obtained when the state  $|L_i\rangle$  is uniformly spread among the irreps of  $G$ , *i.e.* for  $P_G^{(L_i)} = 1/D_G$ . Intermediate values,  $0 < S_G(L_i) < 1$ , indicate partial fragmentation of the state  $|L_i\rangle$  in the respective DS basis. The averaging of such quantities over all eigenstates has been previously used to disclose the global DS content of the IBM Hamiltonian, Eq. (13), and to correlate the implied degree of the eigenfunction localization with chaotic measures [88, 89].

The values of the U(5) entropy  $S_{U5}(L_i)$ , Eq. (70a), are listed for representative states in Fig. 19. As expected,  $S_{U5} = 0$  for the solvable U(5)-PDS states, Eq. (20), with  $(n_d = 0, L = 0_2)$  and  $(n_d = 3, L = 3_2)$ . Other spherical-type of states with ‘ $n_d \leq 2$ ’ have a low value,  $S_{U5} < 0.15$ , while the more dispersed states with ‘ $n_d = 3, 4$ ’ have  $S_{U5} > 0.40$ . The deformed-type of states, shown on the right column of Fig. 19, have a large U(5) entropy,  $S_{U5} > 0.67$ . The values of the SU(3) entropy  $S_{SU3}(L_i)$ , Eq. (70b), are shown for selected states in Fig. 20. As expected,  $S_{SU3} = 0$  for the solvable SU(3)-PDS states, Eq. (25), members of the  $g(K = 0)$  and  $\gamma(K = 2)$  bands. The deformed  $\beta^n(K = 0)$  bands are mixed with respect to SU(3), hence have non-zero values of  $S_{SU3}$ , which increase with  $n$ . The spherical-type of states, shown on the left column of Fig. 20, are strongly mixed with respect to SU(3) and have  $S_{SU3} > 0.72$ .

The coherent decomposition characterizing SU(3) QDS, implies strong correlations between the SU(3) components of different  $L$ -states in the same band. This can be used as a criterion for the identification of rotational bands. We focus here on the  $L = 0, 2, 4, 6$ , members of  $K = 0$  bands. Given a  $L = 0_i^+$  state, among the ensemble of possible states, we associate with it those  $L_j > 0$  states which show the maximum correlation,  $\max_j \{\pi(0_i, L_j)\}$ . Here  $\pi(0_i, L_j)$  is a Pearson correlation coefficient whose values lie in the range  $[-1, 1]$ . Specifically,  $\pi(0_i, L_j) = 1, -1, 0$ , indicate a perfect correlation, a perfect anti-correlation, and no linear correlation, respectively, among the SU(3) components of the  $0_i$  and  $L_j$  states. More details on these coefficients in conjunction with the present study, are discussed in Appendix B. To quantify the amount of coherence (hence of SU(3)-QDS) in the chosen set of states, we adapt the procedure proposed in [81], and consider the following product of the maximum correlation coefficients

$$C_{SU3}(0_i-6) \equiv \max_j \{\pi(0_i, 2_j)\} \max_k \{\pi(0_i, 4_k)\} \max_\ell \{\pi(0_i, 6_\ell)\} . \quad (71)$$

We consider the set of states  $\{0_i, 2_j, 4_k, 6_\ell\}$  as comprising a  $K = 0$  band with SU(3)-QDS, if  $C_{SU3}(0_i-6) \approx 1$ .

The values of  $C_{SU3}(0_i-6)$  for selected sets of states are shown in Fig. 20. As expected,  $C_{SU3}(0_i-6) \approx 1$  for all the ‘deformed’  $K$ -bands. On the other hand, this quantity is much smaller (but still non-zero) for the spherical-type of states. Band structure based on SU(3) QDS thus necessitates a value of  $C_{SU3}(0_i-6)$  in very close proximity to 1. It should be noted that the coherence properly of a band of states, as measured by  $C_{SU3}(0_i-6)$ , is independent

of its purity, as measured by  $S_{\text{SU3}}(L_i)$ . Thus, in Fig. 20, the pure  $g(K=0)$  and  $\gamma(K=2)$  bands with SU(3) PDS have  $C_{\text{SU3}}(0_i-6) = 1$  or  $C_{\text{SU3}}(2_i-8) = 1$  and  $S_{\text{SU3}} = 0$ , while the mixed  $\beta^3(K=0)$  band has  $C_{\text{SU3}}(0_i-6) = 0.9996$  and  $S_{\text{SU3}} = 0.406$ .

### 7.3. Evolution of U(5)-PDS and SU(3)-QDS across the QPT

We turn now to a detailed study of the evolution of partial- and quasi-dynamical symmetries across the first order QPT, induced by the intrinsic Hamiltonian  $\hat{H}_1(\rho)$ , Eq. (7a), and  $\hat{H}_2(\xi)$ , Eq. (7b), with  $\beta_0 = \sqrt{2}$ . For that purpose, we examine the change in the Shannon entropies,  $S_{\text{U5}}(L_i)$  and  $S_{\text{SU3}}(L_i)$ , Eq. (70), and in the SU(3) correlation coefficient  $C_{\text{SU3}}(0_i-6)$ , Eq. (71), as a function of the control parameters,  $0 \leq \rho \leq \rho_c$  and  $\xi_c \leq \xi \leq 1$ , for the entire spectrum.

Fig. 21 displays the values of the U(5) Shannon entropy  $S_{\text{U5}}(L)$ , Eq. (70a), for  $L = 0$  (bottom) and  $L = 2$  (top) eigenstates of  $\hat{H}_{\text{int}}$  (7), with  $N = 50$ . The vertical axis lists the energy  $E$  of the states, while the horizontal axis lists 35 values of the control parameters  $(\rho, \xi)$ . Vertical dashed lines which embrace each control parameter, correspond to the value  $S_{\text{U5}}(L) = 0$  (left) and  $S_{\text{U5}}(L) = 1$  (right). Thus, states which are pure with respect to U(5) (hence with  $S_{\text{U5}}(L) = 0$ ), are represented by points on the vertical dashed line to the left of the given control parameter. Departures from this vertical line,  $0 < S_{\text{U5}}(L) \leq 1$ , indicate the amount of U(5) mixing. For clarity, the values of  $S_{\text{U5}}(L)$  at the U(5) DS limit ( $\rho_{\text{U(5)}} = 0$ ), the spinodal ( $\rho^*$ ), the critical ( $\rho_c, \xi_c$ ), and the anti-spinodal ( $\xi^{**}$ ) points, and the SU(3) DS limit ( $\xi_{\text{SU(3)}} = 1$ ), are distinguished by a different (blue) color. To gain further insight, the stationary and asymptotic values ( $V_{\text{sph}}, V_{\text{max}}, V_{\text{def}}, V_{\text{bar}}, V_{\text{sad}}, V_{\text{lim}}$ ) of the relevant classical potentials, are depicted by dashed black lines (compare with Fig. 3).

Starting on the spherical side of the QPT, at the U(5) DS limit ( $\rho_{\text{U(5)}} = 0$ ), the U(5) entropy,  $S_{\text{U5}}(L) = 0$ , vanishes for all states. The spherical  $L = 0_1$  ground state of  $\hat{H}_1(\rho)$  maintains  $S_{\text{U5}}(L = 0_1) = 0$  throughout region I ( $0 \leq \rho \leq \rho^*$ ) and in part of region II ( $\rho^* < \rho \leq \rho_c$ ), in accord with its U(5)-PDS property, Eq. (20a). As seen in Fig. 21, for  $\rho > 0$ , all other  $L = 0, 2$  eigenstates of  $\hat{H}_1(\rho)$  have positive  $S_{\text{U5}}(L) > 0$ , reflecting their U(5) mixing.  $S_{\text{U5}}(L)$  attains small positive values at low energy, corresponding to spherical-type of states, and changes to moderate and high values as the energy increases, indicating stronger U(5) mixing. The departures of  $S_{\text{U5}}(L)$  from zero value start to occur at lower energy, as  $\rho$  approaches  $\rho^*$ . This behavior is consistent with the Hénon Heiles type of dynamics and the onset of chaos in this region. In region III ( $\xi^{**} \leq \xi \leq 1$ ) all states, including the ground state of  $\hat{H}_2(\xi)$ , have  $S_{\text{U5}}(L) \in [0.7, 0.9]$ , exhibiting weaker variation with energy. These large values reflect the deformed nature of the underlying eigenstates, which are arranged in rotational bands. In region II of phase coexistence ( $\rho^* < \rho \leq \rho_c$  and  $\xi_c \leq \xi < \xi^{**}$ ),  $S_{\text{U5}}(L)$  attains both low and high positive values, reflecting the presence of both spherical- and deformed-type of states. This creates a zig-zag pattern, especially visible in the triangular region bordered by the energies of the barrier ( $V_{\text{bar}}$ ) and of the (deformed or spherical) local minima ( $V_{\text{def}}$  or  $V_{\text{sph}}$ ).

In spite of the U(5) mixing present in the overwhelming majority of eigenstates, a subset of low-lying states in regions I and II exhibit pronounced low-values of  $S_{\text{U5}}(L)$ , indicating an enhanced purity with respect to U(5). Such states are members of U(5)-like multiplets, of

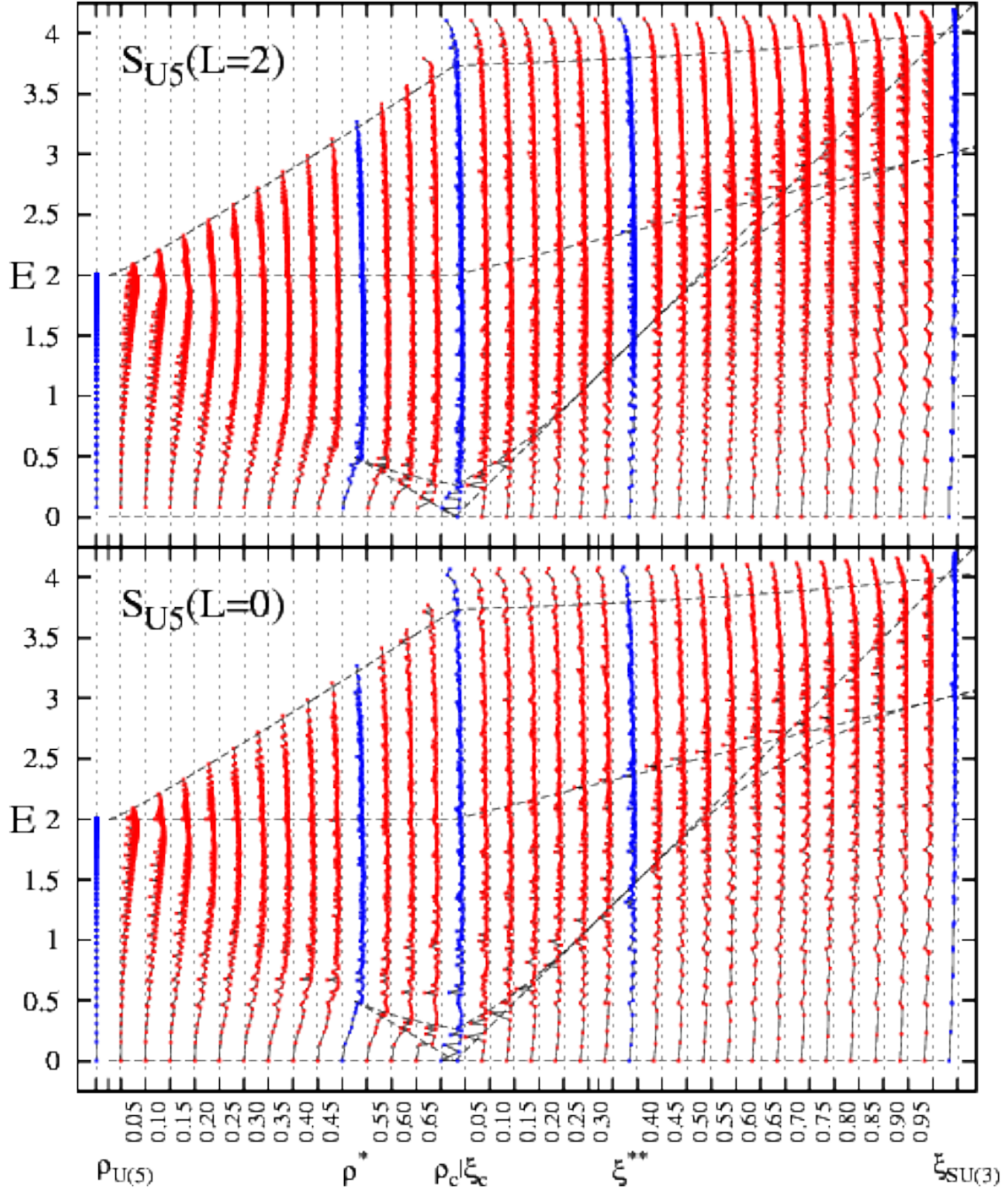


Figure 21:  $U(5)$  Shannon entropy  $S_{U5}(L)$ , Eq. (70a) for  $L = 2$  (top) and  $L = 0$  (bottom) eigenstates of the intrinsic Hamiltonian (7), with  $h_2 = 1$ ,  $\beta_0 = \sqrt{2}$ ,  $N = 50$ , as a function of the control parameters  $(\rho, \xi)$ . Vertical dashed lines to the left (right) of each numbered control parameter, indicate the value  $S_{U5}(L) = 0$  [ $S_{U5}(L) = 1$ ]. Black dashed lines depict the stationary and asymptotic values of the relevant classical potentials (compare with Fig. 3).  $S_{U5}(L) \approx 1$  indicates an approximate  $U(5)$ -PDS.

the form discussed in Fig. 19. Their wave functions are dominated by a single  $n_d$  component, which has the largest (maximal)  $n_d$ -probability,  $P_{n_d}^{(L_i)}$ , for a given  $(n_d, L)$ . These spherical type of states thus exemplify the persistence of an (approximate) U(5) PDS.

The top panel of Fig. 22 displays the values of the SU(3) Shannon entropy  $S_{\text{SU}(3)}(L=0)$ , Eq. (70b), for the entire energy spectrum of  $L=0$  states. The notation of lines is the same as in Fig. 21. Thus, states which are pure with respect to SU(3), are represented by points on the vertical dashed line to the left of the given control parameter, corresponding to  $S_{\text{SU}(3)}(L=0) = 0$ . Departures from this vertical line,  $0 < S_{\text{SU}(3)}(L) \leq 1$ , indicate the amount of SU(3) mixing. The bottom panel of Fig. 22 displays the values of the SU(3) correlation coefficient  $C_{\text{SU}(3)}(0-6)$ , Eq. (71), correlating sequences of  $L=0, 2, 4, 6$ , states, throughout the entire spectrum. The energy  $E$ , listed on the vertical axis, corresponds here to the energy of the  $L=0$  eigenstate in each sequence. The vertical dashed lines which embrace each control parameter  $(\rho, \xi)$ , correspond now to the value  $C_{\text{SU}(3)}(0-6) = 0$  (left) and  $C_{\text{SU}(3)}(0-6) = 1$  (right). Thus, a highly-correlated sequence of  $L=0, 2, 4, 6$  states, comprising a  $K=0$  band and manifesting SU(3)-QDS, are represented by points lying on or very close to the vertical dashed line to the right of the given control parameter, corresponding to  $C_{\text{SU}(3)}(0-6) \approx 1$ . Even slight departures from this vertical line,  $C_{\text{SU}(3)}(0-6) < 1$ , indicate a reduction of SU(3) coherence.

Starting on the deformed side of the QPT, at the SU(3) DS limit ( $\xi_{\text{SU}(3)} = 1$ ), the SU(3) entropy,  $S_{\text{SU}(3)}(L) = 0$ , vanishes for all states. In this case, the  $L$ -states in a given  $K$ -band belong to a single SU(3) irrep, hence necessarily  $C_{\text{SU}(3)}(0-6) = 1$ . As one departs from the symmetry limit, ( $\xi < 1$ ),  $S_{\text{SU}(3)}(L=0) > 0$  acquires positive values, reflecting an SU(3) mixing. The SU(3) breaking becomes stronger at higher energies and as  $\xi$  approaches  $\xi_c = 0$  from above, resulting in higher values of  $S_{\text{SU}(3)}(L=0)$ . A notable exception to this behavior is the deformed ground state ( $L=0_1$ ) of  $\hat{H}_2(\xi)$ , which maintains  $S_{\text{SU}(3)}(L=0_1) = 0$  throughout region III ( $\xi^{**} \leq \xi \leq 1$ ) and in part of region II ( $\xi_c \leq \xi < \xi^{**}$ ), in accord with its SU(3)-PDS property, Eq. (25a). In contrast to the lack of SU(3)-purity in all excited  $L=0$  states, the SU(3) correlation function maintains a value close to unity,  $C_{\text{SU}(3)}(0-6) \approx 1$ . This indicates that the SU(3) mixing is coherent and that these  $L=0$  states serve as bandhead states of  $K=0$  bands with a pronounced SU(3) QDS. This band-structure is observed throughout region III in extended energy domains. In particular, all such  $K=0$  bands show strong coherence up to the energy of the saddle point  $V_{\text{sad}}$ , Eq. (54b), for  $\xi > \xi^{**}$ , or of the spherical local minimum  $V_{\text{sph}}$ , Eq. (45), for  $\xi < \xi^{**}$ . This observation is consistent with the classical analysis, which revealed a robustly regular dynamics in this region. Coherent  $K=0$  bands can also be seen at high energy above  $V_{\text{sph}}$  in regions III and II of Fig. 22. One observes here numerous sequences of points with  $C_{\text{SU}(3)}(0-6) = 1$ , alternating with other points for which  $C_{\text{SU}(3)}(0-6) < 0.7$ . The former correspond to the regular states, identified by the Peres lattices in Fig. 16, while the latter correspond to irregular (chaotic) states. In particular, at energies below  $V_{\text{lim}}$ , Eq. (44), there is a very sharp distinction between the two families, corresponding to the sharp distinction between the regular and chaotic states (dynamics) observed in the Peres lattices (Poincaré surfaces). At very high energies, above  $V_{\text{lim}}$ , some incoherence appears, consistent with the onset of chaos in region III.

In region I ( $0 \leq \rho \leq \rho^*$ ), all states exhibit high values of  $S_{\text{SU}(3)}(L=0) \approx 1$  and

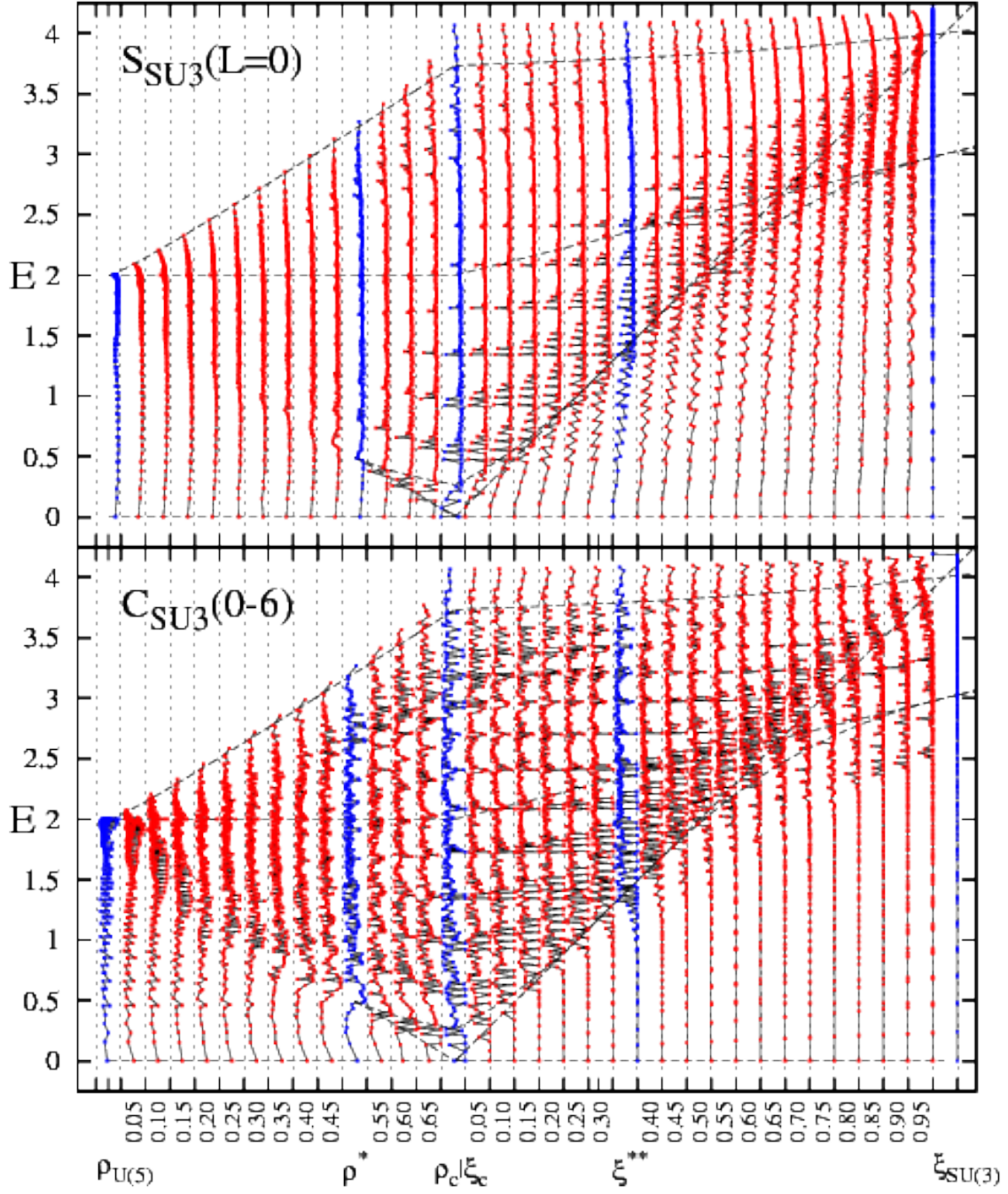


Figure 22: As in Fig. 21, but for the SU(3) Shannon entropy  $S_{\text{SU}(3)}(L=0)$ , Eq. (70b), (top panel) and the SU(3)-correlation coefficient  $C_{\text{SU}(3)}(0-6)$ , Eq. (71), (bottom panel), as a function of the control parameters  $(\rho, \xi)$  and the energy  $E$  of  $L=0$  states. Vertical dashed lines to the left (right) of each numbered control parameter, indicate the value 0 (1) for both quantities.  $S_{\text{SU}(3)}(L=0) \approx 1$  indicates an enhanced SU(3) purity, while  $C_{\text{SU}(3)}(0-6) \approx 1$  indicates a  $K=0$  band exhibiting SU(3)-QDS.



$C_{\text{SU}3}(0-6) < 1$ , indicating considerable SU(3) mixing and lack of SU(3) coherence. This is in line with the presence of spherical states at low energy, and of more complex type of states at higher energy, and the absence of rotational bands in this region. In region II of phase coexistence ( $\rho^* < \rho \leq \rho_c$  and  $\xi_c \leq \xi < \xi^{**}$ ), one encounters both, points with  $C_{\text{SU}3}(0-6) \approx 1$ , and points with  $C_{\text{SU}3}(0-6) < 1$ . This reflects the presence of deformed states arranged into regular bands, exemplifying SU(3) QDS and, at the same time, the presence of spherical states and other more complicated type of states of a different nature.

#### 7.4. Global features of U(5) PDS and SU(3) QDS as fingerprints of the QPT

The preceding discussion has demonstrated the relevance of U(5) PDS and SU(3) QDS in characterizing the symmetry properties of individual quantum eigenstates of the intrinsic Hamiltonian across the QPT. The related measures of these quasi-symmetries, the U(5) Shannon entropy,  $S_{\text{U}5}(L)$ , Eq. (70a), and the SU(3) correlation coefficient,  $C_{\text{SU}3}(0-6)$ , Eq. (71), quantify the U(5)-purity and SU(3)-coherence in these states, respectively. Considerable interest is drawn to subsets of regular states which maintain a high degree of purity or coherence amidst a complicated environment of other states. In particular, a small value of  $S_{\text{U}5}(L)$  signals an approximate U(5) PDS and identifies subsets of spherical-type of states which reflect a surviving regular dynamics in the vicinity of the spherical minimum. On the other hand, a large value of  $C_{\text{SU}3}(0-6) \approx 1$  signals an SU(3) QDS and identifies rotational  $K$ -bands, which reflect a persisting regular dynamics in the vicinity of the deformed minimum. In the present Section, we wish to consider global features of these measures which can shed light on the PDS and QDS content of the entire system as a whole, and monitor its evolution across the the QPT.

The presence or absence in the spectrum of spherical or deformed type of regular states, is intimately tied with the existence and depth of the corresponding spherical or deformed wells in the classical potential. As seen in Figs. 21-22, the number of such regular states is maximal at the DS limits and it reduces as the control parameters approach the values of the anti-spinodal or spinodal points, where the respective local minimum disappears. The evolution with  $(\rho, \xi)$  of the number of states having an approximate U(5) PDS or SU(3) QDS reflects the change in the morphology of the underlying Landau potential and can, therefore, serve as fingerprints of the QPT.

As a global measure of an approximate U(5) PDS, we consider the quantity  $\nu_{\text{U}5}$ , which denotes the number of  $L = 0$  states satisfying  $S_{\text{U}5}(L = 0) < 0.25$ . This quantity is an indicator of the amount of enhanced U(5)-purity in the system. The choice of 0.25 as an upper limit is somewhat arbitrary, and is close to the value of  $S_{\text{U}5}(L = 0) = 0.242$  at  $\xi = 0.17$  for which the maximal U(5) probability is  $P_{n_d=0}^{(L=0)} = 0.8$ . Analogous quantities,  $\nu_{\text{U}5}(L)$ , can be calculated for states with other angular momentum  $L$ . Henceforth, we continue to use the shorthand notation,  $\nu_{\text{U}5} \equiv \nu_{\text{U}5}(L = 0)$ . In a similar spirit, as a global measure of SU(3) QDS, we consider the the quantity  $\nu_{\text{SU}3}$ , which denotes the number of  $K = 0$  bands whose  $L = 0, 2, 4, 6$  members satisfy  $C_{\text{SU}3}(0-6) > 0.995$ . This quantity is an indicator of the amount of SU(3) coherence in the system. The choice of 0.995 as a lower limit is again somewhat arbitrary. It is based on a detailed study of the SU(3) correlator for the regular  $K = 0$  bands in Fig. 22, which revealed a well-separated peak in the range

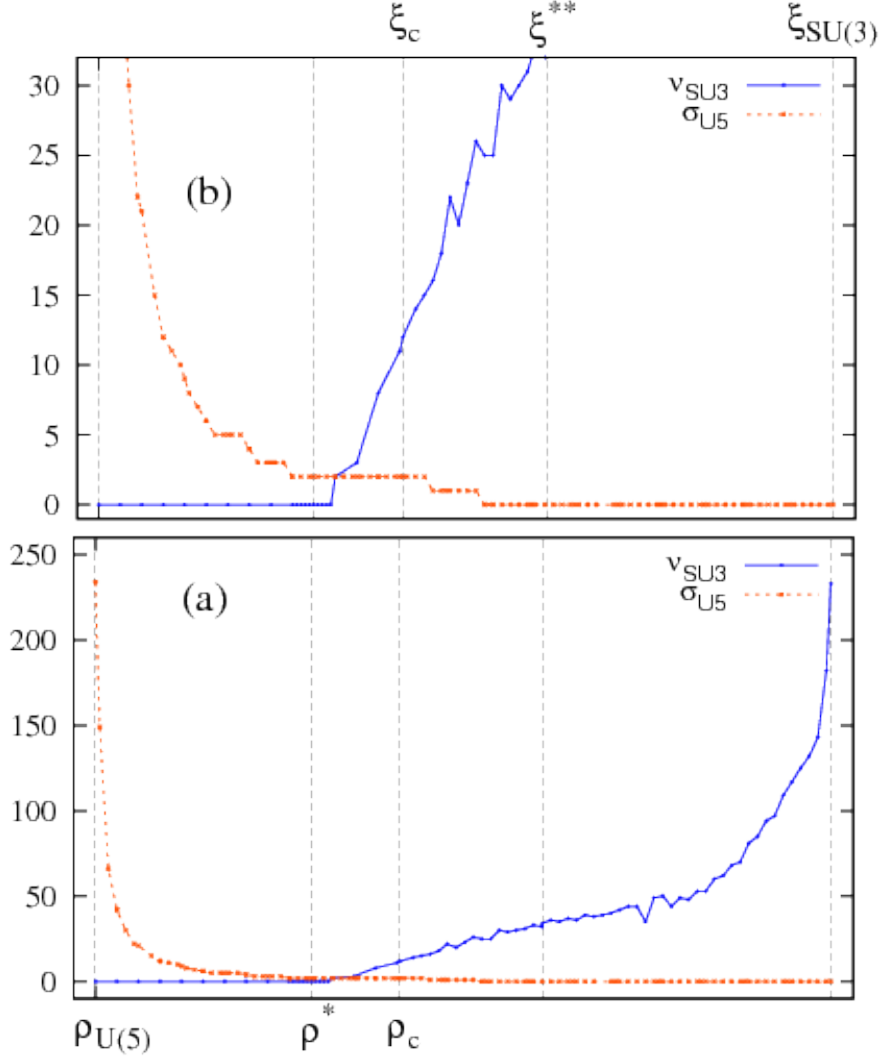


Figure 23: Global measures of U(5) PDS [ $\nu_{U5}$ : the number of  $L = 0$  states with U(5) Shannon entropy  $S_{U5}(L = 0) < 0.25$ , Eq. (70a)] and of SU(3) QDS [ $\nu_{SU3}$ : the number of  $K = 0$  bands with SU(3) correlator  $C_{SU3}(0-6) > 0.995$ , Eq. (71)], as a function of  $(\rho, \xi)$ . (a) Full evolution across the QPT. (b) A detailed zoom. At the critical point  $(\rho_c, \xi_c)$ ,  $\nu_{U5} = 2$  and  $\nu_{SU3} = 12$ , compared to a total of 234  $L = 0$  eigenstates of the Hamiltonian (7) with  $\beta_0 = \sqrt{2}$  and  $N = 50$ .

$C_{SU3}(0-6) \in [0.995, 1]$ . It should be pointed out that the chosen cutoff values for  $\nu_{U5}$  and  $\nu_{SU3}$  apply to eigenstates of the intrinsic Hamiltonian (7) with  $\beta_0 = \sqrt{2}$  and  $N = 50$ , and in general these thresholds vary with  $N$ .

Fig. 23 displays the quantities  $\nu_{U5}$  and  $\nu_{SU3}$  as a function of the control parameters  $(\rho, \xi)$  across the QPT. At the U(5) DS limit ( $\rho_{U(5)} = 0$ ), all states are pure with respect to U(5) and hence, as seen in panel (a) of Fig. 23,  $\nu_{U5} = 234$  equals the total number of  $L = 0$  states for  $N = 50$ . For  $\rho > 0$ , the quantity  $\nu_{U5}$  decreases, indicating a reduction in the U(5) PDS of the system in region I. This reduction in the U(5) purity is accelerated for



larger values of  $\rho$  (stronger U(5) mixing), as the system enters region II of phase-coexistence ( $\rho^* < \rho \leq \rho_c$  and  $\xi_c \leq \xi < \xi^{**}$ ). Inside region II,  $\nu_{U5}$  attains smaller values, it vanishes as  $\xi$  approaches the anti-spinodal  $\xi^{**}$ , where the spherical minimum disappears, and remains  $\nu_{U5} = 0$  in region III ( $\xi \geq \xi^{**}$ ). Similar trends are seen for  $\nu_{U5}(L)$  involving states with different angular momentum when scaled by the number of states for each  $L$ .

At the SU(3) DS limit ( $\xi_{SU(3)} = 1$ ), all states are pure and coherent with respect to SU(3), in particular, all  $L = 0$  states serve as bandheads of  $K = 0$  bands and hence  $\nu_{SU3} = 234$  in panel (a) of Fig. 23. For  $\xi < 1$ , the quantity  $\nu_{SU3}$  decreases, indicating a reduction in the number of regular  $K = 0$  bands with SU(3) QDS, as the deformed well becomes less deep in region III. This reduction in SU(3) coherence continues inside region II of phase coexistence where ‘spherical’ states and chaotic-type of states come into play. The quantity  $\nu_{SU3}$  vanishes as  $\rho$  approaches the spinodal point  $\rho^*$ , where the deformed minimum disappears, and remains  $\nu_{SU3} = 0$  in region I ( $\rho \leq \rho^*$ ).

Panel (b) of Fig. 23 zooms in and provides more details on the evolution of  $\nu_{U5}$  and  $\nu_{SU3}$ . As shown, both quantities are non-zero throughout region II, indicating the presence of both (approximate) U(5) PDS and SU(3) QDS inside the coexistence region. These global measures of purity and coherence in selected eigenstates, thus trace the crossing of the spherical and deformed minima in the Landau potential by monitoring the remaining regular dynamics associated with each of them. The vanishing of  $\nu_{SU3}$  near  $\rho^*$ , appears to be sharper and less gradual than the vanishing of  $\nu_{U5}$  which occurs even before  $\xi < \xi^{**}$ . This reflects the more abrupt disappearance of the deformed minimum at  $\rho^*$  compared to the disappearance of the spherical minimum at  $\xi^{**}$  [compare the behavior of  $(V_{\text{bar}} - V_{\text{def}})$  near  $\rho^*$  with that of  $(V_{\text{bar}} - V_{\text{sph}})$  at  $\xi \leq \xi^{**}$ , in Fig. 3].

It is worthwhile emphasizing that both (approximate) U(5) PDS and SU(3) QDS are present in region II of phase coexistence, including the critical point, imprinting in a transparent manner, the evolution of the first-order QPT. A number of factors have facilitated the exposure of such a simple pattern in the present study; (i) a high barrier, (ii) a wide coexistence region, (iii) invoking the resolution of the Hamiltonian, Eq. (4), and performing the analysis on its intrinsic part. The latter does not contain rotation-vibration terms that can spoil the simple patterns observed. The effect of such collective kinetic terms will be considered in Section 8. The rich symmetry structure uncovered in region II and the coexistence of PDS and QDS inside it, were not noticed in previous works because the Hamiltonians employed did not meet the requirements (i)-(iii).

## 8. Collective effects

The analysis presented so far, considered the evolution of the dynamics associated with the intrinsic part of the Hamiltonian across the QPT. The intrinsic Hamiltonian determines the Landau potential and the variation of its control parameters  $(\rho, \xi)$  induces the shape-phase transition. In the present Section, we address the impact on the order and chaos accompanying the QPT, of the remaining collective part of the Hamiltonian. For that purpose, we examine the classical and quantum dynamics of the combined Hamiltonian

$$\hat{H} = \hat{H}_{\text{int}}(\rho, \xi) + \hat{H}_{\text{col}}(c_3, c_5, c_6) . \quad (72)$$

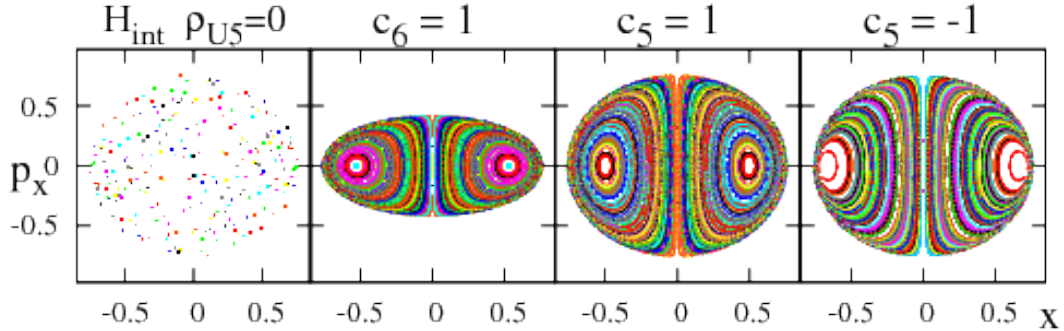


Figure 24: Poincaré sections of the classical intrinsic Hamiltonian  $\mathcal{H}_1(\rho = 0)$ , Eq. (26a), at the U(5)-DS limit ( $\rho = 0$ ), with  $h_2 = 1$  and  $\beta_0 = \sqrt{2}$  (left panel), and of additional collective terms, Eq. (32), with  $c_6 = 1$  and  $c_5 = \pm 1$ , involving  $\overline{\text{O}(6)}$  and  $\text{O}(5)$  rotations. The energy is  $E = V_{\text{lim}}/2 = 1$ . The potential surface  $V_1(\rho = 0)$ , Eq. (38), is the same in all cases and is depicted in the  $\rho_{\text{U}(5)} = 0$  column of Fig. 9.

The intrinsic Hamiltonian considered,  $\hat{H}_{\text{int}}(\rho, \xi)$ , is that of Eq. (7) with  $h_2 = 1$  and  $\beta_0 = \sqrt{2}$ , interpolating between the U(5) ( $\rho = 0$ ) and SU(3) ( $\xi = 1$ ) DS limits. The collective Hamiltonian considered,  $\hat{H}_{\text{col}}(c_3, c_5, c_6)$ , is that of Eq. (6), composed of kinetic terms with couplings  $c_3$ ,  $c_5$  and  $c_6$ , associated with collective  $\text{O}(3)$ ,  $\text{O}(5)$  and  $\overline{\text{O}(6)}$  rotations in the Euler angles,  $\gamma$  and  $\beta$  degrees of freedom, respectively. By construction,  $\hat{H}$  and  $\hat{H}_{\text{int}}$  in Eq. (72) have the same Landau potential which is not influenced by  $\hat{H}_{\text{col}}$ . The observed modifications in the dynamics due to  $\hat{H}_{\text{col}}$ , are thus kinetic in nature, arising from momentum-dependent terms which vanish in the static limit. For simplicity, the impact of these rotational  $c_i$ -terms are studied individually, by adding them one at a time to  $\hat{H}_{\text{int}}(\rho, \xi)$ , the latter taken at representative values of  $(\rho, \xi)$  in regions I-II-III of the QPT. The results obtained indicate that, although the collective Hamiltonian does not affect the Landau potential, it can have dramatic effects on the onset of classical chaos, on the resonance structure and on the regular features of the quantum spectrum.

### 8.1. Classical analysis in the presence of collective terms

As previously done, we constrain the classical dynamics to zero angular momentum and visualize it by means of Poincaré sections. In such circumstances, the classical limit of the quantum Hamiltonian of Eq. (72) is given by

$$\mathcal{H} = \mathcal{H}_{\text{int}}(\rho, \xi) + \mathcal{H}_{\text{col}}(c_5, c_6) , \quad (73)$$

where the first term is the classical intrinsic Hamiltonian of Eq. (26) and the second term is the classical collective Hamiltonian of Eq. (32). The  $\text{O}(3)$   $c_3$ -term is absent from the latter since the classical dynamics is constraint to  $L = 0$ . The  $\text{O}(5)$   $c_5$ -term depends on  $p_\gamma^2$  hence affects the  $\gamma$  motion, while the  $\overline{\text{O}(6)}$   $c_6$ -term depends on  $T = p_\beta^2 + p_\gamma^2/\beta^2$ ,  $T^2$  and  $\beta^2 p_\beta^2$ , hence is the only collective term affecting the  $\beta$  motion. The plane of the Poincaré section is chosen as before at  $y = 0$  and its envelope at a given energy  $E$  is defined by  $\mathcal{H}(x, y = 0, p_x, p_y = 0) = E$ , resulting in the condition

$$\mathcal{H}_{\text{int}}(x, y = 0, p_x, p_y = 0) + c_6[(2 - x^2)p_x^2 - p_x^4] = E . \quad (74)$$

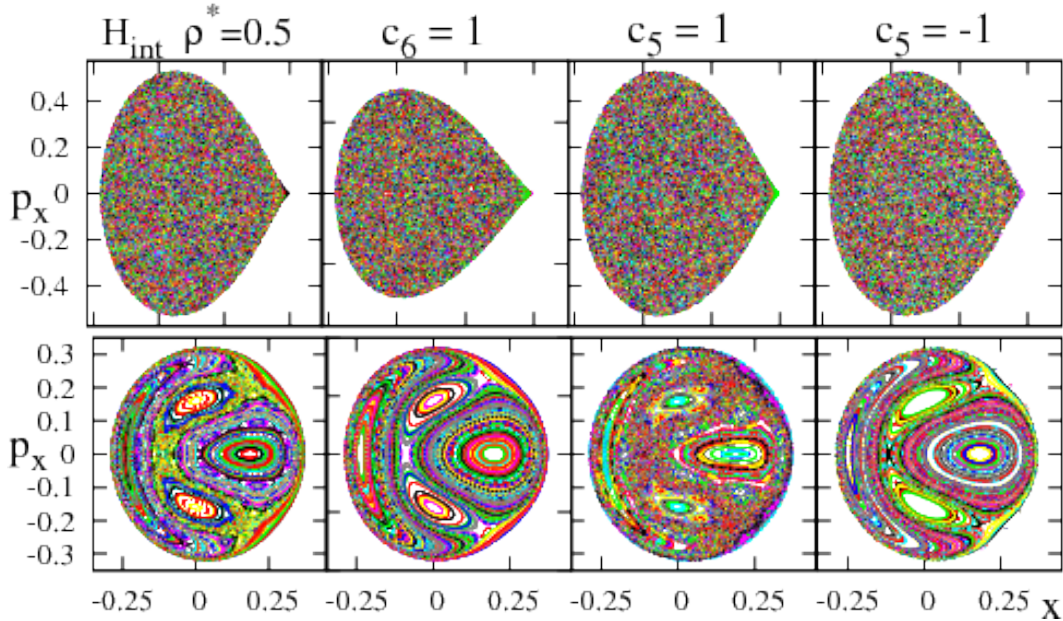


Figure 25: Poincaré sections of the classical intrinsic Hamiltonian  $\mathcal{H}_1(\rho^*)$ , Eq. (26a), at the spinodal point ( $\rho^*$ ), with  $h_2 = 1$  and  $\beta_0 = \sqrt{2}$  (left panel), and of additional collective terms, Eq. (32), with  $c_6 = 1$  and  $c_5 = \pm 1$ , involving  $\overline{O(6)}$  and  $O(5)$  rotations. The energy is  $E = V_{\text{lim}}/10 = 0.2$  (bottom row) and  $E = V_{\text{lim}}/4 = 0.5$  (top row). The potential surface,  $V_1(\rho^*)$ , Eq. (28a), is the same for all cases and is depicted in the  $\rho^* = 0.5$  column of Fig. 9.

As seen, the envelope of the full classical Hamiltonian  $\mathcal{H}$  is modified with respect to that of  $\mathcal{H}_{\text{int}}$ , solely due to the  $\overline{O(6)}$   $c_6$ -term.

Considering the classical dynamics of  $L = 0$  vibrations in the stable spherical phase (region I), the relevant classical intrinsic Hamiltonian in Eq. (73) is  $\mathcal{H}_1(\rho)$  of Eq. (26a), with  $0 \leq \rho \leq \rho^*$ . Fig. 24 shows for  $\rho = 0$  the Poincaré sections, at  $E = 1$ , of  $\mathcal{H}_1(\rho = 0)$  and of the added  $c_5$  and  $c_6$  collective terms. The potential surface is  $V_1(\rho = 0)$ , Eq. (38), the same in all panels. The  $c_5$ -term turns the exact  $U(5)$  symmetry of the intrinsic Hamiltonian into a  $U(5)$  dynamical symmetry of the combined Hamiltonian. The  $c_6$ -term breaks the  $U(5)$  symmetry but maintains the reduced symmetry of the  $O(5)$  subgroup. As a result, the system for  $\rho = 0$  remains integrable in the presence of both terms. The main effect is that the trajectories are no longer periodic but rather become quasi-periodic, start to precess and densely cover the surfaces of the invariant tori. In the Poincaré sections, instead of a finite collection of points, we now see smooth curves organized into two regular islands, forming a pattern typical of an anharmonic (quartic) oscillator. Fig. 25 shows similar sections, at  $E = 0.2$  (bottom) and  $E = 0.5$  (top), for the spinodal-point  $\rho = \rho^*$ . The relevant Landau potential is that depicted in the bottom panel of the  $\rho^* = 0.5$  column in Fig. 9. In general, the added collective terms maintain the characteristic features of the intrinsic classical dynamics, namely, a Hénon-Heiles type of transition from regular dynamics at low energy to chaotic dynamics at higher energy. The classical dynamics in the spherical region is, to a large extent, determined by

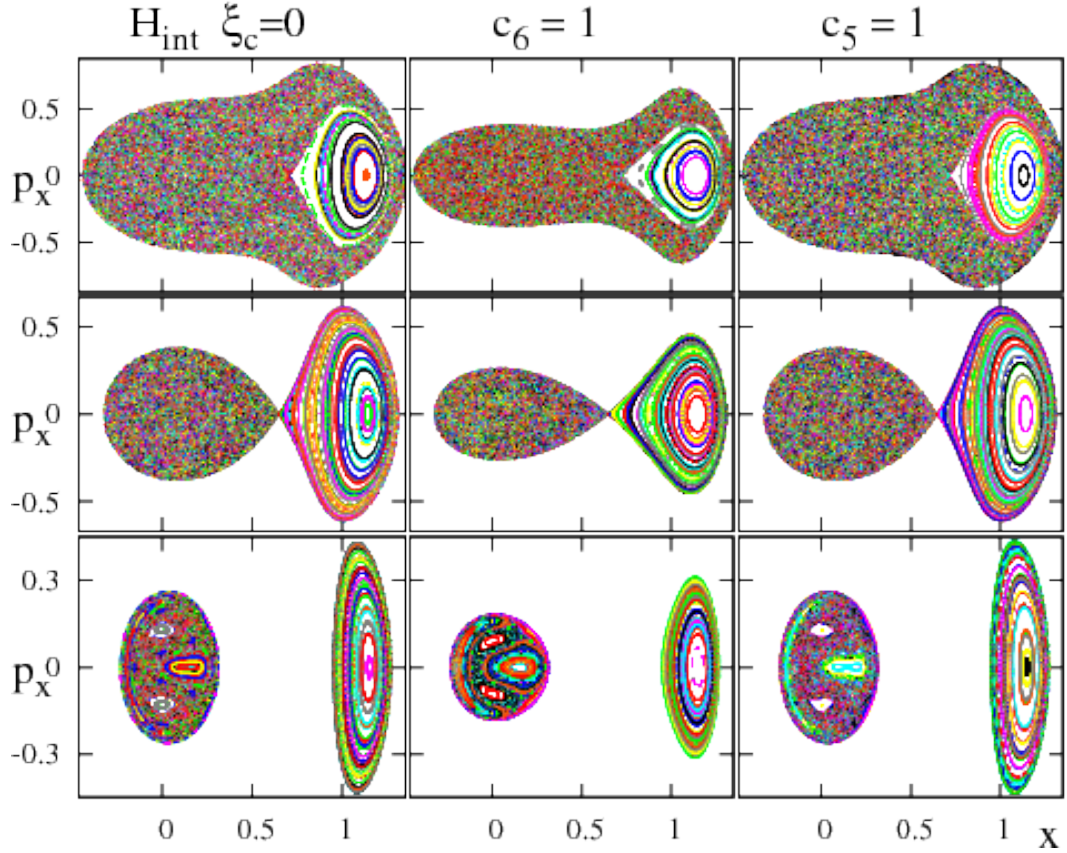


Figure 26: Poincaré sections of the classical intrinsic Hamiltonian  $\mathcal{H}_1(\rho_c) = \mathcal{H}_2(\xi_c)$ , Eq. (26), at the critical point  $(\rho_c, \xi_c)$ , with  $h_2 = 1$  and  $\beta_0 = \sqrt{2}$  (left panel), and of additional collective terms, Eq. (32), with  $c_6 = 1$  and  $c_5 = 1$ , involving  $O(6)$  and  $O(5)$  rotations. The energy is  $E = V_{\text{bar}}/2 = 0.134$  (bottom row),  $E = V_{\text{bar}} = 0.268$  (middle row) and  $E = 2V_{\text{bar}} = 0.536$  (top row). The potential surface  $V_1(\rho_c) = V_2(\xi_c)$ , Eq. (48), is the same for all cases and is depicted in the  $\xi_c = 0$  column of Fig. 10.

the  $\rho$ -term in the intrinsic Hamiltonian, Eq. (26a).

The classical intrinsic Hamiltonian in Eq. (73), appropriate to the coexistence region (region II), is  $\mathcal{H}_1(\rho)$  of Eq. (26a), with  $\rho^* < \rho \leq \rho_c$ , and  $\mathcal{H}_2(\xi)$  of Eq. (26b), with  $\xi_c \leq \xi < \xi^{**}$ . Fig. 26 displays the Poincaré surfaces for the critical point  $(\rho_c, \xi_c)$  with energies below, at, and above the barrier, arising from  $\mathcal{H}_1(\rho_c) \equiv \mathcal{H}_2(\xi_c)$  and from the added  $c_5$  and  $c_6$  rotational terms. The potential surface in all panels is that of Eq. (48), exhibiting a barrier separating the degenerate spherical and deformed minima. The  $c_5$ -term is seen to have a very little effect on the Poincaré sections of the intrinsic Hamiltonian. On the other hand, the sections with the  $c_6$ -term have a smaller size, and are compressed for large  $|p_x|$ , in accord with the properties of the envelope mentioned in Eq. (74). In addition, the regular island in the region of the deformed minimum appears to be more elongated in the  $x$ -direction (see the middle panel of the  $c_6 = 1$  column in Fig. 26). This distortion can affect the regular bands built on the deformed minimum, as will be discussed in the subsequent quantum analysis.

The different impact of the two collective terms on the classical dynamics can be attributed to the fact that in the coexistence region the barrier at the saddle point is in the  $\beta$ -direction, and hence is more sensitive to the  $\beta$  motion. As mentioned, the latter motion is affected by the  $\overline{O(6)}$  term but not by the  $O(5)$  term. In general, throughout region II, the presence of the collective terms in the Hamiltonian does not destroy the simple pattern of robustly regular dynamics confined to the deformed region and well-separated from the chaotic dynamics ascribed to the spherical region.

The classical intrinsic Hamiltonian in Eq. (73), relevant to the stable deformed phase (region III), is  $\mathcal{H}_2(\xi)$  of Eq. (26b), with  $\xi \geq \xi^{**}$ . For  $\xi = 1$ , the intrinsic Hamiltonian has  $SU(3)$  symmetry and the system is completely integrable. As seen in Fig. 27, the inclusion of the  $c_5$ - and  $c_6$ - rotational terms leads to substantial modifications in the phase space portrait, showing chaotic layers and additional islands.

Both the  $O(5)$  and  $\overline{O(6)}$  symmetries are incompatible with the  $SU(3)$  symmetry, hence the corresponding added rotational terms break the integrability of the intrinsic Hamiltonian at  $\xi = 1$ . This can lead to the occurrence of chaotic regions. The latter are more pronounced for the  $O(5)$  term (see the panels for  $c_5 = \pm 1$  in Fig. 27), which can be attributed to the fact that in region III, the saddle point accommodates a barrier in the  $\gamma$ -direction (see the contour plot in Fig. 2). It should be stressed that, in this case, the onset of chaos is entirely due to the kinetic terms of the collective Hamiltonian, since the intrinsic Hamiltonian is integrable for  $\xi = 1$  and its Landau potential, which has a single-deformed minimum, is kept intact in all panels of Fig. 27. This is a clear-cut demonstration that in the deformed side of the QPT, chaos can develop from purely kinetic perturbations, without a change in the morphology of the Landau potential.

The phase space portrait of the integrable intrinsic Hamiltonian at the  $SU(3)$  limit, shows the same pattern of two regular islands at any energy (see the  $\xi = 1$  column in Figs. 27 and 11). The inclusion of the collective terms modifies this pattern. As discussed in Section 5.3, the pattern of islands is affected by the presence of resonances which, in turn, occur at low energy when the ratio  $R$  of normal mode frequencies is a rational number. These resonance effects are influenced by the presence of the collective Hamiltonian. As seen in Eq. (12), both the  $c_5$ - and  $c_6$ - terms contribute to the normal-mode frequencies and hence change the ratio  $R$  of Eq. (59), to

$$R \equiv \frac{\epsilon_\beta}{\epsilon_\gamma} = \frac{h_2 \beta_0^2 (2\xi + 1) + c_6}{(9h_2 + c_5) \beta_0^2 (1 + \beta_0^2)^{-1} + c_6}. \quad (75)$$

In the current study, we adapt the values  $h_2 = 1$  and  $\beta_0 = \sqrt{2}$ , for which the above expression simplifies to  $R = [2(2\xi + 1) + c_6]/(6 + 2c_5/3 + c_6)$ .

For  $\xi = 1$ , the intrinsic Hamiltonian (with  $\beta_0 = \sqrt{2}$ ) has  $R = 1$ . The inclusion of the  $\overline{O(6)}$  rotational term does not alter this value, but it stabilizes an additional family of orbits circulating around, instead of passing through, the deformed minimum (see the unstable orbit of  $\mathcal{H}_2(\xi)$  for  $R = 1$  in Fig. 12). As a result, two additional regular islands develop in the Poincaré sections shown in the  $c_6 = 1$  column Fig. 27, compared to the  $SU(3)$  limit. The inclusion of the  $O(5)$  term changes the ratio to  $R = 9/(9 + c_5)$ , leading to  $R < 1$  ( $R > 1$ ) for



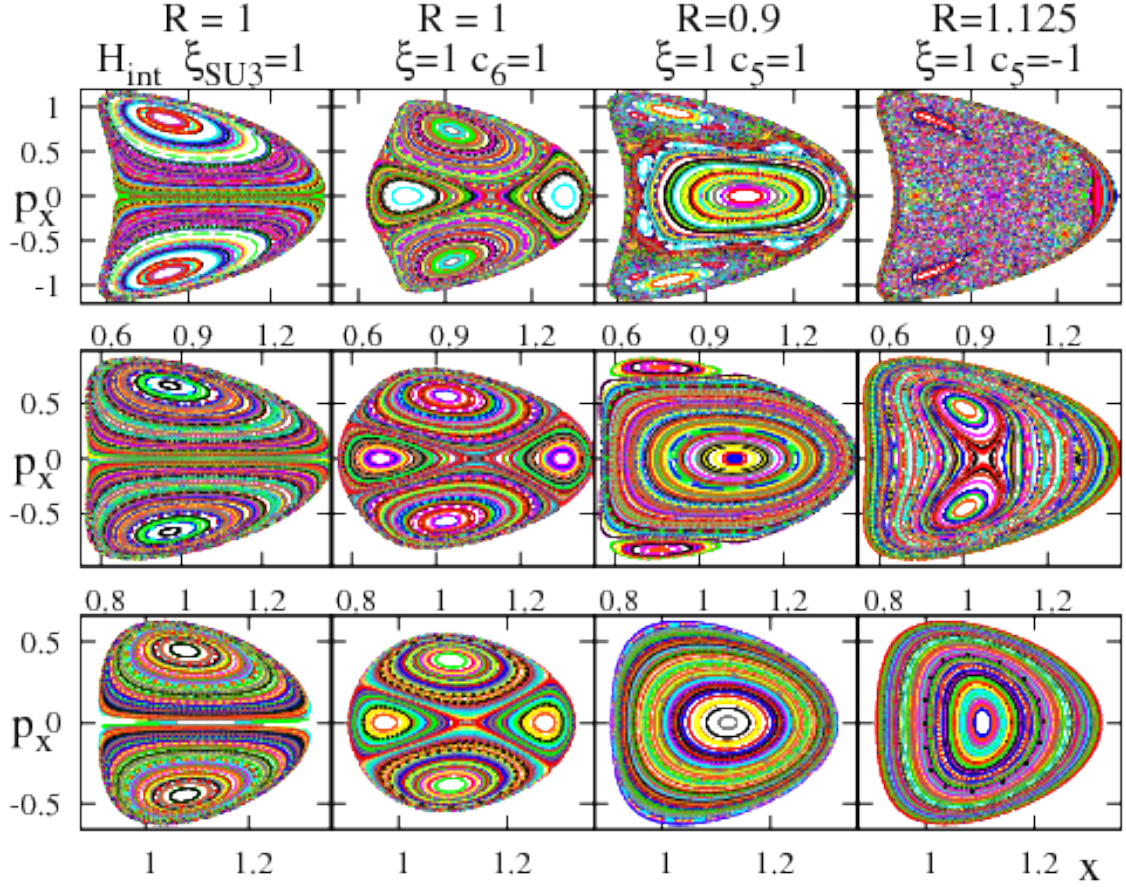


Figure 27: Poincaré sections of the classical intrinsic Hamiltonian  $\mathcal{H}_2(\xi = 1)$ , Eq. (26b), at the SU(3)-DS limit ( $\xi = 1$ ), with  $h_2 = 1$  and  $\beta_0 = \sqrt{2}$  (left panel) and of additional collective terms, Eq. (32), with  $c_6 = 1$  and  $c_5 = \pm 1$ , involving  $O(6)$  and  $O(5)$  rotations. The value of normal-mode frequency ratio  $R$ , Eq. (75), is indicated for each choice of parameters. The energy is  $E = V_{\text{lim}}/4 = 0.75$  (bottom row),  $E = V_{\text{lim}}/2 = 1.5$  (middle row) and  $E = 3V_{\text{lim}}/4 = 2.25$  (top row). The potential surface  $V_2(\xi = 1)$ , Eq. (28b), is the same in all cases and is depicted in the  $\xi_{\text{SU}(3)} = 1$  column of Fig. 11.

$c_5 > 0$  ( $c_5 < 0$ ). The  $\gamma$ -motion, with  $p_x \approx 0$ , is stable for  $R < 1$  and is unstable for  $R > 1$ . In the latter case, the center of the Poincaré section exhibits a hyperbolic fixed point and chaos develops in its vicinity as the energy increases (see the column with  $c_5 = -1$  in Fig. 27). On the other hand, the  $\beta$ -motion, with large  $|p_x|$ , is stable for  $R > 1$  and is unstable for  $R < 1$ . In the latter case, chaos develops at the perimeter of the Poincaré section (see the column with  $c_5 = 1$  in Fig. 27).

For  $\xi < 1$ , the integrability associated with the SU(3) limit is broken due to the presence of the  $(\xi - 1)P_0^\dagger P_0$  in the intrinsic Hamiltonian, Eq. (24). The effect of adding the rotational  $c_5$ -term on the classical dynamics, is similar to that of varying the control parameter  $\xi$  in the intrinsic Hamiltonian. This is illustrated in Fig. 28, where different combinations of  $\xi$  and  $c_5$ , which yield the same ratio  $R$ , give rise to similar Poincaré surfaces. Specifically, the surfaces

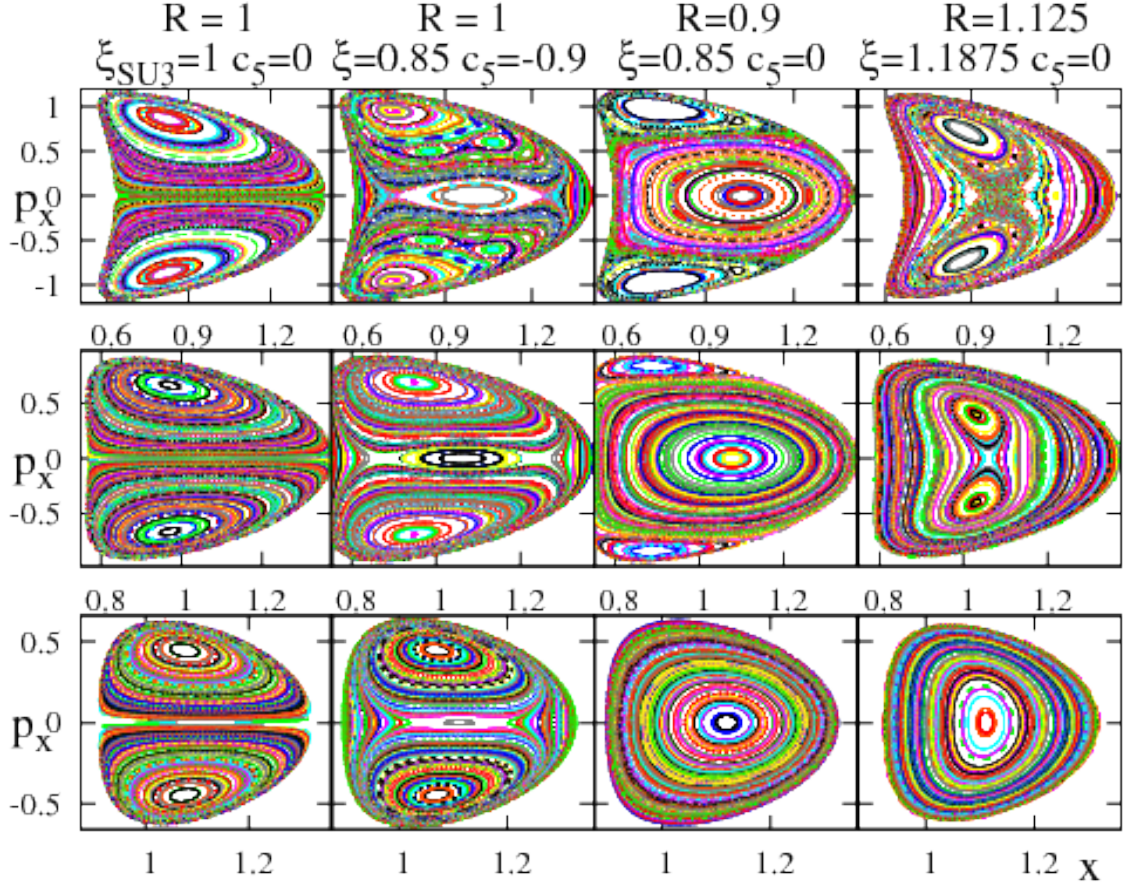


Figure 28: Poincaré sections of the classical intrinsic Hamiltonian  $\mathcal{H}_2(\xi)$ , Eq. (26b), with  $h_2 = 1$  and  $\beta_0 = \sqrt{2}$  in region III, without and with a  $c_5$ -term, Eq. (32). The energies are  $E = V_{\text{lim}}(\xi)/4$  (bottom row),  $E = V_{\text{lim}}(\xi)/2$  (middle row), and  $E = 3V_{\text{lim}}(\xi)/4$  (top row), where  $V_{\text{lim}}(\xi) = (2 + \xi)h_2$ . Note the similarity of surfaces in Figs. 27-28, with different values of  $(\xi, c_5)$ , but with the same value of normal mode frequency ratio  $R$ , Eq. (75).

obtained with  $(\xi = 0.85, c_5 = -0.9; R = 1)$  are similar (but not identical) to the surfaces at the SU(3) limit  $(\xi = 1, c_5 = 0; R = 1)$ , (compare the panels of the  $R = 1$  columns in Fig. 28). Similarly, the surfaces with  $(\xi = 0.85, c_5 = 0; R = 0.9)$  in Fig. 28 resemble the surfaces with  $(\xi = 1, c_5 = 1; R = 0.9)$  in Fig. 27, and the surfaces with  $(\xi = 1.1875, c_5 = 0; R = 1.125)$  in Fig. 28, resemble the surfaces with  $(\xi = 1, c_5 = -1; R = 1.125)$  in Fig. 27. The slight differences are due to anharmonic effects beyond the normal-mode approximation.

## 8.2. Quantum analysis in the presence of collective terms

The collective Hamiltonian  $\hat{H}_{\text{col}}(c_3, c_5, c_6)$  of Eq. (6), is composed of the two-body parts of the Casimir operators,  $\hat{C}_G$ , of the groups  $G = O(3), O(5), \overline{O(6)}$ . In studying their role in the quantum spectrum,  $\hat{C}_{O(3)}$  can be replaced by its eigenvalue  $L(L+1)$ , and has no effect on the structure of wave functions. For that reason, in the quantum analysis presented below, we focus on the effect of the collective O(5) and O(6) terms, when added to the intrinsic

Hamiltonian in various regions of the QPT. As previously done, the regular and irregular nature of the quantum states is revealed through the use of Peres lattices. Their symmetry properties are examined by means of Shannon entropies, Eq. (70), and the Pearson-based SU(3) correlator, Eq. (71). The former indicate the purity with respect to U(5) and SU(3), and the latter indicates the SU(3) coherence. These measures highlight the (approximate) U(5)-PDS and SU(3)-QDS content of the quantum eigenstates, across the QPT.

Figs. 29-32 portray the properties of quantum eigenstates of the full Hamiltonian, Eq. (72). The intrinsic Hamiltonian  $\hat{H}_{\text{int}}(\rho, \xi)$ , Eq. (7), has  $h_2 = 1$  and  $\beta_0 = \sqrt{2}$ , and the control parameters  $(\rho, \xi)$  are taken at representative values in regions I-II-III of the QPT. These values, as well as those of the coupling strengths,  $c_5$  and  $c_6$ , of the added collective terms, are identical to the ones used for the classical analysis in Figs 24-27. The middle (third) column in each of the Figures 29-32, displays the Peres lattices  $\{x_i, E_i\}$ , Eq. (66), of eigenstates  $|i\rangle$  with  $N = 50$  and  $L = 0, 2, 4, 6$ , which are overlaid on the corresponding classical potentials  $V(x, y = 0)$ , Eq. (31). These potentials are unchanged when the collective terms are included in the Hamiltonian. As before, ordered (disordered) meshes of lattice points, identify regular (irregular) type of states. The first, second and fourth columns from the left, display for each energy eigenstate  $E_i$ , the U(5) Shannon entropy  $S_{U5}(L_i)$ , Eq. (70a), for  $L = 0, 2$ , and the SU(3) Shannon entropy  $S_{SU3}(L_i)$ , Eq. (70b) for  $L = 0$ , respectively. The range in these quantities is  $0 \leq S_G(L_i) \leq 1$ , with  $S_G(L_i) = 0$  ( $S_G(L_i) > 0$ ) indicating purity (mixing) with respect to  $G = U(5), SU(3)$ . The right-most column displays the values of the SU(3) correlation coefficient  $0 \leq C_{SU3}(0-6) \leq 1$ , Eq. (71), correlating sequences of  $L = 0, 2, 4, 6$  states for each eigenstate  $L = 0_i$  with energy  $E_i$ . The value  $C_{SU3}(0-6) \approx 1$  indicates a highly-correlated sequence, comprising a  $K = 0$  band and manifesting SU(3)-QDS. Slight departures,  $C_{SU3}(0-6) < 1$ , indicate a reduction in the SU(3) coherence.

The intrinsic Hamiltonian in region I of the QPT is  $\hat{H}_1(\rho)$ , Eq. (7a), with  $0 \leq \rho \leq \rho^*$ . For  $\rho = 0$ , it has U(5) DS and a solvable spectrum, Eq. (17). The added collective  $c_5$ -term conforms with the dynamical symmetry, the eigenstates remain the U(5) basis states,  $|N, n_d, \tau, n_\Delta, L\rangle$  Eq. (1a), and hence satisfy  $S_{U5}(L_i) = 0$ . The combined spectrum becomes  $E_i = 2\bar{h}_2[2N - 1 - n_d]n_d + c_5[\tau(\tau + 3) - 4n_d]$ , which explains the observed spreading in the Peres lattice with  $c_5 = 1$  in Fig. 29. The energies of the lowest  $L = \tau = 0$  states still follow the potential curve  $V_1(\rho = 0)$ , Eq. (38). The  $c_6$ -term breaks the U(5) symmetry, inducing considerable  $\Delta n_d = \pm 2$  mixing, but retains the O(5) symmetry and quantum number  $\tau$ . Accordingly, the U(5) Shannon entropies are non-zero, as seen for  $c_6 = 1$  in Fig. 29. Nevertheless, a few low-lying (as well as high-lying) states exhibit a low value of  $S_{U5}(L)$ , indicating the persistence of an (approximate) U(5)-PDS in the presence of the  $O(6)$  term. The energies of the lowest  $L = \tau = 0$  states in the Peres lattice deviate now from  $V_1(\rho = 0)$ . In all cases considered in Fig. 29, with and without the collective terms, the eigenstates in question are spherical in nature, hence exhibit considerable SU(3) mixing ( $S_{SU3}(L = 0) \approx 1$ ) and lack of SU(3) coherence ( $C_{SU3}(0-6) < 1$ ).

For  $\rho > 0$ , the intrinsic Hamiltonian  $\hat{H}_1(\rho)$  itself breaks the U(5) symmetry. Most of its eigenstates are mixed with respect to U(5) except for the U(5)-PDS states of Eq. (20), with  $n_d = \tau = L = 0, 3$ . The U(5)-PDS property still holds when the  $c_5$ -term is included,



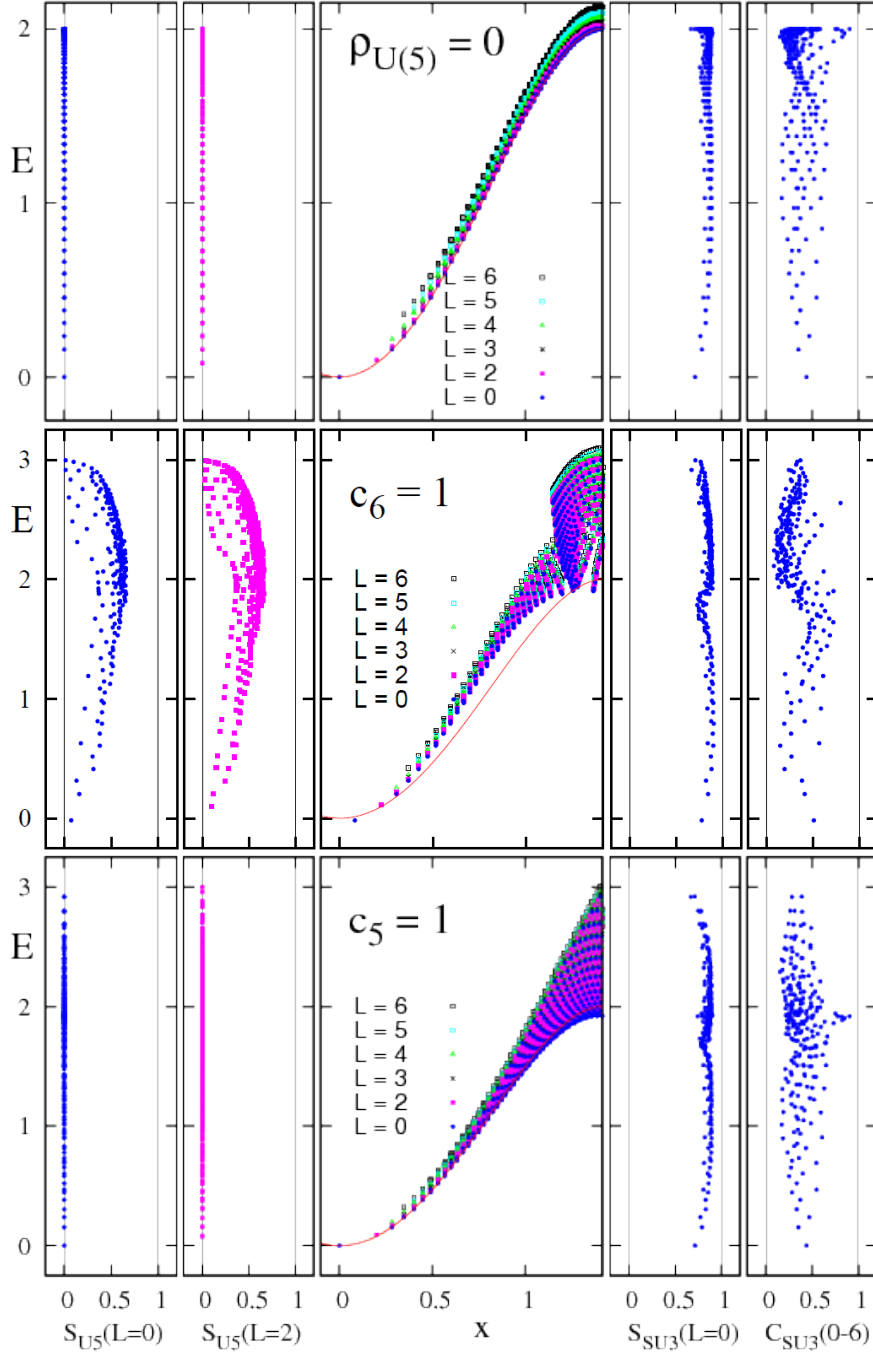


Figure 29:  $U(5)$  Shannon entropy  $S_{U5}(L=0)$  and  $S_{U5}(L=2)$ , Eq. (70a), Peres lattices  $\{x, E_i\}$ , Eq. (66), overlaid on the classical potential,  $SU(3)$  Shannon entropy  $S_{SU3}(L=0)$ , Eq. (70b), and  $SU(3)$  correlation coefficient  $C_{SU3}(0-6)$ , Eq. (71). The  $L = 0, 2, 3, 4, 5, 6$  eigenstates are those of the intrinsic Hamiltonian, Eq. (7), with  $h_2 = 1$ ,  $\beta_0 = \sqrt{2}$ ,  $N = 50$ , at the  $U(5)$  DS limit ( $\rho = 0$ , top row), and of added  $\overline{O}(6)$  ( $c_6 = 1$ , middle row) and  $O(5)$  ( $c_5 = 1$ , bottom row) collective terms, Eq. (6).

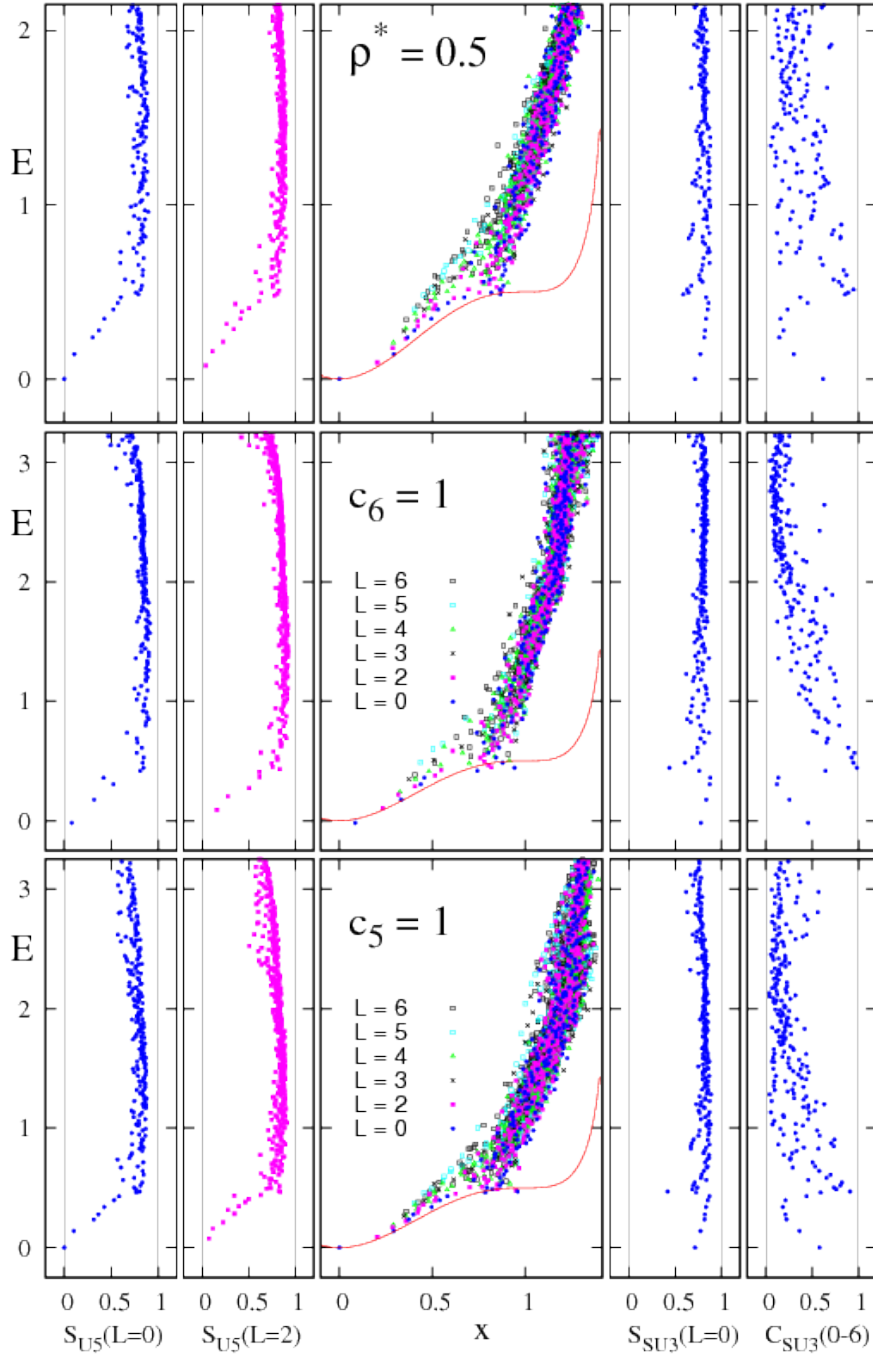


Figure 30: Same as in Fig. 29, but at the spinodal point ( $\rho^* = 1/2$ ).

but is violated by the  $c_6$ -term. This can be seen in Fig. 30 for the spherical ground state,  $L = 0_1$ , which has  $S_{U_5} = 0$  ( $S_{U_5} > 0$ ) for the  $c_5$  ( $c_6$ ) term. In general, the added collective terms maintain the characteristic features of the intrinsic quantum dynamics in region I,

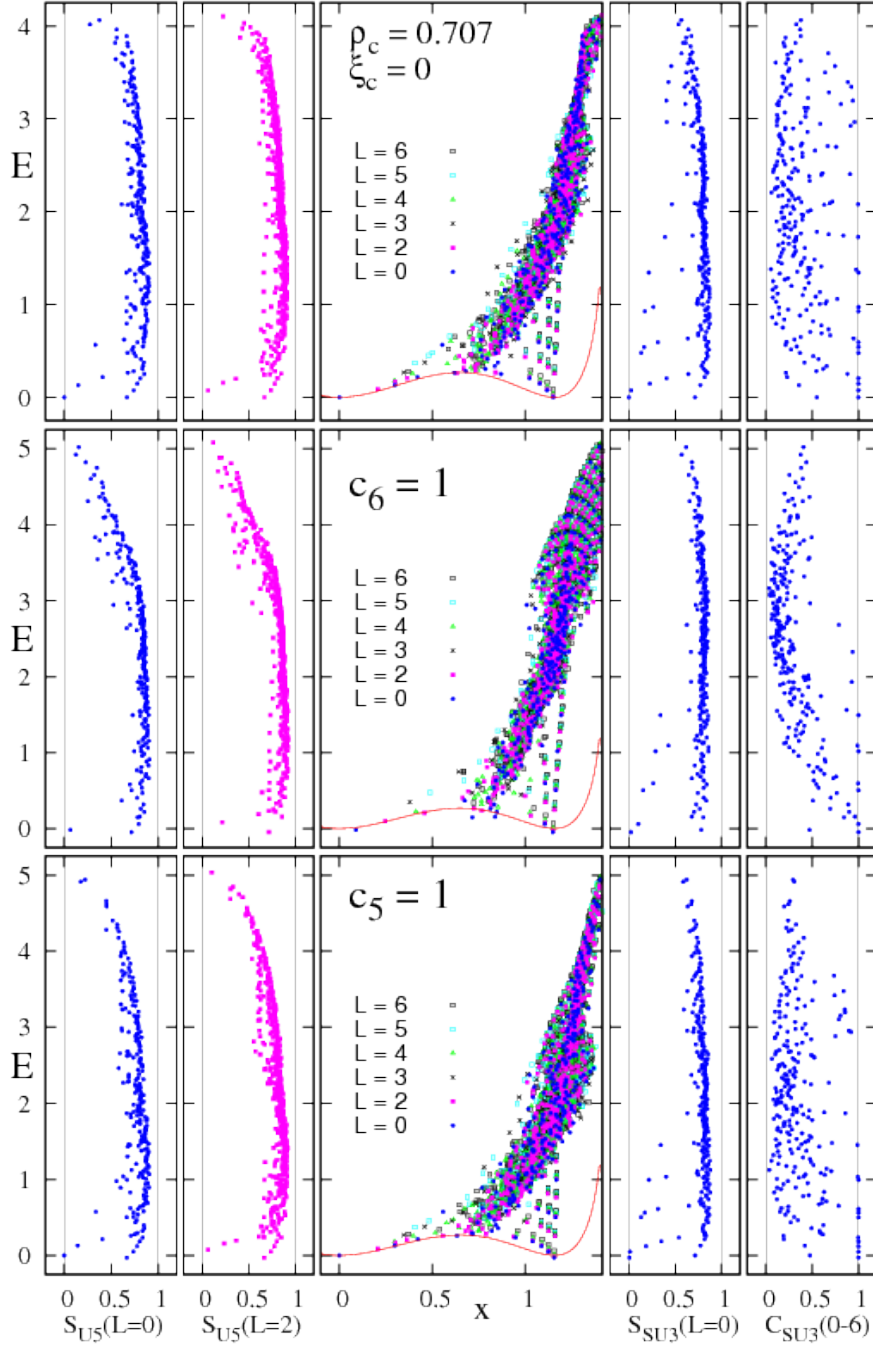


Figure 31: Same as in Fig. 29, but at the critical point ( $\rho_c = 1/\sqrt{2}, \xi_c = 0$ ).

namely, the presence of spherical-type of states at low energy, with an approximate U(5)-PDS, of more complex-type of states at higher energy, and the absence of rotational bands, hence  $S_{\text{SU}_3}(L=0) \approx 1$  and  $C_{\text{SU}_3}(0-6) < 1$  for all states. The quantum dynamics in the spherical region is, to a large extent, determined by the O(5)-breaking  $\rho$ -term in the intrinsic

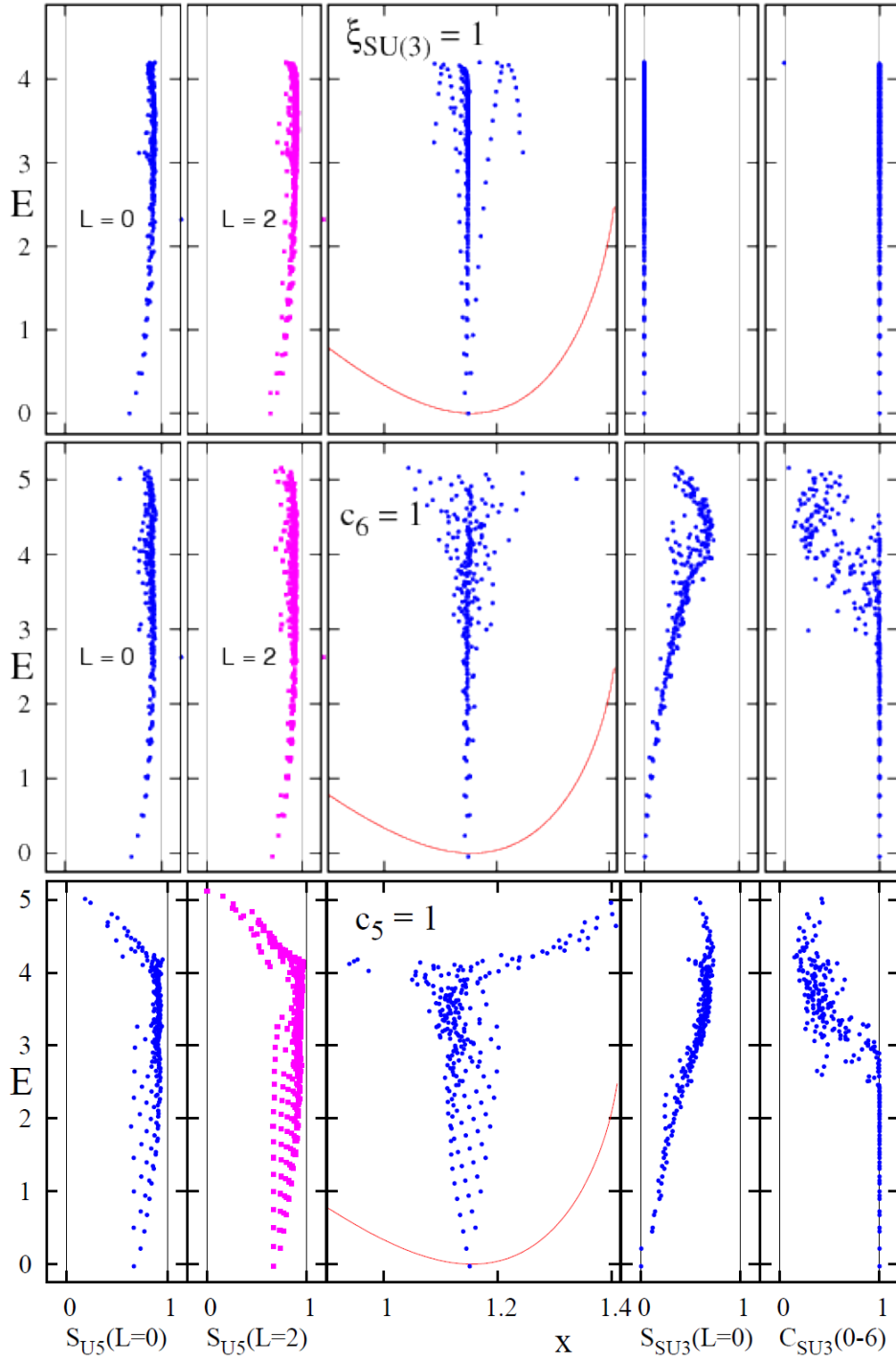


Figure 32: Same as in Fig. 29, but at the SU(3) DS limit ( $\xi = 1$ ).

Hamiltonian, Eq. (19). These observations are exemplified in Fig. 30 by the Peres lattices, Shannon entropies and SU(3) correlator at the spinodal point  $\rho^*$ , and are consistent with the classical analysis of Fig 25, showing the Hénon-Heiles scenario for the onset of chaos in this region.

The intrinsic Hamiltonian in region II is  $\hat{H}_1(\rho)$ , Eq. (7a), with  $\rho^* < \rho \leq \rho_c$ , and  $\hat{H}_2(\xi)$  of Eq. (7b), with  $\xi_c \leq \xi < \xi^{**}$ . As discussed in Section 7, the new element entering the intrinsic quantum dynamics in the shape-coexistence region, is the occurrence of deformed-type of states forming rotational  $K$ -bands, associated with the deformed minimum, coexisting with low-energy spherical-type of states, associated with the spherical minimum, in the background of more-complicated type of states at higher-energies. The regular rotational  $K$ -bands exhibit coherent SU(3) mixing, and for  $K = 0$  bands are signaled by  $C_{\text{SU}(3)}(0-6) \approx 1$ . As shown for the critical point ( $\xi_c = 0$ ) in Fig 31, the inclusion of the collective  $c_5$ -term maintains these features. In contrast, the regular band-structure is disrupted by the inclusion of the  $c_6$ -term. The number of quasi-SU(3) bands for which  $C_{\text{SU}(3)}(0-6) > 0.995$ , is now reduced from 12 to 6. Thus, most of the reduction of SU(3)-QDS is due to the collective  $\overline{O(6)}$  rotations which couple the deformed and spherical configurations and mix strongly the regular and irregular states. This disruption of band-structure is consistent with the  $\beta$ -distortion of the regular island, observed in the classical analysis of Fig. 26. It highlights the importance for QPTs of the coupling of the order parameter fluctuations with soft modes [90].

The intrinsic Hamiltonian in region III is  $\hat{H}_2(\xi)$  of Eq. (7b), with  $\xi \geq \xi^{**}$ . For  $\xi = 1$ , it has SU(3) DS and a solvable spectrum, Eq. (22). The added collective  $c_5$ - and  $c_6$  terms both break the SU(3) symmetry and consequently, as seen in Fig. 32, the SU(3) Shannon entropy in both cases is positive,  $S_{\text{SU}(3)}(L) > 0$ . At low and medium energies, ( $E \leq 3$  for the  $c_5$  term and  $E \leq 4.5$  for  $c_6$  term), the SU(3) mixing is coherent and the  $L$ -states are still arranged in rotational bands. The number of such regular  $K = 0$  bands is smaller for the  $c_5$ -term, consistent with the classical analysis of Fig. 27, showing a more pronounced onset of chaos in the  $\gamma$ -motion due to the O(5) rotational term. At higher energies, the SU(3)-QDS property is dissolved due to mixing with other types of states. In general, there are no spherical-type of states in region III, and the U(5) entropy is positive,  $S_{\text{U}(5)}(L) > 0$ , in all panels of Fig. 32. This is in line with the fact that the classical Landau potential has a single deformed minimum in this region.

## 9. Height of the barrier

All calculations presented so far, were performed at a fixed value of  $\beta_0 = \sqrt{2}$ , ensuring a high barrier  $V_{\text{bar}}/h_2 = 0.268$ , Eq. (52), at the critical point ( $\xi_c = 0$ ). For this choice, the intrinsic Hamiltonian  $\hat{H}_2(\xi; \beta_0 = \sqrt{2})$ , Eq. (24), attains the SU(3) limit for  $\xi = 1$  and exhibits SU(3)-PDS for states in the ground and selected gamma bands of Eq. (25), throughout the deformed region,  $\xi \geq \xi_c$ . A variation of the parameter  $\beta_0$  in the intrinsic Hamiltonian, Eq. (7), affects the symmetry properties of quantum states and the morphology of the classical potential, in particular, the height of the barrier. In the present Section we examine the implied changes in the dynamics in the coexistence region of the QPT, reflecting the impact of different barrier heights.

Focusing the discussion to the intrinsic dynamics at the critical point ( $\rho_c, \xi_c$ ), the Poincaré sections for the classical Hamiltonian  $\mathcal{H}_1(\rho_c) = \mathcal{H}_2(\xi_c)$ , Eq. (26), with  $\beta_0 = 0.35, 1.5, 1.87$ , are displayed in the left, center and right columns of Fig. 33, respectively. The three cases

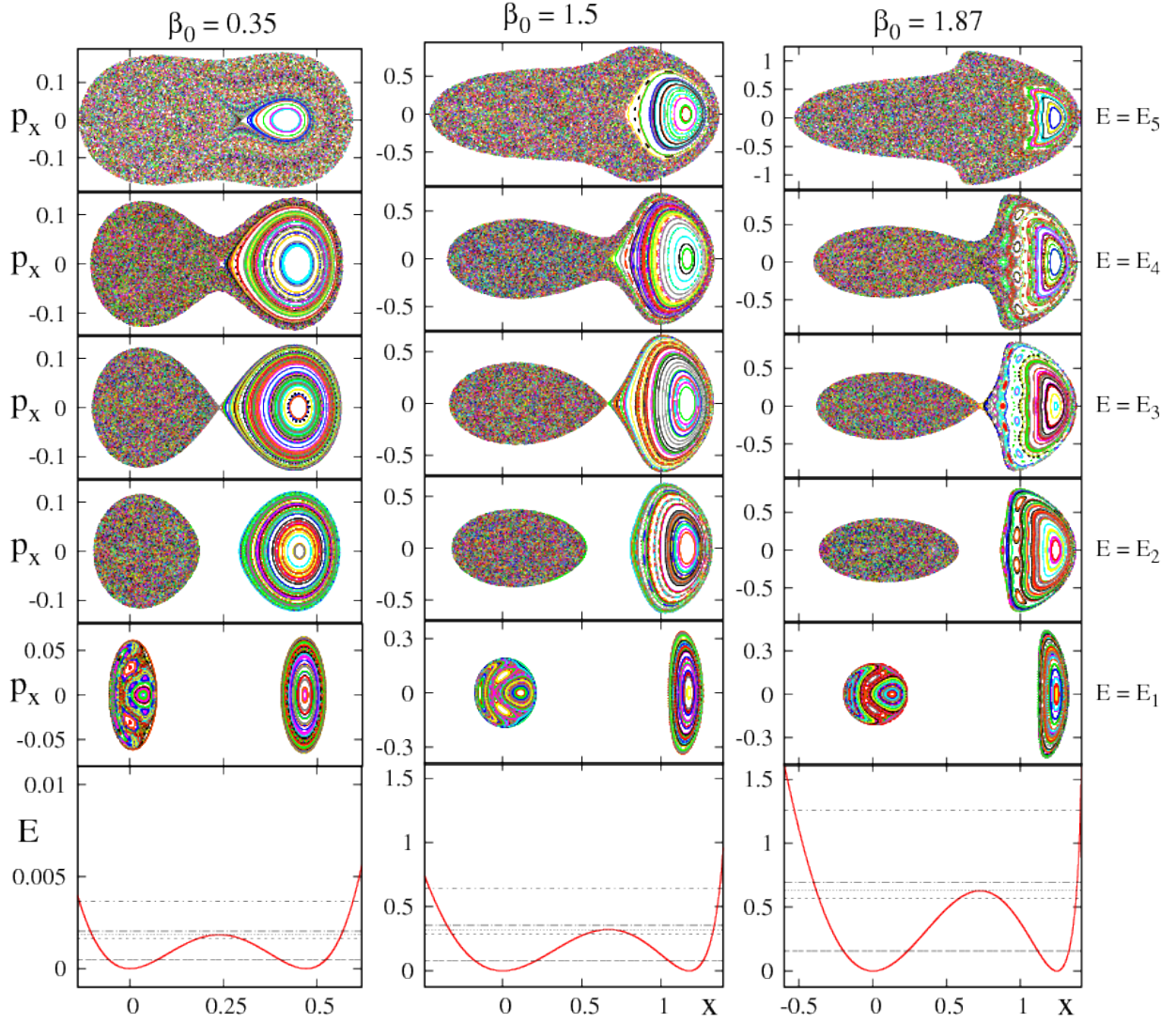


Figure 33: Poincaré sections of critical-point Hamiltonians  $\mathcal{H}_1(\rho_c; \beta_0) = \mathcal{H}_2(\xi_c; \beta_0)$ , Eq. (26), with  $h_2 = 1$  and  $\beta_0 = 0.35, 1.5, 1.87$ , corresponding to different barrier heights  $V_{\text{bar}}/h_2 = 0.0018, 0.322, 1.257$ , respectively. The value at the domain boundary is  $V_{\text{lim}}/h_2 = 2$ . The bottom row displays the corresponding classical potentials  $V_1(\rho_c; x, y = 0) = V_2(\xi_c; x, y = 0)$ , Eq. (31). The five energies at which the sections were calculated consecutively, are indicated by horizontal lines. Note the different vertical and horizontal scales for the panels in the  $\beta_0 = 0.35$  column.

correspond to potential barriers  $V_{\text{bar}}/h_2 = 0.0018, 0.322, 1.257$ , compared to the value at the domain boundary,  $V_{\text{lim}}/h_2 = 2$ . The bottom row depicts the corresponding classical potentials  $V_{\text{cri}}(\beta, \gamma = 0) = V_{\text{cri}}(x, y = 0)$ , Eq. (48). Apart from an energy scale, the three cases display similar trends, namely, a Hénon-Heiles type of transition, with increasing energy, from regular to chaotic motion in the vicinity of the spherical well, and regular dynamics in the vicinity of the deformed well. The extremely low-barrier case displayed in the left column of Fig. 33, is obtained for  $\beta_0 = \frac{1}{2\sqrt{2}}$ , which is the value of the equilibrium

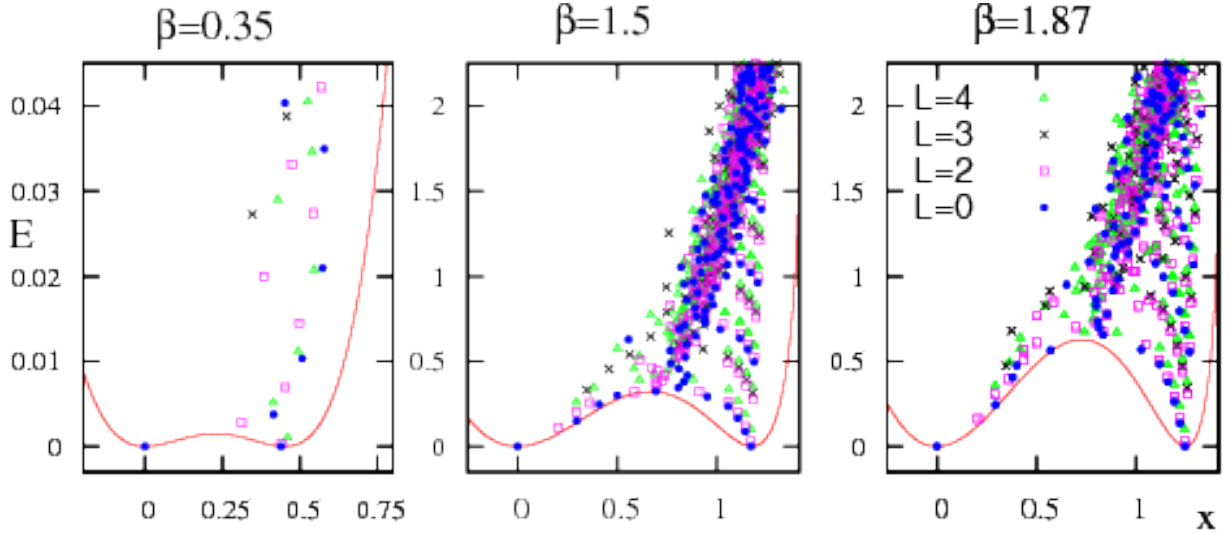


Figure 34: Quantum Peres lattices  $\{x_i, E_i\}$  for  $L = 0$  eigenstates  $|i\rangle$  of  $\hat{H}_{\text{cri}}$  (11), with  $h_2 = 1$ ,  $N = 50$  and  $\beta_0 = 0.35, 1.5, 1.87$ . The lattices are overlaid on the same classical potentials as in Fig. 33, accommodating different barrier heights. Note the different vertical and horizontal scales for the panel with  $\beta_0 = 0.35$ .

deformation for the critical-point Hamiltonian, Eqs. (13)-(14), with  $\chi = -\frac{\sqrt{7}}{2}$ . The small energy scale explains why the simple pattern of coexisting but well-separated regular and chaotic dynamics in the coexistence region, has escaped the attention in all previous works which employed the Hamiltonian of Eq. (13). This highlights the benefits gained by using the intrinsic-collective resolution of the Hamiltonian, Eq. (4), and the ability to construct Hamiltonians accommodating a high-barrier, in order to uncover in a transparent manner the rich dynamics in the coexistence region of the QPT.

In spite of the overall similarity, some differences can be detected between the classical dynamics with  $\beta_0 < 1$  and  $\beta_0 > 1$ . In the former case, the onset of chaos occurs at a lower energy, as demonstrated in Fig. 33. This can be attributed to the different relative weights of the harmonic term,  $\beta_0^2 \beta^2$ , and the chaos-driving term,  $\beta_0 \sqrt{2 - \beta^2} \beta^3 \cos 3\gamma$  in the Landau potential,  $V_{\text{cri}}(\beta, \gamma)$ , Eq. (48). The value of  $\beta_0$  affects also the ratio  $R$  of normal-mode frequencies of oscillations about the deformed minimum, Eq. (59). As noted in Section 5.3, the number of islands in a Poincaré Birkhoff chain is  $2/R$ , hence decreases with  $R \propto (1 + \beta_0^2)$ . Accordingly, the island chains are more visible and the resonance structure is more pronounced for larger values of  $\beta_0$  (see the column for  $\beta_0 = 1.87$  in Fig. 33).

Fig. 34 presents the quantum Peres lattices calculated for ( $N = 50$ ,  $L = 0, 2, 3, 4$ ) eigenstates of the critical-point intrinsic Hamiltonian, Eq. (11), with  $\beta_0 = 0.35, 1.5, 1.87$ , the same values used for the classical Poincaré sections in Fig. 33. In each case, one can clearly identify regular sequences of  $K = 0, 2, 4$  bands localized within and above the respective deformed wells, and persisting to energies well above the barriers. The number of such  $K$ -bands is larger when the potential is deeper (larger  $\beta_0$  values). To the left of the barrier towards the spherical minimum, one observes a number of low-energy U(5)-like multiplets, Eq. (18). This spherical multiplet-structure is very pronounced for  $\beta_0 = 1.5, 1.87$  (high barriers) and only part of it survives for  $\beta_0 = 0.35$  (extremely low barrier).



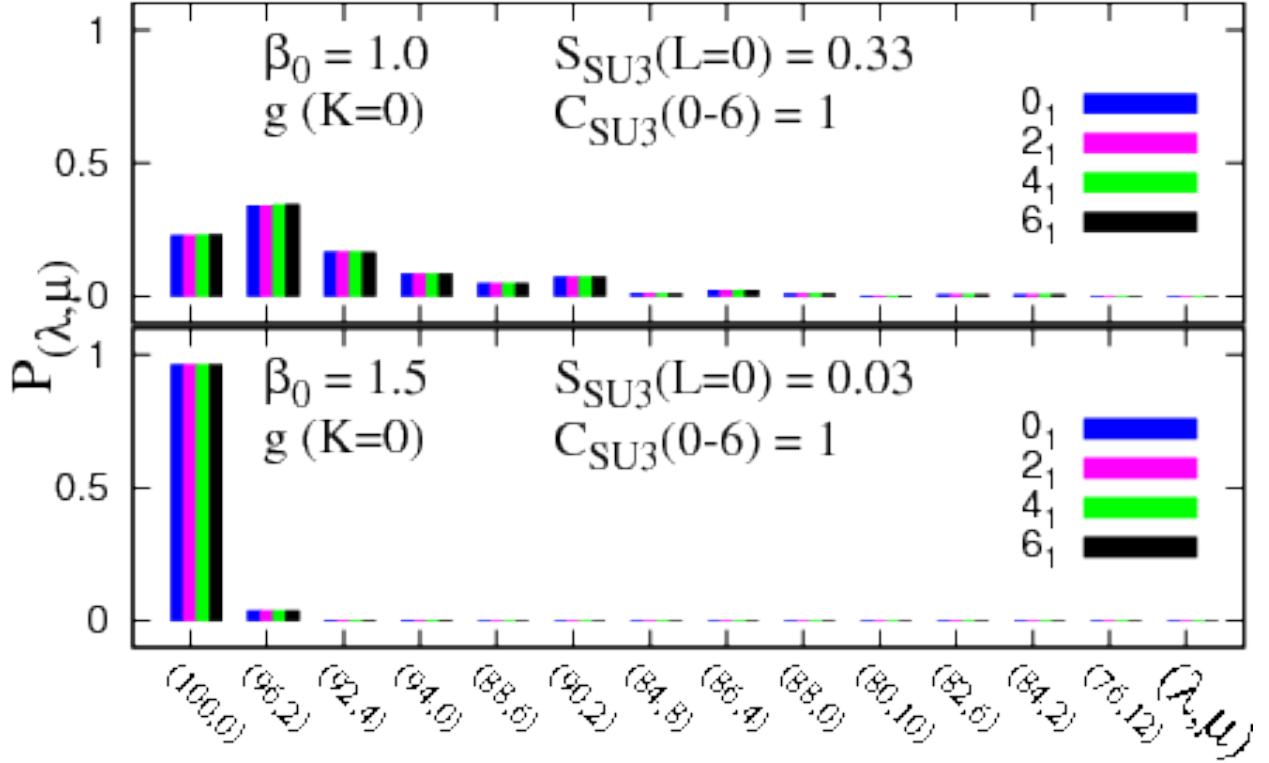


Figure 35: SU(3) probability distribution  $P_{\lambda, \mu}^{(L)}$ , Eq. (69b), for  $(N = 50, L = 0, 2, 4, 6)$  states, members of the ground band of the intrinsic critical-point Hamiltonian  $\hat{H}_1(\rho_c; \beta_0) = \hat{H}_2(\xi_c; \beta_0)$ , Eq. (7), with  $\beta_0 = 1$  (top) and  $\beta_0 = 1.5$  (bottom). Each panel lists the SU(3) Shannon entropy  $S_{\text{SU3}}(L = 0)$ , Eq.(70b), and the SU(3) correlator  $C_{\text{SU3}}(0-6)$ , Eq. (71), indicating the extent of SU(3) mixing and coherence, respectively.

For  $\beta_0 \neq \sqrt{2}$ , the intrinsic Hamiltonian,  $\hat{H}_2(\xi; \beta_0)$ , Eq. (7b), no longer possess the SU(3) PDS property, Eq. (25). All eigenstates are mixed with respect to SU(3), including member states of the ground and gamma bands. Nevertheless, by construction,  $\hat{H}_2(\xi; \beta_0)$  still satisfies Eq. (5), and hence the states with  $L = 0, 2, 4, \dots, 2N$ , projected from the condensate, Eq. (3), with  $[\beta_{\text{eq}} = \sqrt{2}\beta_0(1 + \beta_0^2)^{-1/2}, \gamma_{\text{eq}} = 0]$ , span a solvable (but SU(3)-mixed) ground band. In general, the SU(3) mixing is stronger for larger deviations,  $|\beta_0 - \sqrt{2}|$ , and the mixing is coherent for the  $L$ -states in the same  $K$ -band. This is illustrated in Fig. 35, which shows the SU(3) decomposition in the solvable ground band of the critical-point intrinsic Hamiltonian  $\hat{H}_2(\xi_c; \beta_0)$ , for two values of  $\beta_0$ . For  $\beta_0 = 1$ , the  $L = 0$  bandhead state of the ground band has a high-value for the SU(3) Shannon entropy,  $S_{\text{SU3}}(L = 0) = 0.33$ , hence is less pure compared to its counterpart with  $\beta_0 = 1.5$ , for which  $S_{\text{SU3}}(L = 0) = 0.03$ . In both cases, the ground bands exhibit SU(3) coherence ( $L$ -independent mixing), with SU(3) correlation coefficients  $C_{\text{SU3}}(0-6) = 1$ , exemplifying SU(3)-QDS.



## 10. Summary and conclusions

We have presented a comprehensive analysis of the dynamics evolving across a generic (high-barrier) first-order QPT, with particular emphasis on aspects of chaos, regularity, and symmetry. The study was conducted in the framework of the IBM, a prototype of an algebraic model, whose phases are associated with dynamical symmetries (DSs) and the transition between them exemplify QPTs in an interacting many-body system. The specific model Hamiltonian employed, describes a shape-phase transition between spherical [U(5) DS] and deformed [SU(3) DS] quadrupole shapes, a situation encountered in nuclei. The resolution of the Hamiltonian into intrinsic (vibrational) and collective (rotational) parts has allowed us to disentangle the effects due to terms affecting the Landau potential, from effects due to kinetic terms. The separate treatment of the intrinsic dynamics highlights simple features by avoiding distortions that may arise in the presence of large rotation-vibration coupling. The availability of IBM Hamiltonians accommodating a high barrier in a wide range of control parameters, made it possible to uncover a previously unrecognized pattern of competing order and chaos, which echoes the QPT in the coexistence region.

A classical analysis of the intrinsic part of the Hamiltonian revealed a rich mixed dynamics with distinct features in each structural region of the QPT. On the spherical side of the QPT, the system is integrable at the U(5) DS limit. Near it, the phase space portrait resembles that of a weakly perturbed anharmonic (quartic) oscillator. In other parts of region I, where the Landau potential has a single spherical minimum, the phase space portrait is similar to the Hénon-Heiles system, with regular dynamics at low energy and chaos at higher energy. The non-integrability here is due to the O(5)-breaking term in the Hamiltonian. On the deformed side of the QPT, the system is integrable at the SU(3) DS limit. Away from it, the integrability is lost by a different mechanism of breaking the SU(3) symmetry. The dynamics, however, remains robustly regular throughout region III, where the Landau potential supports a single deformed minimum. The Poincaré sections in this region are dominated by regular trajectories forming a single island. Additional chains of regular islands show up, occasionally, due to resonances in the normal-mode oscillations. The fact that the classical dynamics evolves differently, is attributed to the different topology of the Landau potential in the vicinity of the two minima. In spite of the abrupt structural changes taking place, the dynamics in the phase coexistence region (region II), exhibits a very simple pattern where each minimum preserves, to a large extent, its own characteristic dynamics. The robustly ordered motion is still confined to the deformed minimum, in marked separation from the chaotic behavior ascribed to the spherical minimum. The coexistence of well-separated order and chaos persists in a broad energy range, even above the barrier, throughout region II, and is absent outside it. The simple pattern of mixed dynamics thus traces the crossing of the two minima, a defining feature of a first-order QPT. Simply divided phase spaces are known to occur in billiard systems [91, 92], where the amount of chaoticity in the motion of a free particle is governed by the geometry of the cavity. Here, however, they show up in a many-body interacting system undergoing a QPT, where the onset of chaos is governed by a variation of coupling constants in the Hamiltonian.

The quantum manifestations of the classical inhomogeneous phase space structure have

been analyzed via Peres lattices. The latter distinguish regular from irregular quantum states by means of ordered and disordered meshes of points. A choice of Peres operator whose classical limit corresponds to the deformation, allowed us to overlay the lattices on the classical potentials and thus associate the indicated states with a given region in phase space. The results obtained reflect adequately the mixed nature of the classical dynamics. The distribution of lattice points agrees with the location of regular and chaotic domains in the classical Poincaré sections. The quantum analysis has disclosed a number of regular low-energy spherical-vibrator U(5)-like multiplets, associated with the spherical minimum and regular SU(3)-like rotational  $K$ -bands in the vicinity of the deformed minimum. The latter bands persist to energies well above the barrier, extend to high values of angular momenta, and their number is larger for deeper deformed wells. These two kinds of regular subsets of states retain their identity amidst a complicated environment of other states, and both are present in the coexistence region.

An important clue on the nature of the surviving regular sequences of selected states, comes from a symmetry analysis of their wave functions. A U(5) decomposition has shown that the above mentioned regular U(5)-like multiplets consist of spherical type of states, with wave functions dominated by a single  $n_d$  component. As such, they exhibit U(5) partial dynamical symmetry [U(5)-PDS], either exactly or to a good approximation. This enhanced U(5) purity is signaled by a low value of the U(5) Shannon entropy, Eq. (70a). In contrast, the deformed type of states exhibit a broad  $n_d$ -distribution. An SU(3) decomposition of the states in the regular  $K$ -bands shows a coherent ( $L$ -independent) SU(3) mixing, exemplifying SU(3) quasi-dynamical symmetry [SU(3)-QDS]. This pronounced coherence is signaled by a high value of the Pearson-based SU(3) correlation coefficient, Eq. (71). The persisting regular U(5)-like [SU(3)-like] multiplets reflect the geometry of the Landau potential, as they are associated with the different spherical (deformed) minimum. Accordingly, their total number  $\nu_{U5}$  ( $\nu_{SU3}$ ) can be used both as a global measure of the U(5)-PDS [SU(3)-PDS] present in the system, and as a mirror which captures the structural evolution of the first-order QPT. This is demonstrated in Fig. 23, showing the change in these quantities as a function of the control parameters ( $\rho, \xi$ ). The quantity  $\nu_{U5}$  ( $\nu_{SU3}$ ) is maximal at the U(5)-DS [SU(3)-DS] limit and vanishes towards the anti-spinodal (spinodal) point, where the spherical (deformed) minimum disappears.

The collective part of the Hamiltonian consists of kinetic terms associated with O(3), O(5) and  $\overline{O(6)}$  rotations. When added to the intrinsic part of the Hamiltonian they lead to rotational splitting and mixing. Although these kinetic terms do not affect the Landau potential, the mixing induced by the O(5) and  $\overline{O(6)}$  terms, can affect the onset of classical chaos and the regular features of quantum states. An analysis of the classical and quantum dynamics has shown that in region I, the added collective terms being O(5)-invariant, maintain the Hénon-Heiles type of dynamics; the onset of chaos being largely determined by the intrinsic Hamiltonian. The  $\overline{O(6)}$  rotational term, being associated with the  $\beta$  degree of freedom, was found to be significant in the coexistence region. Its presence disrupts the regular  $K$ -bands built on the deformed minimum and reduces their coherence property related to SU(3)-QDS. The simple pattern of well-separated regular and chaotic dynamics ascribed to each minimum, however, is not destroyed. The O(5) rotational term, being associated with

the  $\gamma$  degree of freedom, was found to be significant in region III. Its presence modifies the regular intrinsic dynamics associated with the single deformed minimum and leads to significant chaoticity. The SU(3)-QDS property here is completely dissolved at higher energies. It is important to note that chaos can develop from purely kinetic perturbations, without a change in the Landau potential, as vividly demonstrated in Fig. 27. This illustrates that a criterion for the onset of chaos cannot be based solely on the geometry of the potential.

The study of first-order QPTs conducted in this work, considered a finite system, whose mean-field potential involved two asymmetric wells, one dominated by chaotic dynamics the other by regular dynamics. A parameter  $\beta_0$  in the Hamiltonian governed the height of the barrier between them. The ramifications of divided phase space and Hilbert space structure, *e.g.*, simple patterns of dynamics and intermediate symmetries (PDS and QDS), are observed at any  $\beta_0 > 0$ , but are more pronounced for higher barriers (larger  $\beta_0$ ). It will be interesting to see in future studies of first-order QPTs, whether simply divided spaces occur also when both wells accommodate regular or chaotic motion but with distinct characteristic features, *e.g.*, different phase space portraits and dissimilar symmetry structure. Other issues which deserve further attention are finite-size effects and scaling behavior. Although there are initial indications that the simple pattern of mixed dynamics characterizing the QPT, occurs also at moderate values of  $N$ , a systematic study is called for. The large- $N$  scaling behavior should be considered, in analogy to what has been done in second-order (continuous) QPTs. An interesting question to address is whether the global measures of U(5)-PDS and SU(3)-QDS,  $\nu_{U5}$  and  $\nu_{SU3}$ , shown in Fig. 23, converge to a particular curve for large  $N$ .

Returning to the key questions posed in the Introduction, we end with some pertinent remarks. Based on the results obtained in the present paper, we conclude that the interplay of order and chaos accompanying the first-order QPT can reflect its evolution, provided the underlying phase-space is simply divided and each minimum maintains its own characteristic dynamics. If these conditions are met, then the resulting simple pattern of mixed dynamics can trace the modifications in the topology of the Landau potential inside the coexistence region. The pattern of mixed but well-separated dynamics is particularly transparent when considering the intrinsic dynamics, and appears to be robust. Deviations are largely due to kinetic collective rotational terms, which may lead to strong rotation-vibration coupling, breakdown of adiabaticity and an onset of chaos due to purely kinetic perturbations. The present work suggests that the remaining regularity in the system, associated with different minima at the classical level, and with different regular subsets of eigenstates, at the quantum level, amidst a complicated environment, can be assigned particular intermediate symmetries, PDS or QDS. Both the classical and quantum analysis indicate a tendency of a system undergoing a QPT, to retain some “local” regularity far away from integrable limits and some partial- or quasi form of symmetries far way from symmetry limits. Is this linkage between persisting regularities and persisting symmetries a general result or an observation valid for specific algebraic models? What are the general conditions for a dynamical system to have these local regions of regularities and effective symmetries for subsets of states? Can one incorporate the notions of quasi- and partial dynamical symmetries in attempts [93, 94, 95] to formulate quantum analogs of the KAM and Poincaré-Birkhoff

theorems? Quantum phase transitions in many-body systems and their algebraic modeling provide a fertile ground for addressing these deep questions. The present work is only a first step towards accomplishing this goal.

## Acknowledgments

This work is supported by the Israel Science Foundation Grant No. 493/12. M.M. acknowledges the Golda Meir Fellowship Fund, the Czech Science Foundation (P203-13-07117S) and the partial support by U.S. Department of Energy Grant No. DE-FG-02-91ER-40608.

## Appendix A: the IBM potential surface

The normal-order form of the most general IBM Hamiltonian with one- and two-body interactions is given by

$$\begin{aligned} \hat{H}_{IBM} = & \epsilon_s s^\dagger s + \epsilon_d d^\dagger \cdot \tilde{d} + u_0 (s^\dagger)^2 s^2 + u_2 s^\dagger d^\dagger \cdot \tilde{d} s + v_0 \left[ (s^\dagger)^2 \tilde{d} \cdot \tilde{d} + H.c. \right] \\ & + v_2 \left[ s^\dagger d^\dagger \cdot (\tilde{d}\tilde{d})^{(2)} + H.c. \right] + \sum_{L=0,2,4} c_L (d^\dagger d^\dagger)^{(L)} \cdot (\tilde{d}\tilde{d})^{(L)}, \end{aligned} \quad (76)$$

where *H.c.* means Hermitian conjugate. As noted in Section 2, a potential surface  $V(\beta, \gamma)$ , Eq. (2), is obtained by the expectation value of the Hamiltonian in an intrinsic state  $|\beta, \gamma; N\rangle$ , Eq. (3), where  $(\beta, \gamma)$  are quadrupole shape variables. For the general IBM Hamiltonian (76) the surface reads

$$V(\beta, \gamma) = N(N-1) \left\{ E_0 + \frac{1}{2}\beta^2 \left[ a - b\frac{1}{2}\beta\sqrt{2-\beta^2} \cos 3\gamma + (c-a)\frac{1}{2}\beta^2 \right] \right\}. \quad (77)$$

The coefficients  $E_0, a, b, c$ , involve particular linear combinations of the Hamiltonian's parameters [53]

$$\begin{aligned} a = u_2 + 2v_0 - 2u_0 + \bar{\epsilon}, \quad b = 2\sqrt{\frac{2}{7}}v_2, \quad c = \frac{1}{5}c_0 + \frac{2}{7}c_2 + \frac{18}{35}c_4 + \bar{\epsilon}, \quad E_0 = u_0 + \bar{\epsilon}_s, \\ \bar{\epsilon} = \bar{\epsilon}_d - \bar{\epsilon}_s, \quad \bar{\epsilon}_i = \epsilon_i/(N-1). \end{aligned} \quad (78)$$

In analyzing properties of the IBM potential surface, it is convenient to use a different parameterization,  $\tilde{\beta}$ , instead of  $\beta$ , where the two variables are related by Eq. (39). The intrinsic state in the new parameterization reads [60, 61]

$$|\tilde{\beta}, \gamma; N\rangle = (N!)^{-1/2} [\Gamma_c^\dagger(\tilde{\beta}, \gamma)]^N |0\rangle, \quad (79a)$$

$$\Gamma_c^\dagger(\tilde{\beta}, \gamma) = (1 + \tilde{\beta}^2)^{-1/2} \left[ \tilde{\beta} \cos \gamma d_0^\dagger + \tilde{\beta} \sin \gamma (d_2^\dagger + d_{-2}^\dagger) / \sqrt{2} + s^\dagger \right], \quad (79b)$$

and the potential surface has the form

$$V(\tilde{\beta}, \gamma) = N(N-1) [E_0 + f(\tilde{\beta}, \gamma)], \quad (80a)$$

$$f(\tilde{\beta}, \gamma) = (1 + \tilde{\beta}^2)^{-2} \tilde{\beta}^2 \left[ a - b\tilde{\beta} \cos 3\gamma + c\tilde{\beta}^2 \right]. \quad (80b)$$

The extremum equations,  $\partial V/\partial\tilde{\beta} = \partial V/\partial\gamma = 0$ , always have  $\tilde{\beta} = 0$  as a solution. It is a local minimum for  $a > 0$  and a global minimum if in addition,  $c - b^2/4a > 0$ . For  $b \neq 0$ , a deformed extremum ( $\tilde{\beta}^* \neq 0, \gamma^*$ ), has  $\gamma^* = 0$  (prolate) or  $\gamma^* = \pi/3$  (oblate),  $\text{mod}(2\pi/3)$ . For  $\gamma = 0$ ,  $\tilde{\beta}^* \neq 0$  is a real solution of the following equation

$$2a - 3b\tilde{\beta} + 2(2c - a)\tilde{\beta}^2 + b\tilde{\beta}^3 = 0 . \quad (81)$$

For  $\gamma = \pi/3$ , the sign of  $b$  in Eq. (81) is reversed. This equation has one real root for  $D > 0$ ; all roots real and unequal for  $D < 0$ ; and all roots real and at least two are equal for  $D = 0$ , where

$$D = -(1 + \zeta^2)^3 + \left(\frac{3}{2}\zeta + \zeta^3 + \frac{a}{b}\right)^2 , \quad \zeta = \frac{2(2c - a)}{3b} . \quad (82)$$

In a local minimum,  $\gamma^* = 0$  ( $\pi/3$ ) for  $b > 0$  ( $b < 0$ ) and  $b\tilde{\beta}_*(3 + \tilde{\beta}_*^2) - 4a > 0$ . In a global minimum,  $b\tilde{\beta}_* - 2a > 0$ .

Given an Hamiltonian  $\hat{H}(\lambda)$  describing a QPT, its potential surface coefficients,  $a(\lambda)$ ,  $b(\lambda)$  and  $c(\lambda)$ , Eq. (78), depend on the control parameter  $\lambda$ . In case of a first-order QPT between a spherical and prolate-deformed shape, the value of the control parameter at the critical point ( $\lambda_c$ ), which defines the critical-point Hamiltonian  $\hat{H}(\lambda_c)$ , is determined by the condition

$$b^2 = 4ac , \quad a > 0 , \quad b > 0 , \quad f(\tilde{\beta}, \gamma = 0) = c(1 + \tilde{\beta}^2)^{-2}\tilde{\beta}^2 (\tilde{\beta} - \bar{\beta})^2 . \quad (83)$$

The corresponding potential surface shown, has degenerate spherical and deformed minima at  $\tilde{\beta} = 0$  and  $(\tilde{\beta} = \bar{\beta}, \gamma = 0)$ , where  $\bar{\beta} = 2a/b$ . The value of the control parameter at the spinodal point ( $\lambda^*$ ), where the deformed minimum disappears, is obtained by requiring  $D = 0$ , with  $D$  given in Eq. (82). The value of the control parameter at the anti-spinodal point ( $\lambda^{**}$ ), where the spherical minimum disappears, is obtained by requiring  $a = 0$ .

The potential surface coefficients for the first-order intrinsic Hamiltonian of Eq. (7), are given by

$$\hat{H}_1(\rho)/\bar{h}_2 : \quad a = 2\beta_0^2 , \quad b = 4\beta_0^2\rho , \quad c = 2 , \quad E_0 = 0 , \quad (84a)$$

$$\hat{H}_2(\xi)/\bar{h}_2 : \quad a = 2\beta_0^2[1 - \xi(1 + \beta_0^2)] , \quad b = 4\beta_0 , \quad c = 2 + \xi(1 - \beta_0^2) , \quad E_0 = \xi\beta_0^4 . \quad (84b)$$

The values of the control parameters at the critical ( $\rho_c, \xi_c$ ), spinodal ( $\rho^*$ ), and anti-spinodal ( $\xi^{**}$ ) points, given in Eqs. (33)-(35), were obtained by the conditions mentioned above. The energy surface coefficients of the collective Hamiltonian, Eq. (6), all vanish.

## Appendix B: Linear correlation coefficients

The extent to which two  $n$ -dimensional vectors,  $X$  and  $Y$ , with components  $X_m$  and  $Y_m$  respectively, support a linear relation, can be measured by the standard Pearson correlation coefficient, defined as

$$\pi(X, Y) = \frac{1}{n-1} \sum_{m=1}^n \frac{(X_m - \bar{X})}{s_X} \frac{(Y_m - \bar{Y})}{s_Y} . \quad (85)$$

Here  $\bar{X}$ ,  $\bar{Y}$  and  $s_X$ ,  $s_Y$  are the mean values and standard deviations of the vector components, respectively. The values of the Pearson coefficient lie in the range  $-1 \leq \pi(X, Y) \leq 1$ , with  $\pi(X, Y) = 1$ ,  $\pi(X, Y) = -1$ , and  $\pi(X, Y) = 0$  indicate a perfect correlation, perfect anti-correlation and no linear correlation, respectively.

In the present work, we apply the Pearson indicator to estimate the amount of correlations between two eigenstates of an IBM Hamiltonian,  $|L_i\rangle$  and  $|L'_j\rangle$ . For that purpose, we expand both states in the SU(3) basis as in Eq. (68), and identify their SU(3) probability distributions  $P_{(\lambda,\mu)}^{(L_i)}$  and  $P_{(\lambda,\mu)}^{(L'_j)}$ , Eq. (69b), with the components of the vectors  $X_m$  and  $Y_m$  in Eq. (85). To ensure an equal number of components, we assign a value zero to the component,  $P_{(\lambda,\mu)}^{(L'_j)} = 0$ , if the angular momentum  $L'$  is not contained in a particular SU(3) irrep  $(\lambda, \mu)$  that does accommodate the angular momentum  $L$ . To associate a band of states with a given state  $|L_i\rangle$ , we scan the entire spectrum of states  $|L'_j\rangle$ , with angular momentum  $L' \neq L$ , and choose the state that maximizes the Pearson correlation coefficient  $\max_j \{\pi(L_i, L'_j)\}$ , Eq. (85). This identifies among the ensemble of states with angular momentum  $L'$ , the most correlated state with  $|L_i\rangle$ , which is the favored candidate to be its member in the same band. This procedure, adapted from [81], was used in Eq. (71) to identify  $K = 0$  bands, composed of sequences of rotational states with  $L = 2, 4, 6$ , built on a given  $|L = 0_i\rangle$  bandhead state.

## References

- [1] J.A. Hertz, Phys. Rev. B 14 (1976) 1165.
- [2] R. Gilmore and D.H. Feng, Nucl. Phys. A 301 (1978) 189.
- [3] R. Gilmore, J. Math. Phys. 20 (1979) 891.
- [4] *Understanding Quantum Phase Transitions*, edited by L. Carr, CRC press (2010).
- [5] S. Sachdev, *Quantum Phase Transitions* (Cambridge University Press, Cambridge, 1999).
- [6] M. Greiner, O. Mandel, T. Esslinger, T. W. Hänsch, and I. Bloch, Nature 415 (2002) 39.
- [7] K. Baumann, C. Guerlin, F. Brennecke and T. Esslinger, Nature 464 (2010) 1301.
- [8] P. Cejnar, J. Jolie and R. F. Casten, Rev. Mod. Phys. 82 (2010) 2155.
- [9] M.C. Gutzwiller, *Chaos in Classical and Quantum Mechanics* (Springer, New York, 1990).
- [10] L. E. Reichl, *The Transition to Chaos in Conservative Classical Systems: Quantum Manifestations* (Springer-Verlag, New York, 1992).
- [11] A.J. Lichtenberg and M.A. Lieberman, *Regular and Chaotic Dynamics* (Springer-Verlag, New York, 1992).
- [12] C. Emary and T. Brandes, Phys. Rev. Lett. 90 (2003) 044101.
- [13] C. Emary and T. Brandes, Phys. Rev. E 67 (2003) 066203.
- [14] C.A. Marianetti, G. Kotliar and G. Ceder, Nature Mater. 3 (2004) 627.
- [15] C. Pfleiderer, J. Phys.: Condens. Matter 17 (2005) S987.
- [16] C. Pfleiderer, Rev. Mod. Phys. 81 (2009) 1551.
- [17] B. Karmakar, V. Pellegrini, A. Pinczuk, L.N. Pfeiffer, and K.W. West, Phys. Rev. Lett. 102 (2009) 036802.
- [18] N. T. Phuc, Y. Kawaguchi, and M. Ueda, Phys. Rev. A 88 (2013) 043629.
- [19] G. Bertaina, E. Fratini, S. Giorgini, and P. Pieri, Phys. Rev. Lett. 110 (2013) 115303.
- [20] A.P. Young, S. Knysh, and V.N. Smelyanskiy, Phys. Rev. Lett. 104 (2010) 020502.
- [21] F. Iachello and A. Arima, *The Interacting Boson Model* (Cambridge Univ. Press, Cambridge, 1987).
- [22] F. Iachello and R.D. Levine, *Algebraic Theory of Molecules*, (Oxford Univ. Press, Oxford, 1994).
- [23] R. Bijker, F. Iachello and A. Leviatan, Ann. Phys., NY 236 (1994) 69.

- [24] P. Cejnar and J. Jolie, Prog. Part. Nucl. Phys. 62 (2009) 210.
- [25] F. Iachello, Rivista Del Nuovo Cimento 34 (2011) 617.
- [26] R.F. Casten, Prog. Part. Nucl. Phys. 62 (2009) 183.
- [27] R.F. Casten and E.M. McCutchan, J. Phys. G 34 (2007) R285.
- [28] F. Iachello, Phys. Rev. Lett. 85 (2000) 3580.
- [29] F. Iachello, Phys. Rev. Lett. 87 (2001) 052502.
- [30] D.J. Rowe, Phys. Rev. Lett. 93 (2004) 122502.
- [31] D.J. Rowe, Nucl. Phys. A 745 (2004) 47.
- [32] G. Rosensteel and D.J. Rowe, Nucl. Phys. A 759 (2005) 92.
- [33] A. Leviatan, Phys. Rev. Lett. 98 (2007) 242502.
- [34] A. Leviatan and J.N. Ginocchio, Phys. Rev. Lett. 90 (2003) 212501.
- [35] F. Iachello and N.V. Zamfir, Phys. Rev. Lett. 92 (2004) 212501.
- [36] A. Leviatan, Phys. Rev. C 72 (2005) 031305(R).
- [37] A. Leviatan, Phys. Rev. C 74 (2006) 051301(R).
- [38] J.M. Arias, J. Dukelsky, J.E. García-Ramos, and J. Vidal, Phys. Rev. C 75 (2007) 014301.
- [39] D.J. Rowe, P.S. Turner and G. Rosensteel, Phys. Rev. Lett. 93 (2004) 232502.
- [40] S. Dusuel, J. Vidal, J.M. Arias, J. Dukelsky and J.E. García-Ramos, Phys. Rev. C 72 (2005) 011301(R).
- [41] E. Williams, R.J. Casperson and V. Werner, Phys. Rev. C 81 (2010) 054306.
- [42] M.A. Caprio, P. Cejnar and F. Iachello, Ann. Phys. (N.Y.) 323 (2008) 1106.
- [43] D. Petrellis, A. Leviatan and F. Iachello, Ann. Phys. NY 326 (2011) 926.
- [44] Y. Alhassid, A. Novoselsky and N. Whelan, Phys. Rev. Lett. 65 (1990) 2971.
- [45] Y. Alhassid and N. Whelan, Phys. Rev. C 43 (1991) 2637.
- [46] Y. Alhassid and N. Whelan, Phys. Rev. Lett. 67 (1991) 816.
- [47] Y. Alhassid, A. Novoselsky and N. Whelan, Phys. Rev. C 45 (1992) 1677.
- [48] N. Whelan and Y. Alhassid, Nucl. Phys. A 556 (1993) 42.
- [49] S. Heinze, P. Cejnar, J. Jolie and M. Macek Phys. Rev. C 73 (2006) 014306.
- [50] M. Macek, P. Cejnar, J. Jolie and S. Heinze, Phys. Rev. C 73 (2006) 014307.
- [51] M. Macek, P. Stránský, P. Cejnar, S. Heinze, J. Jolie and J. Dobeš, Phys. Rev. C 75 (2007) 064318.
- [52] M.W. Kirson and A. Leviatan, Phys. Rev. Lett. 55 (1985) 2846.
- [53] A. Leviatan, Ann. Phys., NY 179 (1987) 201.
- [54] M. Macek and A. Leviatan, Phys. Rev. C 84 (2011) 041302(R).
- [55] A. Leviatan and M. Macek, Phys. Lett. B 714 (2012) 110.
- [56] A. Arima and F. Iachello, Ann. Phys., NY 99 (1976) 253.
- [57] A. Arima and F. Iachello, Ann. Phys., NY 111 (1978) 201.
- [58] A. Arima and F. Iachello, Ann. Phys., NY 123 (1979) 468.
- [59] A. Bohr and B. R. Mottelson, *Nuclear Structure, Vol. II*. (W. A. Benjamin Publishers, Reading, 1975).
- [60] J. N. Ginocchio and M. W. Kirson, Phys. Rev. Lett. 44 (1980) 1744.
- [61] A.E.L. Dieperink, O. Scholten and F. Iachello, Phys. Rev. Lett. 44 (1980) 1747.
- [62] A. Leviatan, Prog. Part. Nucl. Phys. 66 (2011) 66.
- [63] D.H. Feng, R. Gilmore and S.R. Deans, Phys. Rev. C 23 (1981) 1254.
- [64] D.D. Warner and R.F. Casten, Phys. Rev. C 28 (1983) 1798.
- [65] A. Leviatan, Phys. Rev. Lett. 77 (1996) 818.
- [66] A. Leviatan and I. Sinai, Phys. Rev. C 60 (1999) 061301(R).
- [67] R.L. Hatch and S. Levit, Phys. Rev. C 25 (1982) 614.
- [68] W. Zhang, C.C. Martens, D.H. Feng and J.M. Yuan, Phys. Rev. Lett. 61 (1988) 2167.
- [69] W.M. Zhang, D.H. Feng, J.M. Yuan and S.J. Wang, Phys. Rev. A 40 (1989) 438.
- [70] W.M. Zhang, D.H. Feng and J.M. Yuan, Phys. Rev. A 42 (1990) 7125.
- [71] V. P. Berezovoj, Yu. L. Bolotin and V. A. Cherkaskiy, Phys. Lett. A 323 (2004) 218.
- [72] P. Cejnar and P. Stránský, Phys. Rev. Lett. 93 (2004) 102502.
- [73] P. Stránský and P. Cejnar, Phys. Rev. C 74 (2006) 014306.
- [74] P. Stránský P. Hruška and P. Cejnar, Phys. Rev. E 79 (2009) 046202.



- [75] P. Stránský P. Hruška and P. Cejnar, Phys. Rev. E 79 (2009) 066201.
- [76] M. Hénon and C. Heiles, Astron. J. 69 (1964) 73.
- [77] P.W. Cleary, Phys. Rev. A 41 (1990) 2924.
- [78] P. Cejnar and P. Stránský, Phys. Rev. E 78 (2008) 031130.
- [79] A. Peres, Phys. Rev. Lett. 53 (1984) 1711.
- [80] M. Macek, J. Dobeš and P. Cejnar, Phys. Rev. C 80 (2009) 014319.
- [81] M. Macek, J. Dobeš and P. Cejnar, Phys. Rev. C 82 (2010) 014308.
- [82] A. Leviatan, Z. Phys. A 321 (1985) 467.
- [83] M. Macek, J. Dobeš, P. Stránský and P. Cejnar, Phys. Rev. Lett. 105 (2010) 072503.
- [84] I. C. Percival, J. Phys. B 6 (1973) L229.
- [85] N. Whelan, Y. Alhassid and A. Leviatan, Phys. Rev. Lett. 71 (1993) 2208.
- [86] A. Leviatan and N. D. Whelan, Phys. Rev. Lett. 77 (1996) 5202.
- [87] D. Bonatsos, E.A. McCutchan and R.F. Casten, Phys. Rev. Lett. 104 (2010) 022502.
- [88] P. Cejnar and J. Jolie, Phys. Lett. B 420 (1998) 241.
- [89] P. Cejnar and J. Jolie, Phys. Rev. E 58 (1998) 387.
- [90] D. Belitz, T.R. Kirkpatrick and T. Vojta, Rev. Mod. Phys. 77 (2005) 579.
- [91] L.A. Bunimovich, Chaos, 11 (2001) 802.
- [92] B. Dietz, T. Friedrich, M. Miski-Oglu, A. Richter and F. Schäfer, Phys. Rev. E 75 (2007) 035203(R).
- [93] G. Hose and H. S. Taylor, Phys. Rev. Lett. 51 (1983) 947.
- [94] L. E. Reichl and W. A. Lin, Foundations of Physics 17 (1987) 689.
- [95] D. A. Wisniacki, M. Saraceno, F.J. Arranz, R.M. Benito and F. Borondo, Phys. Rev. E 84 (2011) 026206.